A stochastic particle method for the investigation of turbulence/chemistry interactions in large-eddy simulations of turbulent reacting flows

A THESIS
SUBMITTED TO THE FACULTY OF THE GRADUATE SCHOOL
OF THE UNIVERSITY OF MINNESOTA
BY

Pietro Ferrero

IN PARTIAL FULFILLMENT OF THE REQUIREMENTS
FOR THE DEGREE OF
DOCTOR OF PHILOSOPHY

Graham V. Candler

December, 2013

Acknowledgements

Earning a doctoral degree in aerospace engineering at the University of Minnesota is one of the greatest accomplishments I have achieved so far in my life. It is undoubtedly a crucial step in the fulfillment of the dream of a little child that, when watching the lift off of the Space Shuttle for the first time in the early '90s, with weeping eyes immediately knew what he wanted to be.

What I didn't know back then is the huge number of extraordinary people that I would have met while chasing my dreams and how dramatically they would have changed my life for the better. The list is so long that a couple of pages cannot be exhaustive and I apologize with whom I might have omitted.

My warmest thanks go to my academic adviser, Prof. Graham Candler, for believing in my potentialities from the first minute and for giving the opportunity to join his outstanding research group without even having met me personally. In the five years we worked together I had the chance to appreciate his unmatched knowledge of fluid dynamics, his constant encouragements, his calmness in dealing with the issues invariantly arise in research as well as his kindness and positive attitude. I consider myself very privileged to have had Prof. Candler as my academic advisor.

I would like to thank Prof. Peyman Givi and Collin Otis from the University of Pittsburgh for the invaluable help I received from them during this work. Prof. Givi's research group is the pioneer in the use the filtered mass density function methodology and the innumerable discussions we had together helped me grasp and clarify most of the concepts pertaining this rather complex topic.

Similarly, I owe a lot to Prof. Paul Dimotakis of the California Institute of Technology, for helping me to understand the physics and the chemistry of turbulent reacting mixing layers.

I also want to thank all my colleagues in Prof. Candler's group for so many interesting discussions about fluid dynamics, science and much more. All of them had a very positive impact on my work both by directly helping me and by providing a cheerful and stimulating atmosphere in the office. I am especially grateful to Pramod Subbareddy, Ioannis Nompelis, Anand Kartha, Eric Stern, Joseph Brock, Paolo Valentini, Alan Schwing, Sriram Doraiswamy, Loretta Trevino, Aaron Neville, Vladymir Gizdak, Derek Dinzl, Ross Chaudhry, Erik Tylczak, Jason Bender, Sidharth G. S. and Heath Johnson.

Besides growing professionally as an engineer and a researcher, during my years in Minnesota I was very fortunate to meet some of the best and most loyal friends friends a person can ask for. I really want to thank Eyoab Zegeye, Kamran Turkoglu, Karen Rezikyan, Mostafa Toloui, Davide Giannuzzi, Raul Velasquez, Arda Özdemir, Senny Ghebrejohannes, Ilija Bojovic, Federico "the boss" Galli, Daniel Rave, Deepak Adhikari, Annalisa Franco, Kyung-Hoon Shin and all the FC Voyageurs soccer team for sharing so many good times together and for being like brothers to me.

Equally important have been my "old" friends on the other side of the ocean which, through their warmth, always made me feel as I never left home. These include Alberto Ribotta, Alessio Ribotta, Andrea Ferrero, Manlio Matsumura, Luca Sigot, Damiano Borgogno, Federico Mario Mighetto, Nicola Di Nardo, Luca "slopewalker" Bertini, Pep Morral, Roberto Gervasio, Tommaso Banone, Carlotta Barile, Marco Angeletti and Pasquale Mastromauro.

Lastly, but not for importance, I would have never have reached this goal if it were not for my mother, Chiara Ribotta, and my father, Dario Ferrero. During my years in graduate school, not only they gave me unconditional love, support and encouragement but they shared with me my joys and my sorrows, my successes and my defeats, as if they were theirs. There are simply no words for me to express how much I owe them.

Abstract

The main objective of this work is to investigate the effects of the coupling between the turbulent fluctuations and the highly non-linear chemical source terms in the context of large-eddy simulations of turbulent reacting flows. To this aim we implement the filtered mass density function (FMDF) methodology on an existing finite volume (FV) fluid dynamics solver. The FMDF provides additional statistical sub-grid scale (SGS) information about the thermochemical state of the flow - species mass fractions and enthalpy - which would not be available otherwise. The core of the methodology involves solving a transport equation for the FMDF by means of a stochastic, grid-free, Lagrangian particle procedure. Any moments of the distribution can be obtained by taking ensemble averages of the particles. The main advantage of this strategy is that the chemical source terms appear in closed form so that the effects of turbulent fluctuations on these terms are already accounted for and do not need to be modeled.

We first validate and demonstrate the consistency of our implementation by comparing the results of the hybrid FV/FMDF procedure against model-free LES for temporally developing, non-reacting mixing layers. Consistency requires that, for non-reacting cases, the two solvers should yield identical solutions. We investigate the sensitivity of the FMDF solution on the most relevant numerical parameters, such as the number of particles per cell and the size of the ensemble domain. Next, we apply the FMDF modeling strategy to the simulation of chemically reacting, two- and three-dimensional temporally developing mixing layers and compare the results against both DNS and model-free LES. We clearly show that, when the turbulence/chemistry interaction is accounted for with the FMDF methodology, the results are in much better agreement to the DNS data. Finally, we perform two- and three-dimensional simulations of high Reynolds number, spatially developing, chemically reacting mixing layers, with the intent of reproducing a set of experimental results obtained at the California Institute of Technology. The mean temperature rise calculated by the hybrid FV/FMDF solver, which is associated with the amount of product formed, lies very close to the experimental profile. Conversely, when the effects of turbulence/chemistry coupling are ignored, the simulations clearly over predict the amount of product that is formed.

Contents

List of Tables

List of Figures

Chapter 1

Introduction

Turbulent reacting flows play a predominant role in transportation, in many industrial processes and, in a sense, in our society as a whole. There are two main reasons for why this is true. First, as of now - and for the foreseeable future - the world's increasing energy demands can only be satisfied by the combustion of hydrocarbon fuels. Second, essentially all reacting flows in industrial applications are turbulent. The increasing and ever fluctuating price of fuel as well as the concern over the environmental impact of the combustion's products has recently led a large research effort to improve the efficiency of the combustion process. It is reasonable to assume that any improvements in this area will most likely have its origins in a better understanding of the underlying physics of the problem.

There are essentially two complimentary lines of research that are pursued in order to tackle the difficulties of turbulent reacting flows: experimental measurements and computational simulations. In this work we pursue the latter direction. Computational simulations are very attractive because they are usually cheaper and faster to set up and run than an experimental apparatus and because their predictive capabilities are extensively used in the design cycle of combusting devices. On the other hand, as recently reviewed by Pope (2012), turbulent reacting flows present many serious challenges to the current simulation models. These include the large number of chemical species that are usually involved in the combustion processes, the wide range of length and time scales that characterizes high-Reynolds number flows, the coupling between reaction and molecular diffusion, and the presence of non-linear chemical kinetics together with

large turbulent fluctuations.

There are currently three major approaches, with very different computational costs, that are used in computational fluid dynamics of turbulent flows: Reynolds-averaged Navier-Stokes simulation (RANS), large-eddy simulation (LES) and direct numerical simulation (DNS). In the RANS approach only the time averaged form of the Navier-Stokes equations are explicitly solved, while all the fluctuating terms due to turbulence are modeled. RANS simulations are able to provide a solution in a "reasonable" time even for very large and complex domains and, together with the fact that they can simulate flows with any Reynolds number, they represent the state of the art in many industrial applications. The biggest limitation of RANS is that, even for non reacting flows, there are not universal models for the fluctuating terms and those available need to be constantly adjusted to fit experimental data.

On the other side of the spectrum lie direct numerical simulations, in which all the fluid and chemical scales are explicitly computed and no modeling is required. Although DNS is a very useful tool for turbulence research and for the validations of closure models, its use is limited to low-Reynolds number flows, mainly because of its very high computational cost. Furthermore, it has been appreciated by many authors (see Echekki and Mastorakos (2011), Chen et al. (2009) and Choi and Moin (2012)) that even using the most optimistic models for the growth of computational power, performing a DNS of a practical combustion device will be unfeasible for many decades to come.

The third simulation strategy, large-eddy simulation, lies somewhere in between the former two methodologies. The main idea behind LES is to resolve all the large turbulent energy containing scales and to model only the dissipative ones. This is achieved by passing the transport variables through a spatial filter and only solve for the so-called filtered part. Because of this procedure the effects of fluctuations at small (or unresolved) scales has to be modeled. These fluctuations, which are usually called sub-grid scale (SGS) terms, are smaller, more universal and much less problem-dependent than those that have to be modeled in RANS. Although much more expensive, it is widely recognized (see for example Pope (2000)) that LES can achieve far superior accuracies than RANS.

We must note that these simulation strategies are common to any turbulent flows, wether they are chemically reacting or inert. In the case of reacting flows, however, there

are additional complications that arise in the modeling of the unclosed terms in RANS and LES. One of the most important, as reviewed by Pope (2012), is the combined effect of the large turbulent fluctuations and the non-linear chemical source terms, which prevents the use of simple models based on expansion about mean properties. This is unlike the effects of turbulence on the momentum equations, where the resulting Reynolds stress tensor can be adequately be modeled using, for example, a gradient-diffusion approximation. Because of these intrinsic difficulties, turbulence/chemistry interactions are sometimes ignored although some authors, such as Colucci et al. (1998), Jaberi et al. (1999), Pope (2000) and the results of this work clearly show that neglecting these effects can lead to large errors.

One possible solution - which is the one we adopted - consists to model the turbulence/chemistry interactions using some description of the statistical distribution of the fluid composition, usually through the joint probability density function (PDF) of the species mass fractions and enthalpy. There are two different categories of methodologies that are used to obtain the PDF. One approach is to use the assumed PDF methods, in which the shape of the distribution function is assumed a priori and is determined by a small set of parameters such as the mean and the variance. The flamelet-like class of models, which assume a very strong coupling between reactions and molecular diffusion and also imply that the species mass fractions are confined to a very-low-dimensional manifold in the species space, belong to the assumed PDF category (Pope (2012)). Alternatively, a second approach is to use transported PDF methods, in which the joint PDF is directly computed by solving a modeled transport equation that describes its evolution. This class of methods, although more computationally expensive, do not make any assumptions on the shape of the PDF and are consequently more general. Because of these desirable features, this is the methodology that we implemented and used extensively in this work to investigate turbulent combustion.

Transported PDF methods (hereafter only called PDF methods) were originally developed by Pope (1981) and Pope (1985) as a model for RANS. Pope (1991) formulated the concept of the Filtered Density Function (FDF), which is the extension of PDF methods to LES. Colucci et al. (1998) were the first to show the improved accuracy of the FDF over model-free LES for incompressible, constant density reactive flows. Jaberi et al. (1999) further extended the FDF by formulating the filtered mass density function

(FMDF), which can be used to simulate low-Mach number flows with variable density. Since these early results the FDF/FMDF methodology has become very popular in the field of combustion research as reviewed by Givi (2006) and Pope (2000).

Based on these considerations, the two main objectives of this work are, first, to implement the FMDF methodology on a high-order, unstructured compressible finite volume (FV) solver and, second, to use this tool to investigate the effects of turbulence/chemistry interaction on large-eddy simulations of turbulent reacting flows.

As already noted, PDF methods rely on the solution of a transport equation for the distribution function of the concentrations and the enthalpy. This is a very highly-dimensional equation which would be impractical to solve with a conventional finite difference or finite volume technique. Instead, we implement a Monte Carlo solution method, which uses "stochastic" particles to approximate the distribution functions. These particles are advected through space in a Lagrangian manner and are used to calculate any finite moments of the distribution function by taking appropriate ensemble averages.

Despite its many successes for low-Mach number reacting flow simulations, very little work has been done to extend the FMDF formulation to compressible, high-Mach flows. The only published work we are aware of is Banaeizadeh et al. (2011). Because in this thesis we are concerned with both incompressible and compressible applications, we follow their approach to derive and test a compressible formulation of the FMDF methodology.

Moreover, with the exceptions of Ansari et al. (2011), Subramaniam and Haworth (2000) and few other works, most of the research using PDF/FMDF methods has been carried out on structured Cartesian grids, usually with equally spaced elements. Although this approach greatly simplifies the particle tracking in the domain, it also limits the geometrical complexity of the problems that can be simulated. In this work we develop and implement a FMDF/Monte Carlo procedure that does not assume any particular grid topology and works on unstructured grids composed of any type of polyhedrons.

In addition, we developed the FMDF solver to work on the same parallel infrastructure that is used for the finite volume solver. This feature enables us to use high-performance computing facilities to perform simulations of considerable size as we show

in the results section.

We accomplish the second objective - studying the effects on turbulence on the chemistry source terms - by performing several large-eddy simulations on temporally developing and spatially developing mixing layers. A mixing layer is formed by two near-parallel flows with different velocities. Small disturbances initiate instabilities that grow, and eventually result in the break up and formation of a turbulent mixing layer. In these flows, turbulence causes spatial dispersion and redistribution of fluids at different scales that enhances mixing and the homogenization of the flowfield (Bonanos et al. (2009)). Mixing layers are good candidates to perform fundamental studies on turbulent combustion because, as Dimotakis (1991) points out, they contain all the physics of the problem without the additional complexities of real combustors. We use temporally developing mixing layers, which are computationally cheap to run, first to validate the implementation of the FMDF methodology and to demonstrate that its results are consistent with the finite volume method for non-reacting cases. We also show the increased accuracy of the FMDF methodology in predicting the product formation in reacting cases by comparing its predictions with the results of a DNS for the same flow. We then use the FMDF methodology to numerically reproduce the experimental results obtained by Slessor et al. (1998) involving high-Reynolds, chemically reacting mixing layers at Supersonic Shear Layer Facility (S^3L) at the California Institute of Technology. The chemical reaction mechanism is the combustion of hydrogen and fluorine, which is characterized by very fast kinetics and is composed of several basic reactions. These flows are much more complicated and expensive to simulate as compared to the temporally developing mixing layers we use for validation. Nevertheless, also for these more realistic configurations, FMDF shows superior accuracy over the model-free LES and its predictions are in closer agreement with the experimental data.

This thesis is organized as follows. In chapter 2 we present both the unfiltered and the LES governing equations for multi-species, chemically reacting gases and we briefly discuss the modeling strategies for the unclosed terms. We then describe the FMDF transport equation and outline the Monte Carlo procedure we used to solve it. In the last part we also provide a possible extension of the FMDF formulation to compressible flows. In chapter 3 we describe in detail the numerical methods that we use to solve the hybrid FMDF/FV system, with particular emphasis on the features of the Monte Carlo solver

that we developed for this work. Next, we validate and demonstrate the consistency of the FMDF methodology by running some non-reacting cases in chapter 4. In chapter 5 we show that FMDF/FV procedure yields more accurate results for chemically reacting flows as compared to LES without turbulence/chemistry modeling. These findings are further expanded in chapter 6, where we present the results of our two- and three-dimensional simulations of spatially developing, chemically reacting mixing layers and compare the predictions of the FMDF/FV solver against experimental results. Finally, in chapter 7, we summarize the achievements and the findings of the present work and provide some advice for future research on the topic.

Chapter 2

Mathematical formulation

In this chapter we present the system of coupled differential equations that govern the fluid motion and we lay down the mathematical formulation of the filtered mass density function (FMDF) methodology. The types of flows that have been studied in this thesis can adequately be described by the Navier-Stokes equations for a thermally perfect, chemically reacting gas mixture, coupled with an equation of state. The only two assumptions implicit in this formulation are that the flow always lies in the continuum regime and that high-enthalpy, "real gas" relaxation processes can be neglected. The high-Reynolds number and relatively low temperatures achieved by the flowfields that we simulated guarantee that these assumptions are never violated. This set of equations can be directly solved as is whenever all spatial and temporal scales can be explicitly resolved, as in the case of direct numerical simulations (DNS). For high Reynolds number flows, due to computational limitations, this is usually impossible and only the motion of the larger scales are actually resolved, while the effects of the smaller scales are modeled. This procedure is mathematically equivalent to applying a spatial filter to the Navier-Stokes equations and the resulting set of equations is called the large-eddy simulation (LES) equations. We present these equations in a subsequent section of the chapter together with a discussion of all the terms that require modeling. Particular emphasis is placed on the chemical source term, as this is the objective of the FMDF formulation. In the last part of the chapter, we introduce the mathematical definition of the filtered mass density function together with the transport equation that describes its evolution. The exact FMDF transport equation still contains unclosed terms and

is characterized by a high dimensionality which makes it impractical to solve it with traditional numerical schemes. We therefore discuss the models and assumptions that we use to simplify the unclosed terms and we introduce the principle of equivalent systems, which justifies the use of stochastic Monte Carlo methods for the solution of the FMDF transport equation.

2.1 Unfiltered (DNS) equations

The governing equations for a gas mixture composed of N_s chemical species are:

$$\frac{\partial \rho_s}{\partial t} + \frac{\partial}{\partial x_j}\left(\rho_s u_j\right) + \frac{\partial J_j^s}{\partial x_j} = \rho\omega_s, \qquad s = 1, 2, ..., N_s \tag{2.1a}$$

$$\frac{\partial}{\partial t}\left(\rho u_i\right) + \frac{\partial}{\partial x_j}\left(\rho u_i u_j + p\delta_{ij} - \sigma_{ij}\right) = 0, \tag{2.1b}$$

$$\frac{\partial}{\partial t}\left(\rho E\right) + \frac{\partial}{\partial x_j}\left[\left(\rho E + p\right) u_j - \tau_{ij} u_i + q_j + \rho v_{j,s} h_s\right] = 0, \tag{2.1c}$$

where u_i is the velocity vector, ρ_s the mass density of species s, p the pressure, ρ is the mass density of the mixture ($\rho = \sum_{s=1}^{N_s} \rho_s$), $v_{j,s}$ is the diffusion velocity of species s, while ω_s is the chemical source term. Note that we solve separate equations for each of the species densities. Furthermore, by summing eqs. (2.1a) over all species, the diffusive and chemical source terms sum to zero and we recover the traditional continuity equation,

$$\frac{\partial \rho}{\partial t} + \frac{\partial \rho u_j}{\partial x_j} = 0. \tag{2.2}$$

The diffusive fluxes are the mass diffusion, J_j^s, the heat flux vector, q_j and the stress tensor σ_{ij}. The last term on the total energy equation is due to the diffusion of species with different enthalpies, where $v_{j,s}$ is the diffusion velocity of species s. If we neglect the effects of vibrational non-equilibrium, the total energy per unit volume, E, is defined as

$$E = \sum_{s=1}^{N_s} \rho_s C_{V\,s} T + \frac{1}{2} u_i u_i + \sum_{s=1}^{N_s} \rho_s h_s^o, \tag{2.3}$$

where T is the static temperature, while $C_{V\,s}$ and h_s^o are the specific heat at constant volume and the enthalpy of formation for species s, respectively. In order to close the system, an equation of state must be prescribed. We use the perfect gas law, which is generalized to multi-species mixtures using Dalton's law,

$$p = \sum_{s=1}^{N_s} p_s = \sum_{s=1}^{N_s} \rho_s \frac{R}{\mathcal{M}_s} T = \rho \overline{R} T, \qquad \text{with} \quad \overline{R} = \sum_{s=1}^{N_s} c_s \frac{R}{\mathcal{M}_s}, \tag{2.4}$$

where R is the universal gas constant and $\mathcal{M}_s$ and p_s are the species molecular mass and partial pressure, respectively. The species mass fractions, c_s, are defined as

$$c_s \equiv \frac{\rho_s}{\rho}, \tag{2.5}$$

and, by definition, $\sum_{s=1}^{N_s} c_s = 1$. In the total energy equation it also appears the static enthalpy per unit mass of species s, which is defined as

$$h_s = C_{V\,s} T + \frac{p_s}{\rho_s} + h_s^o. \tag{2.6}$$

In lieu of the total energy equation, eq. (2.1c), a static enthalpy equation can be also be used,

$$\frac{\partial}{\partial t}(\rho h) + \frac{\partial}{\partial x_j}(\rho h u_j) = -\frac{\partial q_j}{\partial x_j} + \sigma_{ij}\frac{\partial u_i}{\partial x_j} + \frac{Dp}{Dt} - \frac{\partial}{\partial x_j}\left(\rho v_{j,s} h_s\right), \tag{2.7}$$

where the enthalpy of the mixture is defined as,

$$h = \sum_{s=1}^{N_s} h_s c_s, \tag{2.8}$$

where h_s is given by eq. (2.6).

2.1.1 Diffusive fluxes

In this section we present the closures we adopted for the diffusive fluxes. The stress tensor and heat flux vector are assumed to obey Newton's and Fourier's law, respectively,

$$\sigma_{ij} = \mu\left(\frac{\partial u_i}{\partial x_j} + \frac{\partial u_j}{\partial x_i} - \frac{2}{3}\frac{\partial u_k}{\partial x_k}\sigma_{ij}\right), \qquad q_j = \kappa\frac{\partial T}{\partial x_j}, \tag{2.9}$$

where μ is the kinematic viscosity, κ is the thermal conductivity and the Stokes hypothesis has been used. The mass diffusion flux for the species s depends on the diffusion velocity $v_{j,s}$,

$$J_j^s = \rho_s v_{s,j}. \tag{2.10}$$

The diffusion velocities are in general a function of the gradients of concentrations, temperature and pressure. In this work we assume that the temperature and pressure effects are negligible and model $v_{j,s}$ only through gradients of concentration (Fick's law):

$$\rho_s v_{s,j} = -\rho \mathcal{D}_s \frac{\partial c_s}{\partial x_j}, \tag{2.11}$$

where $\mathcal{D}_s$ are the species diffusion coefficients. An important assumption that is made is to neglect multi-component diffusion and replace the $\mathcal{D}_s$ with a single binary diffusion coefficient $\mathcal{D}$. The latter is derived by assuming a constant Lewis number,

$$\mathrm{Le} = \frac{\mathrm{Sc}}{\mathrm{Pr}} = \mathcal{D}\frac{\rho \mathrm{C_p}}{\kappa}, \tag{2.12}$$

where C_P is the specific heat at constant pressure of the mixture and Sc and Pr are the Schmidt and Prandtl numbers,

$$\mathrm{Sc} = \frac{\mu}{\mathcal{D}}, \qquad \mathrm{Pr} = \frac{\kappa}{\mu \mathrm{C_p}}. \tag{2.13}$$

The kinematic viscosity coefficient is either constant or calculated using Blottner curve fits (Nompelis (2004)). The thermal conductivity coefficient is derived from μ by prescribing a constant Prandtl number.

2.1.2 The chemical source terms

In this section we give a detailed description of the chemical source terms that appear in the species mass conservation equations, eqs. (2.1a), and which are the main focus of this work. Following the description given in Poinsot and Veynante (2005), a generic chemical system of N_s species reacting with M reactions can be written as,

$$\sum_{s=1}^{N_s} \nu'_{s,j} \mathcal{A}_s \rightleftharpoons \sum_{s=1}^{N_s} \nu''_{s,j} \mathcal{A}_s, \qquad \text{for} \quad j = 1, ..., M \tag{2.14}$$

where $\mathcal{A}_s$ is the chemical symbol for species s, while $\nu'_{s,j}$ and $\nu''_{s,j}$ are the molar stoichiometric coefficients for species s in reaction M. Mass conservation requires that

$$\sum_{s=1}^{N_s} \left(\nu'_{s,j} - \nu''_{s,j}\right) \mathcal{A}_s = 0, \qquad \text{for} \quad j = 1, ..., M. \tag{2.15}$$

The chemical source term for species s is the sum of the reaction rates $\omega_{s,j}$ of all M reactions,

$$\omega_s = \sum_{j=1}^{M} \omega_{s,j}. \tag{2.16}$$

It is convenient to define a new variable, $\mathcal{Q}_j$, called the rate of progress for the jth reaction,

$$\mathcal{Q}_j \equiv \frac{\omega_{s,j}}{\mathcal{M}_s(\nu'_{s,j} - \nu''_{s,j})}, \tag{2.17}$$

so that

$$\omega_s = \mathcal{M}_s \sum_{j=1}^{M} (\nu'_{s,j} - \nu''_{s,j}) \mathcal{Q}_j. \tag{2.18}$$

By summing all the reaction rates ω_s and using eq. (2.15) we obtain,

$$\sum_{s=1}^{N_s} \omega_s = \sum_{s=1}^{N_s} \left(\mathcal{M}_s \sum_{j=1}^{M} (\nu'_{s,j} - \nu''_{s,j}) \mathcal{Q}_j \right) = 0, \tag{2.19}$$

which justifies eq. (2.2) and is again a consequence of mass conservation.

The rate of progress for reaction j is a function of the molar concentrations $[X_s] = \rho_s / \mathcal{M}_s$,

$$\mathcal{Q}_j = k_{f_j} \prod_{s=1}^{N_s} [X_s]^{\nu'_{s,j}} - k_{b_j} \prod_{s=1}^{N_s} [X_s]^{\nu''_{s,j}}, \tag{2.20}$$

where k_{f_j} and k_{b_j} are the forward and backward reaction rates, respectively. The former are modeled using the empirical Arrehenius law,

$$k_{f_j} = C_{f_j} T^{\eta_j} \exp\left(\frac{-E_a}{RT}\right), \tag{2.21}$$

where the pre-exponential factor, C_{f_j}, the temperature exponent, η_j and the activation energy E_a are empirical coefficients that must be provided for each of the M reactions.

The backward reactions rates, k_{f_j}, are obtained from the forward reactions rates through

$$k_{bj}(T) = \frac{k_{f_j}}{k_{eq_j}}, \tag{2.22}$$

where the equilibrium rate constants $k_{bj}(T)$ are assumed to be only functions of temperature and are calculated from a theoretical curve fit of the form

$$k_{eq_j} = \frac{a_1}{Z} + a_2 \log Z + a_3 Z + a_4 Z^2 + a_5 Z^3, \tag{2.23}$$

where $Z = 10,000/T$ and the constants that appear in eq. (2.23) are taken from curve fits.

2.1.3 Low Mach number approximation

In the case of variable-density, low Mach number flows the static enthalpy equation, eq. (2.7), reduces to

$$\frac{\partial}{\partial t}(\rho h) + \frac{\partial}{\partial x_j}(\rho h u_j) = -\frac{\partial q_j}{\partial x_j} - \frac{\partial}{\partial x_j}(\rho v_{j,s} h_s), \tag{2.24}$$

because the total derivative of the pressure and the viscous dissipation become negligible (Poinsot and Veynante (2005)). If the flow is characterized by a unity Lewis number (Le = 1) and we neglect the diffusion of species with different enthalpies, then eq. (2.7) has the same form as the species mass fraction equations, eqs. (2.1a), and they can be lumped together as

$$\frac{\partial \rho \phi_\alpha}{\partial t} + \frac{\partial \rho u_j \phi_\alpha}{\partial x_j} = -\frac{\partial J_j^\alpha}{\partial x_j} + \rho S_\alpha, \qquad \alpha = 1, 2, ..., N_s + 1. \tag{2.25}$$

The scalar vector $\phi_\alpha = (c_1, c_2, ..., c_{N_s}, h)^T \equiv \Phi$, of length N_s+1, contains the mass fraction of the N_s species plus the specific enthalpy h. The source terms are

$$S_\alpha = \begin{cases} \dot{\omega}_\alpha & \text{for } \alpha = 1, ..., N_s \\ 0 & \text{for } \alpha = N_s + 1 \end{cases} \tag{2.26}$$

Using the previous assumptions the diffusive terms are also grouped together as

$$J_j{}^{\alpha} = -\rho\Gamma\frac{\partial\phi_\alpha}{\partial x_j}, \quad \alpha = 1, ..., N_s + 1. \tag{2.27}$$

where Γ represents the mass and thermal diffusivities, which are the same for $\mathrm{Le} = 1$.

2.2 LES equations

The LES equations are obtained by applying a spatial filter $G(\mathbf{x}, \mathbf{x}'; \Delta)$ to the Navier-Stokes equations, eqs. (2.1). Each variable f is thus divided into a resolved part, denoted by an overbar, and a sub-grid scale (SGS) part, which is denoted by a prime:

$$f(\mathbf{x}) = \overline{f}(\mathbf{x}) + f'(\mathbf{x}). \tag{2.28}$$

The filtered part is formally defined as

$$\overline{f}(\mathbf{x}) = \int_{\mathcal{D}} f(\mathbf{x}')G(\mathbf{x}, \mathbf{x}'; \Delta)d\mathbf{x}', \tag{2.29}$$

where Δ is the filter width and $\mathcal{D}$ is the computational domain. The spatial filter, G, can assume different forms and it will influence the resolved field, as reviewed by Pope (2000). In this work we use a simple box function, where the filter width, Δ, is some function of the local cell dimensions. The filtering is thus directly applied by the grid and we do not attempt any type of explicit filtering. For compressible flows it is convenient to use Favre-averaging to eliminate the additional SGS terms that appear in the mass fraction equation,

$$\widetilde{f} = \frac{\overline{\rho f}}{\overline{\rho}}, \tag{2.30}$$

so that the total density equation,

$$\frac{\partial\overline{\rho}}{\partial t} + \frac{\partial\overline{\rho}\widetilde{u}_j}{\partial x_j} = 0. \tag{2.31}$$

has the same mathematical form as the unfiltered one, eq. (2.2).
The filtered form of the Navier-Stokes equations are

$$\frac{\partial \bar{\rho}_s}{\partial t} + \frac{\partial \bar{\rho}_s \widetilde{u}_j}{\partial x_j} = -\frac{\partial \bar{\rho}_s \widetilde{v}_{s,j}}{\partial x_j} - \frac{\partial \mathcal{V}_{s,j}}{\partial x_j} + \bar{\omega}_s, \tag{2.32a}$$

$$\frac{\partial \bar{\rho} \widetilde{u}_i}{\partial t} + \frac{\partial \bar{\rho} \widetilde{u}_i \widetilde{u}_j}{\partial x_j} = -\frac{\partial \bar{p}}{\partial x_i} + \frac{\partial \bar{\sigma}_{ij}}{\partial x_j} - \frac{\partial \tau_{ij}}{\partial x_j}, \tag{2.32b}$$

$$\begin{aligned} \frac{\partial \bar{E}}{\partial t} + \frac{\partial}{\partial x_j}\left[(\bar{E}+\bar{p})\tilde{u}_j + \widetilde{q}_j - \bar{\sigma}_{ij}\tilde{u}_i + \sum_s \bar{\rho}_s \tilde{h}_s \tilde{v}_{s,j}\right] = \\ -\frac{\partial}{\partial x_j}\left(q_{T,j} + \mathcal{J}_j - \mathcal{D}_j + \sum_s h_s^0 \mathcal{V}_{s,j}\right), \end{aligned} \tag{2.32c}$$

where the diffusive terms are given by

$$\widetilde{\sigma_{ij}} = \widetilde{\mu}\left(\frac{\partial \widetilde{u}_i}{\partial x_j} + \frac{\partial \widetilde{u}_j}{\partial x_i} - \frac{2}{3}\frac{\partial \widetilde{u_k}}{\partial x_k}\widetilde{\sigma_{ij}}\right), \qquad \widetilde{q}_j = \widetilde{\kappa}\frac{\partial \widetilde{T}}{\partial x_j}, \qquad \bar{\rho}_s \widetilde{v}_{s,j} = -\bar{\rho}\widetilde{\mathcal{D}}\frac{\partial \widetilde{c}_s}{\partial x_j}, \tag{2.33}$$

which implies that SGS fluctuations of the diffusion terms have been neglected. Previous work by Vreman et al. (1995) in subsonic mixing layers found that these non-linearities are indeed small. The filtered equation for the static enthalpy, eq. (2.7), is

$$\frac{\partial}{\partial t}\left(\overline{\rho}\widetilde{h}\right) + \frac{\partial}{\partial x_j}\left(\overline{\rho}\widetilde{h}\widetilde{u_j}\right) = -\frac{\partial \widetilde{q_j}}{\partial x_j} + \tilde{\sigma}_{ij}\frac{\partial \widetilde{u_i}}{\partial x_j} + \frac{D\overline{p}}{Dt} - \frac{\partial}{\partial x_j}\left(\overline{\rho}\tilde{v}_{j,s}\tilde{h}_s\right) - C_V\frac{\partial q_{T,j}}{\partial x_j} - \Pi_{dil} + \epsilon_v, \tag{2.34}$$

The sub-grid scale (SGS) terms that arise from the filtering operation are the SGS stress tensor, τ_{ij}, the turbulent mass flux, $\mathcal{V}_{s,j}$, the turbulent heat flux, q_{Tj}, the turbulent diffusion $\mathcal{J}_j$, the SGS viscous diffusion D_j, the SGS pressure-dilatation Π_{dil}, and the

SGS viscous dissipation ϵ_v. These unclosed terms are formally defined as,

$$\tau_{ij} = \overline{\rho}(\widetilde{u_i u_j} - \widetilde{u}_i \widetilde{u}_j) \tag{2.35a}$$

$$\mathcal{V}_{s,j} = \overline{\rho}(\widetilde{c_s u_j} - \widetilde{c}_s \widetilde{u}_j) \tag{2.35b}$$

$$q_{T,j} = \overline{\rho}(\widetilde{u_j T} - \widetilde{u}_j \widetilde{T}) \tag{2.35c}$$

$$\mathcal{J}_j = \overline{\rho}(\widetilde{u_j u_k u_k} - \widetilde{u}_j \widetilde{u_k u_k}) \tag{2.35d}$$

$$\mathcal{D}_j = \overline{\sigma_{ij} u_i} - \widetilde{\sigma}_{ij} \widetilde{u}_i \tag{2.35e}$$

$$\Pi_{dil} = \overline{p S_{kk}} - \overline{p} \widetilde{S}_{kk} \tag{2.35f}$$

$$\epsilon_v = \overline{\sigma_{ji} S_{ij}} - \widetilde{\sigma}_{ji} \widetilde{S}_{ij}. \tag{2.35g}$$

As we described in sec. 2.1.2, the source term $\omega_s = \omega_s(c_s, T)$ is a complex nonlinear function of the species concentrations and the temperature. Neglecting the effects of SGS turbulent fluctuations on the chemical source term is equivalent to make the assumption that

$$\widetilde{\omega_s(c_s, T)} \approx \omega_s(\tilde{c}_s, \tilde{T}), \tag{2.36}$$

which is mathematically incorrect because the filtering operation does not commute for non-linear functions. As reviewed by Pope (2012), it is well known that turbulence/chemistry interactions can play a significant role in LES of chemically reacting flows and that neglecting them can to lead to an overprediction of mixing and, consequently, of product formation. An improved treatment of the chemical source term, which avoids the drastic assumption implied by eq. (2.36), is the main objective of the FMDF formulation which will be discussed in sec. 2.3.

2.2.1 Model of the SGS quantities

The SGS terms that are highlighted in eqs. (2.35) and (2.36) cannot be derived from first principles and need to be modeled. For the SGS stress tensor, eq. (2.35a), we use the Boussinesq eddy viscosity assumption,

$$\tau_{ij} = -2\mu_{\mathrm{T}} \left(\tilde{S}_{ij} - \frac{1}{3} \tilde{S}_{kk} \delta_{ij} \right), \tag{2.37}$$

where $\tilde{S}_{ij}$ is the resolved rate of strain tensor and μ_{T} is the eddy viscosity coefficient. The idea behind eddy viscosity models is to try to reproduce the exchange of energy between the resolved and the unresolved scales by mimicking the drain of energy that characterizes the turbulent cascade. The SGS mass and heat transfer fluxes are also treated using a gradient diffusion hypothesis (Pope (2000)),

$$\mathcal{V}_{s,j} = -\frac{\mu_{\mathrm{T}}}{\mathrm{Sc}_{\mathrm{T}}}\frac{\partial \tilde{c}_s}{\partial x_j}, \quad q_{T,j} = -\frac{\mu_{\mathrm{T}}}{\mathrm{Pr}_{\mathrm{T}}}\frac{\partial \tilde{T}}{\partial x_j}, \tag{2.38}$$

where the turbulent Schmidt (Sc_{T}) and Prandtl (Pr_{T}) numbers are constants of the model. No attempt is done to evaluate them dynamically, although Martin et al. (2000) showed that certain dynamic models have better performance then the static ones in a priori simulations of isentropic turbulence decay. The calculation of the eddy viscosity is a central problem in LES and over the years many different models have been proposed, some of which are reviewed by Pope (2000). In this thesis we use the Modified Kinetic Energy Model (MKEV) and the one-equation turbulence model developed by Spalart and Allmaras (1992). The former is a modified, compressible version of the one proposed by Bardina et al. (1983), in which the eddy viscosity is determined based on the subgrid kinetic energy

$$\nu_{\mathrm{T}} = C_k \Delta \sqrt{\left| \widetilde{\widetilde{u_i^* u_i^*}} - \widetilde{\widetilde{u_i^*}}\,\widetilde{\widetilde{u_i^*}} \right|}, \tag{2.39}$$

where $u_i^* = u_i - \mathcal{U}_i$ and $\mathcal{U}_i$ is a reference velocity which is imposed to guarantee the Galilean invariance of the model. The double tilde denotes the filter at the secondary level which has a characteristic width larger than that of the grid level filter Δ.

The second turbulence model we employed is the compressible version of the Spalart-Allmaras model (SA) as described in Catris and Aupoix (2000). Although originally developed in the context of Raynolds-Averaged Navier Stokes (RANS) simulations, the SA model has been more recently expanded by Spalart et al. (1997) to work in detached-eddy simulation (DES) mode. The compressible SA is a one equation model that determines the eddy viscosity by solving a semi-empirical transport equation for ν_T,

$$\frac{D\rho\tilde{\nu}}{Dt} = c_{b1}\rho\tilde{S}\tilde{\nu} + \frac{1}{\sigma}\left[\nabla\cdot(\mu\nabla\tilde{\nu}) + \sqrt{\rho}\tilde{\nu}\nabla(\sqrt{\rho}\tilde{\nu}) + c_{b2}(\nabla\sqrt{\rho}\tilde{\nu})^2\right] - c_{w1}f_w\rho\left(\frac{\tilde{\nu}}{d_w}\right)^2, \tag{2.40}$$

where the working variable $\tilde{\nu}$ is related to the eddy viscosity through

$$\nu_T = \tilde{\nu} f_{v1}, \tag{2.41}$$

where

$$f_{v1} = \frac{\chi^3}{\chi^3 + c_{v1}^3} \qquad \text{and} \qquad \chi = \frac{\tilde{\nu}}{\nu}. \tag{2.42}$$

The working variable $\tilde{\nu}$ has been introduced in the original formulation to ensure proper behavior of the eddy viscosity close to the walls. The first term on the right-hand side of eq. (2.40) is the production term and it contains the variable $\tilde{S}$, defined as

$$\tilde{S} = S + \frac{\tilde{\nu}}{\kappa^2 d_w^2} \qquad \text{and} \qquad f_{v2} = 1 - \frac{\chi}{1 + \chi_{v1}}, \tag{2.43}$$

where S is the vorticity magnitude, κ the von Karman constant and d_w is the distance from the wall. The last term on the right-hand side is the destruction term, which contains the function f_w,

$$f_w = g \left(\frac{1 + c_{w3}^6}{g^6 + c_{w3}^6} \right)^{1/6}, \tag{2.44}$$

with

$$g = r + c_{w2}(r^6 - r) \qquad \text{and} \qquad r = 1 - \frac{\tilde{\nu}}{\tilde{S} \kappa^2 d_w^2}. \tag{2.45}$$

In this work we only simulate free flows which are not wall-bounded. For this reason we disable the wall functions by enforcing

$$f_{v1} = 1 \qquad \text{and} \qquad f_{v2} = 0, \tag{2.46}$$

and by setting f_w to its asymptotic value of $f_w^* = 0.424$. Furthermore, the wall distance d_w is replaced with the largest cell dimension, Δ, so that the model always works in LES mode.

The SGS turbulent diffusion is modeled following Knight et al. (1998),

$$S_j = \widetilde{u}_k \tau_{jk}, \tag{2.47}$$

where τ_{jk} is modeled SGS stress tensor given by eq. (2.37).

No attempt is made to model the SGS viscous diffusion (D_j), as no models are currently available in the literature and because its relative importance compared to the other SGS terms in the total energy equation is negligible (Martin et al. (2000)). Similarly, both the SGS pressure-dilatation Π_{dil} and the SGS viscous dissipation ϵ_v have been neglected. These two last terms are negligible in low Mach number flows.

2.2.2 Low Mach number approximation for LES equations

Similarly to the DNS equations presented in sec. (2.1.3), whenever $M \ll 1$, the filtered enthalpy equation reduces to

$$\frac{\partial}{\partial t}\left(\overline{\rho}\widetilde{h}\right) + \frac{\partial}{\partial x_j}\left(\overline{\rho}\widetilde{h}\widetilde{u_j}\right) = -\frac{\partial \widetilde{q_j}}{\partial x_j} - \frac{\partial}{\partial x_j}\left(\overline{\rho}\tilde{v}_{j,s}\tilde{h}_s\right) - C_V\frac{\partial q_{T,j}}{\partial x_j}. \tag{2.48}$$

If we ignore the diffusion of species with different enthalpies and assume a unit turbulent Lewis number,

$$\mathrm{Le_T} \equiv \frac{\mathrm{Sc_T}}{\mathrm{Pr_T}} = 1, \tag{2.49}$$

then the filtered enthalpy equation takes the same form as the filtered mass fraction equations, eqs. (2.32a). In the same manner as it was done for the unfiltered equations, we can group them together as

$$\frac{\partial \overline{\rho}\widetilde{\phi}_\alpha}{\partial t} + \frac{\partial \overline{\rho}\widetilde{u}_j\widetilde{\phi}_\alpha}{\partial x_j} = \frac{\partial}{\partial x_j}\left[-\rho\left(\Gamma + \Gamma_\mathrm{T}\right)\frac{\partial \widetilde{\phi}_\alpha}{\partial x_j}\right] + \rho\widetilde{S}_\alpha, \qquad \alpha = 1, 2, ..., N_s + 1. \tag{2.50}$$

where Γ_T represents both the turbulent mass diffusivity ($\mu_\mathrm{T}/\mathrm{Sc_T}$) and the turbulent heat conductivity ($\mu_\mathrm{T}/\mathrm{Pr_T}$).

2.3 Filtered mass density function (FMDF) for low Mach number flows

The objective of the filtered mass density function (FMDF) methodology is to provide an exact expression for the chemical source term for LES simulations, without neglecting the SGS contributions as it is done in eq. (2.36). To this aim, we consider the SGS fluctuations of the scalar array (the N_s species mass fraction plus enthalpy) in

a probabilistic manner by introducing their probability density function (PDF), which is dubbed the filtered mass density function and is denoted by $\mathcal{F}_L$. We then derive a transport equation that describes the evolution of $\mathcal{F}_L$ and solve it using an appropriate numerical method. The FMDF methodology belongs to the more general family of PDF methods, which have been originally developed and applied to Reynolds Averaged Navier-Stokes (RANS) simulations of chemically reacting flows. For a more in-depth presentation of these methods the reader is referred to Pope (1985).

In this section we describe the FMDF formulation for LES of density-varying, low Mach number flows as it was originally proposed by Jaberi et al. (1999). A proposed extension to take compressibility effects into account will be given in sec. 2.5.
The filtered mass density function is mathematically defined as

$$\mathcal{F}_L(\Psi;\mathbf{x},t) \equiv \int_{-\infty}^{+\infty} \rho(\mathbf{x'},t)\sigma[\Psi,\Phi(\mathbf{x'},t)]G(\mathbf{x'}-\mathbf{x})d\mathbf{x'}, \tag{2.51}$$

where G is the LES filter function introduced in eq. (2.29) and Ψ is the scalar vector in sample space, $\Phi(\mathbf{x'},t) = (c_1, c_2, ..., c_{N_s}, h)^T$. The fine-grained PDF, $\sigma\left[\Psi,\Phi(\mathbf{x'},t)\right]$, can be seen as the PDF of one realization of the flow and is defined as the product of Dirac delta functions for each scalar variable,

$$\sigma[\Psi,\Phi(\mathbf{x'},t)] \equiv \prod_{\alpha=1}^{N_s+1} \delta(\psi_\alpha - \phi_\alpha(\mathbf{x},t)). \tag{2.52}$$

The FMDF is the extension for variable-density flows of the filtered density function (FDF), originally introduced by Pope (1991). Equation (2.51) implies that the FMDF is the mass density spatially filtered value of the fine-grained density. In fact, by integrating over all composition domain,

$$\int_{-\infty}^{+\infty} \mathcal{F}_L(\Psi;\mathbf{x},t)d\Psi = \int_{-\infty}^{+\infty} \rho(\mathbf{x'},t)G(\mathbf{x'}-\mathbf{x})d\mathbf{x'} = \overline{\rho}(\mathbf{x},t), \tag{2.53}$$

the LES filtered density is recovered.
The conditional filtered average of any variable Q is defined as

$$\langle Q(\mathbf{x},t)|\Psi\rangle_L = \frac{1}{\mathcal{F}_L}\int_{-\infty}^{+\infty} \rho(\mathbf{x'},t)Q(\mathbf{x'},t)\sigma[\Psi,\Phi(\mathbf{x'},t)]G(\mathbf{x'}-\mathbf{x})d\mathbf{x'}. \tag{2.54}$$

Following directly from eq. (2.54):

1. For $Q(\mathbf{x},t) = c$, where c is a constant:

$$\langle Q(\mathbf{x},t)|\Psi\rangle_L = c \tag{2.55}$$

2. For $Q(\mathbf{x},t) = \hat{Q}(\Phi(\mathbf{x},t))$, where $\hat{Q}$ is a variable that is completely described by the compositional vector $\Phi(\mathbf{x},t) = (c_1, c_2, ..., c_{N_s}, h)^T$:

$$\langle Q(\mathbf{x},t)|\Psi\rangle_L = \hat{Q}(\Psi) \tag{2.56}$$

3. Integral property:

$$\int_{-\infty}^{+\infty} \langle Q(\mathbf{x},t)|\Psi\rangle_L \mathcal{F}_L(\Psi;\mathbf{x},t)d\Psi = \overline{\rho}(\mathbf{x},t)\widetilde{Q}(\mathbf{x},t). \tag{2.57}$$

From these properties it follows that the filtered value of any function of the scalar variables, such as the chemical source term, is obtained by integration over the composition space.

A transport equation that describes the evolution of the FMDF can be derived by taking the time derivative of the FMDF, eq. (2.51), and combining it with the filtered scalar transport equation, eq. (2.50). The details of the calculation can be found in Pope (1981) and only the final result is presented here:

$$\frac{\partial \mathcal{F}_L}{\partial t} + \frac{\partial \left[\langle u_j|\psi\rangle_\ell \mathcal{F}_L\right]}{\partial x_j} - \frac{\partial}{\partial \psi_\alpha}\left[\left\langle \frac{1}{\hat{\rho}(\phi)}\frac{J_j^\alpha}{\partial x_j}|\psi\right\rangle_\ell \mathcal{F}_L\right] + \frac{\partial}{\partial \psi_\alpha}\left[\hat{S}_\alpha(\psi)\mathcal{F}_L\right] = 0. \tag{2.58}$$

From this equation we see that the FMDF evolves in time because of convection in physical space (second term), diffusion (third term) and because of chemical reactions (last term). Both the convection and mixing terms are conditional averages that involve two-point correlations and need to be modeled. On the other hand, the chemical source term only requires one-point correlations and appears in closed form. The convection term is decomposed as

$$\langle u_j|\psi\rangle_\ell \mathcal{F}_L = \widetilde{u}_j\mathcal{F}_L + \left[\langle u_j|\psi\rangle_\ell - \widetilde{u}_j\right]\mathcal{F}_L, \tag{2.59}$$

while the mixing term, using Fick's law and the assumption of constant molecular diffusion, becomes

$$\begin{aligned}\frac{\partial}{\partial\psi_\alpha}\left[\left\langle\frac{1}{\hat{\rho}(\phi)}\frac{\partial}{\partial x_i}\rho\Gamma\frac{\partial\phi_\alpha}{\partial x_i}|\psi\right\rangle_\ell\mathcal{F}_L\right]=&\frac{\partial}{\partial x_i}\left(\rho\Gamma\frac{\partial(\mathcal{F}_L/\hat{\rho})}{\partial x_i}\right)-\\&\frac{\partial^2}{\partial\psi_\alpha\psi_\beta}\left[\left\langle\rho\Gamma\frac{\partial\phi_\alpha}{\partial x_i}\frac{\partial\phi_\beta}{\partial x_i}\right\rangle_\ell\mathcal{F}_L/\hat{\rho}\right].\end{aligned}\tag{2.60}$$

By substituting eq. (2.59) and eq. (2.60) into the FMDF transport equation (2.58), we obtain

$$\begin{aligned}\frac{\partial\mathcal{F}_L}{\partial t}+\frac{\partial}{\partial x_j}\left[\widetilde{u}_j\mathcal{F}_L\right]+\frac{\partial}{\partial x_i}\left[\gamma\frac{\partial(\mathcal{F}_L/\hat{\rho})}{\partial x_i}\right]=&-\frac{\partial^2}{\partial\psi_\alpha\psi_\beta}\left[\left\langle\gamma\frac{\partial\phi_\alpha}{\partial x_i}\frac{\partial\phi_\beta}{\partial x_i}\right\rangle_\ell\mathcal{F}_L/\hat{\rho}\right]\\&-\frac{\partial\left[\langle u_j|\psi\rangle_\ell-\langle u_j\rangle_L\right]\mathcal{F}_L}{\partial x_j}-\frac{\partial}{\partial\psi_\alpha}\left[\hat{S}_\alpha(\psi)\mathcal{F}_L\right].\end{aligned}\tag{2.61}$$

This equation is still an exact transport equation for the FMDF. The second and third terms on the left-hand side represent convection and diffusion in physical space, respectively, and they are closed. The last term on the right-hand side is the chemical source term and it is also closed. The unclosed terms are the first and second terms on the right-hand side, and they represent the effects of SGS mixing and convection, respectively.

The convection term is modeled adopting a gradient diffusion hypothesis:

$$\left[\langle u_j|\psi\rangle_\ell-\widetilde{u}_j\right]\mathcal{F}_L=-\rho\Gamma_T\frac{\partial(\mathcal{F}_L/\overline{\rho})}{\partial x_j}.\tag{2.62}$$

The advantage of this choice is that the first moment of eq. (2.62),

$$\overline{\rho}\left[\widetilde{u_j\phi_\alpha}-\widetilde{u}_j\widetilde{\phi}_\alpha\right]=-\rho\Gamma_T\frac{\partial\widetilde{\phi}_\alpha}{\partial x_j},\tag{2.63}$$

is identical to the SGS closure adopted in LES, cfr. eq. (2.50).

The closure adopted for the mixing term is based on the Interaction by Exchange with the Mean (IEM) model:

$$\frac{\partial^2}{\partial\psi_\alpha\psi_\beta}\left[\left\langle\gamma\frac{\partial\phi_\alpha}{\partial x_i}\frac{\partial\phi_\beta}{\partial x_i}\right\rangle_\ell\mathcal{F}_L/\hat{\rho}\right]=-\frac{\partial}{\partial\psi_\alpha}\left[\Omega_m(\psi_\alpha-\widetilde{\phi}_\alpha)\mathcal{F}_L\right],\tag{2.64}$$

where Ω_m is the SGS mixing frequency and is modeled as

$$\Omega_m(\mathbf{x},t) = \frac{C_\Omega(\Gamma+\Gamma_T)}{\Delta^2}, \tag{2.65}$$

where Δ is the filter width. It is worth noting that IEM is known to have some limitations as shown by Pope (2000) and several other mixing models have been developed. A good review and comparison of the current available micromixing models is given by Meyer and Jenny (2009). In this present work we chose not to investigate the effects of using different mixing models but decided to only employ IEM, as it is the most widely used in the community.

To establish consistency between the FMDF and conventional moment closure, an additional minor assumption is made

$$\frac{\partial}{\partial x_i}\left(\rho\Gamma\frac{\partial(\mathcal{F}_L/\hat{\rho})}{\partial x_i}\right) \approx \frac{\partial}{\partial x_i}\left(\rho\Gamma\frac{\partial(\mathcal{F}_L/\overline{\rho})}{\partial x_i}\right). \tag{2.66}$$

Using this assumption and the closures given by eq. (2.62) and (2.64), the modeled FMDF transport equation becomes

$$\begin{aligned}\frac{\partial\mathcal{F}_L}{\partial t} + \frac{\partial\left[\langle u_j|\psi\rangle_\ell\,\mathcal{F}_L\right]}{\partial x_j} = &-\frac{\partial}{\partial x_i}\left(\rho\Gamma\frac{\partial(\mathcal{F}_L/\overline{\rho})}{\partial x_i}\right) + \frac{\partial}{\partial\psi_\alpha}\left[\Omega_m(\psi_\alpha-\widetilde{\phi}_\alpha)\mathcal{F}_L\right]\\ &- \rho\Gamma_T\frac{\partial(\mathcal{F}_L/\overline{\rho})}{\partial x_i} - \frac{\partial}{\partial\psi_\alpha}\left[\hat{S}_\alpha(\psi)\mathcal{F}_L\right].\end{aligned} \tag{2.67}$$

The first and second central moments of eq. (2.67) are, respectively,

$$\frac{\partial\overline{\rho}\widetilde{\phi}_\alpha}{\partial t} + \frac{\partial\overline{\rho}\widetilde{\phi}_\alpha\widetilde{u}_j}{\partial x_j} = \frac{\partial}{\partial x_j}\left[\overline{\rho}\left(\Gamma+\Gamma_T\right)\frac{\partial\widetilde{\phi}_\alpha}{\partial x_j}\right] + \overline{\rho}\widetilde{S}_\alpha, \tag{2.68}$$

$$\begin{aligned}\frac{\partial\overline{\rho}\sigma_\alpha^2}{\partial t} + \frac{\partial\overline{\rho}\sigma_\alpha^2\widetilde{u}_j}{\partial x_j} = &\frac{\partial}{\partial x_j}\left[\overline{\rho}\left(\Gamma+\Gamma_T\right)\frac{\partial\sigma_\alpha^2}{\partial x_j}\right] + 2\overline{\rho}\left(\Gamma+\Gamma_T\right)\left[\frac{\partial\widetilde{\phi}_\alpha}{\partial x_j}\frac{\partial\widetilde{\phi}_\alpha}{\partial x_j}\right]\\ &- 2\overline{\rho}\Omega_m\sigma_\alpha^2 + 2(\widetilde{\phi_\alpha S_\alpha} - \overline{\rho}\widetilde{\phi}_\alpha\widetilde{S}_\alpha),\end{aligned} \tag{2.69}$$

where the SGS variance is defined as $\sigma_\alpha^2 = \widetilde{\phi_\alpha^2} - \widetilde{\phi}_\alpha\widetilde{\phi}_\alpha$. The equation for the first moment of the FMDF is identical to the filtered scalar equation, eq. (2.50), thus showing

the consistency of the method and of the closures adopted. We can directly solve eqs. (2.68) and (2.69) using a conventional numerical scheme and compare the results with the first two moments obtained from the FMDF. This redundancy provides a good test to check the numerical consistency of the FMDF formulation, as we show in chapter 4.

2.4 Monte Carlo solution of the FMDF

Because of the high dimensionality of the FMDF transport equation, eq. (2.67), conventional finite difference or finite volume numerical methods are impractical to use for solving it. Instead, in the same manner as it is done in other areas where high-dimensional equations are encountered, such as the Boltzmann equations, we employ a stochastic Monte Carlo procedure. The justification for using a stochastic particle method to solve the FMDF transport equation comes from the principle of equivalent systems stated by Pope (1985): "Many different systems of particles evolve with the same PDF". This principle is used to construct a system of *stochastic* particles whose evolution is simply computed and in which the PDF evolves in the same manner as the PDF of the system of fluid particles. This set of stochastic particles can be implemented either in an Eulerian or Lagrangian fashion. Fox (2003), Colucci (1998) and many other authors have shown that the Eulerian formulation is very dissipative and cannot be used for high-resolution LES simulations. For this reason we employ a Lagrangian formulation which, although more involved to implement on unstructured grids, considerably reduces the artificial diffusion of the method.

The domain is filled with the stochastic particles which move in space because of convection - due to the mean filtered velocity - and because of the effects of molecular and turbulent diffusion. In addition, the particles can change their composition due to mixing and due to chemical reactions.

The physical motion is governed by the general diffusion process as described in Risken (1989) and Gardiner (2009),

$$dX_i = D_i(X(t), t)dt + E(X(t), t)dW_i, \tag{2.70}$$

where X_i is the Lagrangian position of the particle, D_i and E are the drift and diffusion coefficients, respectively, and dW_i denotes the Wiener-Levy process. These coefficient

are derived by comparing the Fokker-Planck equation corresponding to eq. (2.70) with the spatial derivative terms in the FMDF transport equation, eq. (2.67), and are

$$D_i(X(t),t) = \widetilde{u}_i + \frac{1}{\overline{\rho}}\frac{\partial \overline{\rho}(\Gamma + \Gamma_T)}{\partial x_i}; \qquad E(X(t),t) = \sqrt{2(\Gamma + \Gamma_T)}. \tag{2.71}$$

The subgrid mixing and chemical reaction terms are implemented by altering the composition of the particles through the following ordinary differential equation,

$$\frac{d\phi_\alpha^+}{dt} = -\Omega_m(\phi_\alpha^+ - \widetilde{\phi}_\alpha) + \hat{S}_\alpha(\phi_\alpha^+), \tag{2.72}$$

where ϕ_α^+ denotes the scalar value of the particle at the Lagrangian position X_i. In eq. (2.72) we already used the IEM mixing model. As previously discussed, the principle of equivalent systems ensures that the solutions of eq. (2.70) and (2.72) yield the same statistics as solving directly the FMDF transport equation, eq. (2.67).

2.5 FMDF for compressible flows

The methodology described in sec. 2.3 assumes that the total pressure and viscous dissipation terms in the static enthalpy equation, eq. (2.7), are negligible and does not account for them. This simplified form of the enthalpy equation, eq. (2.24), has the same mathematical form of the mass fraction equations so that the FMDF formulation can be used for all the scalars ϕ_α (N_s species mass fractions plus enthalpy). This assumption is only valid for low Mach number flows. For compressible, high Mach number cases, the effects of the pressure variation and the viscous dissipation cannot be neglected and must be included in the formulation. This can be achieved by including these two contributions in the source term of the enthalpy equation. The mass fraction/enthalpy equation is unchanged (cfr. eq. (2.25):

$$\frac{\partial \rho\phi_\alpha}{\partial t} + \frac{\partial \rho u_j \phi_\alpha}{\partial x_j} = -\frac{\partial J_j^\alpha}{\partial x_j} + \rho S_\alpha, \qquad \alpha = 1, 2, ..., N_s + 1, \tag{2.73}$$

but now the source term S_α is

$$S_\alpha = \begin{cases} \dot{\omega}_\alpha & \text{for } \alpha = 1, ..., N_s \\ \frac{1}{\rho}\left(\frac{\partial p}{\partial t} + u_i \frac{\partial p}{\partial x_i} + \sigma_{ij}\frac{\partial u_i}{\partial x_j}\right) & \text{for } \alpha = N_s + 1 \end{cases} \tag{2.74}$$

After filtering eq. (2.73) and (2.74), we follow a procedure very similar to the one detailed in the previous section in order to derive the compressible FMDF transport equation. This is the same as the low Mach number one, eq. (2.67), with additional conditional averages that stems out of the pressure and viscous dissipations terms. Due to the lack of suitable models for these new terms, we follow the work of Banaeizadeh et al. (2011) and write them as

$$\left\langle \left(\frac{1}{\rho}\frac{\partial p}{\partial t}\right) | \psi \right\rangle_\ell \mathcal{F}_L = \frac{1}{\overline{\rho}}\left(\frac{\partial \overline{p}}{\partial t}\right)\mathcal{F}_L, \tag{2.75}$$

$$\left\langle \left(\frac{1}{\rho} u_i \frac{\partial p}{\partial x_i}\right) | \psi \right\rangle_\ell \mathcal{F}_L = \frac{1}{\overline{\rho}}\left(\widetilde{u}_i \frac{\partial \overline{p}}{\partial x_i}\right)\mathcal{F}_L, \tag{2.76}$$

$$\left\langle \left(\frac{1}{\rho}\sigma_{ij}\frac{\partial u_i}{\partial x_j}\right) | \psi \right\rangle_\ell \mathcal{F}_L = \frac{1}{\overline{\rho}}\left(\widetilde{\sigma}_{ij}\frac{\partial \widetilde{u}_i}{\partial x_j}\right)\mathcal{F}_L. \tag{2.77}$$

What eqs. (2.75) to (2.77) entail is that the SGS contribution of the pressure and viscous dissipation is neglected and only the filtered part is retained in the formulation. The filtered source term is thus

$$\widetilde{S}_\alpha = \begin{cases} \widetilde{\omega}_\alpha & \text{for } \alpha = 1, ..., N_s \\ \frac{1}{\overline{\rho}}\left(\frac{\partial \overline{p}}{\partial t} + \widetilde{u}_i \frac{\partial \overline{p}}{\partial x_i} + \widetilde{\sigma}_{ij}\frac{\partial \widetilde{u}_i}{\partial x_j}\right) & \text{for } \alpha = N_s + 1 \end{cases} \tag{2.78}$$

At this point it is unclear whether these contributions are significant or not in high speed flows and further investigations will be needed in order to assess the validity of these assumptions. If the SGS effects of pressure are to be included in the FMDF formulation, due to the lack of universal models, a possible solution would be to use the pressure-velocity-scalar filtered density function outlined by Sheikhi et al. (2009).

Chapter 3

Numerical methodology

The numerical solution of the governing equations is based on a hybrid methodology in which the LES equations, eqs. (2.32), are solved using an unstructured, parallel, finite-volume scheme, while the FMDF transport equation, eq. (2.67), is solved with a stochastic, Lagrangian Monte Carlo (MC) procedure. The main advantage of this hybrid approach is that it combines the strengths of both methods. A purely stochastic Monte Carlo simulation, where both the momentum and turbulence equations are also treated with FDF methods, is known to produce results that are heavily affected by stochastic noise and that could have negative impacts on the overall numerical stability. Conversely, a purely conventional LES produces much smoother results but does not have any sub-grid information about the scalar distribution and tends to over predict the amount of molecular mixing, as we show in chapter 5 and 6.

The solver we employed for the solution of the compressible Navier-Stokes equations is US3D[1], a three-dimensional, unstructured, parallel finite volume code which has been developed at the University of Minnesota. We present some of US3D's main characteristics in the first section of this chapter, focusing especially on those that are relevant for this work. For a more detailed description of the structure and capabilities of US3D the reader is referred to Nompelis et al. (2004) and Nompelis et al. (2005). Next we describe in much more details the Monte Carlo[2] procedure that was newly developed for this application. We place more emphasis on the MC solver as compared to the FV

[1]The acronym stands for UnStructured 3D.

[2]Unfortunately we did not coin any name for the MC solver.

because it represents an original addition to the US3D code by this work. We therefore touch upon some of the implementation challenges we faced and how we addressed them, such as reliably tracking particles on 3D unstructured grids and making the code fully parallel by using domain decomposition. Finally, in the last section, we outline the strategy we employed to couple the two codes. Using this hybrid procedure results in the creation of redundant variables, i.e. some physical quantities are calculated by both solvers. This redundancy, far from being a waste of resources, can be exploited to verify the consistency of the FV/FMDF formulation, as we show in chapter 4.

3.1 Finite volume solver

The compressible Navier-Stokes equations, eqs. 2.1, can be written in compact form as

$$\frac{\partial U}{\partial t} + \nabla \cdot \left(\overrightarrow{F}_I - \overrightarrow{F}_V \right) = W. \tag{3.1}$$

In the above expression $U = (\rho_1, \rho_2, ..., \rho_{N_s}, \rho u, \rho v, \rho w, E)^T$ is the vector of conserved variables, the fluxes have been split into their inviscid ($\overrightarrow{F}_I$) and viscous components ($\overrightarrow{F}_V$), and W is the source term defined as,

$$W \equiv \begin{pmatrix} \omega_1 \\ \omega_2 \\ \vdots \\ \omega_{N_s} \\ 0 \\ \vdots \\ 0 \end{pmatrix}, \tag{3.2}$$

where the ω_s are the chemical source terms corresponding to species s, eq. (2.16). The source terms for the momentum and total energy equations are identically zero. The finite volume method consists of splitting the computational domain into smaller domains, called elements or cells, and use the divergence theorem to relate the rate of

change of U to the sum of the fluxes across each face of the element,

$$\frac{\partial \overline{U_i}}{\partial t} = -\frac{1}{\mathcal{V}_i} \sum_{faces} \left[(F'_I - F'_V) S \right] + \overline{W_i}. \tag{3.3}$$

The above expression is the semi-discrete version of the governing equations where the over line denotes the average value of the variable inside the element i, S is the face area, $\mathcal{V}_i$ is the volume of the cell, and the summation is for every face of the element. The prime means that the fluxes have been dotted with the face unit outward-pointing normal, $F' = \overrightarrow{F} \cdot \hat{n}$. The unstructured finite volume solver we used in this work, US3D, stores the variables at the cell centroids and can support four types of element: tetrahedra, pyramids, prisms and hexahedra.

The FV code is able to run on multiple cores by using a domain decomposition technique. In the pre-processing phase, the total domain is divided into subdomains by the METIS algorithm (George and Vipin (1995)) and each is assigned to a different processor. Whenever needed, neighboring processors exchange the data that is necessary to calculate the gradients or the higher-order stencils. It is needless to say that the parallelization of the code is an indispensable feature in order to being able to simulate cases of practical interest.

3.1.1 Inviscid fluxes

The inviscid part of the fluxes can be calculated using the modified flux vector splitting method of Steger-Warming, which is reviewed in MacCormack and Candler (1989), and reads

$$F_I = \left(R \Lambda^+ R^{-1} \right)_f \cdot U_L + \left(R \Lambda^- R^{-1} \right)_f \cdot U_R, \tag{3.4}$$

where R and R^{-1} are the right and left eigenvector matrices of the flux Jacobian, $A = \partial F' / \partial U$, and Λ^+ and Λ^- are the diagonal matrices that contain the positive and negative eigenvalues of A, respectively. The subscript f means that the quantities inside the parenthesis are calculated using averaged values at the face, while U_L and U_R denotes the vector of conserved variables coming from the "left" or "right" of the face, thus making the method truly upwind. If the immediate neighboring elements are used for U_L and U_R the method is first order accurate in space but commonly a higher order

TVD-MUSCL reconstruction is used (Yee (1989)).

Even using this higher order reconstruction upwind schemes, an excessive amount of dissipation for LES-type of applications is introduced in the computation. For this reason the code allows the use of high-order, symmetric schemes that are "4th" and "6th" order accurate on Cartesian mesh as was demonstrated by Bartkowicz (2012) for one-dimensional problems. The idea behind these schemes is to increase the stencil size by using the cell-centered gradients which are always computed for the evaluation of the viscous fluxes. As an example, if we want to compute the flux at the face $i + 1/2$ and we only have connectivity information of the neighboring elements i and $i + 1$, we can derive a fourth-order accurate method as

$$U_{i+1/2} = \alpha \left(U_i + U_{i+1}\right) + \beta \Delta x \left(\frac{\partial U}{\partial x} + \frac{\partial U}{\partial x}\right), \tag{3.5}$$

where Δx is the (locally) uniform grid spacing and $\alpha = 1/2$, $\beta = 1/3$. If we have connectivity information also to the next set of elements, $i + 2$ and $i - 1$, we can follow the same procedure to develop a sixth-order accurate reconstruction for the inviscid fluxes. It is clear that the "6th" order gradient reconstruction works better when the grid points in the stencil are aligned (local 1D reconstruction) and when they are of similar size, i.e. when the grid stretching is not excessive. Whenever either one or both of these conditions are violated in some parts of the domain, the method might not perform as well as expected and one should resort to lower order schemes.

A very important point that needs to be stressed is the fact that these high order gradient reconstruction methods are all symmetric and they are prone to be unstable in the presence of strong gradients such as shock waves. In order to preserve a shock capturing capability a dissipative part has to be added to the inviscid fluxes,

$$F_I = F_{sym} + \alpha_{diss} F_{diss}, \tag{3.6}$$

where $\alpha_{diss} \in [0, 1]$ is a switch that turns on or off the dissipative portion. Ideally the switch should be close to zero in smooth regions and only be active ($\alpha_{diss} \approx 1$) in the presence of shock waves. The mathematical form of the switch we use, suggested by

Ducros et al. (2000), is

$$\alpha_{diss} = \min\left(\frac{\theta^2}{\theta^2 + \omega^2 + \epsilon}, 1\right), \tag{3.7}$$

with θ being the divergence of the velocity, ω the vorticity magnitude and ϵ a small number to prevent division by zero. In regions characterized by strong compressibility, the divergence dominates against the vorticity magnitude and the value of α_{diss} is close to one. The opposite is true in smooth regions dominated by turbulence, where we want the dissipation portion to be as small as possible to avoid dissipating the turbulent structures. For the dissipative fluxes, F_{diss}, we use the upwind portion of the Steger-Warming method. As noted in Subbareddy and Candler (2009), eq. (3.4) can be rearranged into

$$F_I = \left(R\Lambda^+R^{-1}\right)_f \cdot \left(\frac{U_L + U_R}{2}\right) - \frac{1}{2}\left(R|\Lambda|R^{-1}\right)_f \cdot (U_R - U_L), \tag{3.8}$$

where we decomposed the Steger-Warming flux into its symmetric (first term on the right hand side) and its upwind part (second term on the r.h.s.). It is this latter portion that is used for the dissipative fluxes, F_{diss}, in eq. (3.6).

3.1.2 Viscous fluxes

The viscous fluxes are calculated exactly provided that the gradients of the variables of interest are known at each face. In US3D, the cell-centered gradients are computed using a least squares (LS) fit, which is weighted using the inverse distance between elements, as described by Mavriplis (2003). Only the cell-centered data of the elements that share a face with the current element are included in the stencil. The LS method fits a hyperplane to all the data points that belong to the stencil by solving a linear system of equations at each element. In the absence of gird deformation, the linear operator can be calculated once, inverted and then stored at start-up. The least squares fit is particularly suitable for unstructured grids. The face-centered gradients are then obtained by averaging the cell-centered ones.

3.1.3 Time integration

Once the explicit inviscid and viscous fluxes have been evaluated, eq. (3.3) needs to be discretized and integrated in time. US3D allows the use of both explicit and implicit methods for the time advancement of the equations. Implicit methods become essential whenever we face a problem with solid walls as the tiny viscous spacing that is required near the wall to capture the boundary layer makes any explicit calculation unfeasible. Implicit methods have their drawbacks because they are usually not time-accurate and thus not optimal for unsteady simulations. In this work, as we mostly deal with LES of unsteady free flows, we only employed explicit time integration schemes. In particular, we used the third order, 'strong-stability-preserving' explicit Runge-Kutta scheme due to Shu and Osher (1988). It must be noted, however, that in the case of very stiff chemistry source terms, explicit methods limit the range of cases that can be simulated, as we discuss both at the end of next section and in chapter 6.

3.2 Monte Carlo solver

As described in sec. 2.4, we solve the FMDF transport equation using a Lagrangian "grid-free" Monte Carlo (MC) scheme. This procedure employs a certain number of stochastic particles that undergo motion in physical space and whose composition changes with time because of the effects of mixing and chemical reactions. The term grid-free refers to the fact that, in theory, no computational grid is required for the Monte Carlo solver, as the particles are free to move in space in a Lagrangian fashion. In practice, we do require some reference grid in order to evaluate some statistical moments, as we will explain later in this section. Two different approaches can be pursued: either we create a different grid for the MC solver or we take advantage of the computational grid that is used by the CFD code. In this work we employ the latter solution, which has the advantages of requiring less memory, being less intrusive in the original CFD code, and taking advantage of the fact that the FV grid is already clustered in regions of large gradients.

In order to numerically solve the FMDF transport equation, we employ a splitting operation: we treat advection and diffusion in physical space as a separate step as compared to the change in compositional space. In particular, at every time step, we

perform three main operations:

1. Each particle is moved to a new position determined by the stochastic differential equations of eq. (2.70) . This step requires tracking the particle on the unstructured grid.

2. Ensemble averages are collected.

3. Particle composition is changed due to the mixing model and chemical reactions.

We will now describe in detail each of these steps.
The stochastic differential equations, eqs. (2.70), are explicitly integrated in time using the Euler-Maruyamma approximation,

$$X_i^{(n)}(t_{k+1}) = X_i^{(n)}(t_k) + D_i^{(n)}(t_k)\Delta t + E^{(n)}(t_k)(\Delta t)^{1/2}\xi^{(n)}(t_k), \tag{3.9}$$

where $X_i^{(n)}(t_{k+1})$ and $X_i^{(n)}(t_k)$ are the new and old particle position, respectively, and $\Delta t = t_{k+1} - t_k$ is the simulation time step. The drift and diffusion coefficients, $D_i^{(n)}(t_k) = D_i(X_i^{(n)}(t), t)$ and $E^{(n)}(t_k) = E(X_i^{(n)}(t), t)$, are given by eq. (2.71) and are evaluated at the particle location, while $\xi^{(n)}$ is a random variable with a standard Gaussian probability density function (zero mean value and unit variance). According to Gickhman (1974) this formulation preserves the Markovian character of the diffusion process. Although conceptually very simple, this step is probably the most difficult to implement in a robust and efficient way in an unstructured framework where the computational domain is split among multiple processors. We provide the details of the strategy we used to achieve this in sec. 3.2.1.
Note that the numerical solution given by eq. (3.9) is first-order accurate in time. Higher-order numerical schemes for its solution have been developed (Kloeden and Platen (1992)) but they usually require derivatives of the coefficients and we have not investigated them here.

The filtered velocities and turbulent fields that appear in the drift and diffusion coefficients of eq. (3.9) are interpolated to the particle position using the gradients that are available at the cell center,

$$\theta_p = \theta_i + (\nabla\theta)_i \cdot (\mathbf{r}_i - \mathbf{r}_p), \tag{3.10}$$

where θ is a generic variable known at the cell centroid and $\mathbf{r}_i - \mathbf{r}_p$ is the position vector that connects the particle (subscript p) to the cell centroid (subscript i).

The next step in the simulation is to build an estimator of the statistics for the variables of interest, usually chemical composition and temperature from the ensemble of particles. This procedure is called particle-field estimation and, according to Fox (2003), one of the most suitable ways of doing it is to use a kernel function $h(\mathbf{x})$ of the form,

$$h_{\Delta_E}(\mathbf{x}) = \begin{cases} 1 & \text{if } \mathbf{x} \in \Delta_E \\ 0 & \text{otherwise} \end{cases} \tag{3.11}$$

so that only the particles that are currently inside a certain "spatial bin" of characteristic length Δ_E, called the ensemble domain, are considered for the estimation of the statistics. For example, using eq. (3.11), the estimated first statistical moment of any quantity $Q(\phi)$ (its Favre-averaged mean) is given by

$$\widetilde{Q} \approx \frac{\sum_{p \in \Delta_E} w^{(p)} \hat{Q}(\phi^{(p)})}{\sum_{p \in \Delta_E} w^{(p)}}, \tag{3.12}$$

where $w^{(p)}$ is the particle weight which will be described in section 3.2.2. The ensemble domain is where the FMDF is discretely represented and where all the statistical quantities of interest are calculated. It can have any arbitrary shape although we only consider hexahedron and spherical domains that are centered around the cell centroid. A finite size domain is required by the fact that, with probability one, no particles will coincide with the point, as demonstrated by Pope (1985). Numerically, the specification of the size of the ensemble domain is an important issue because it is a trade-off between two conflicting requirements. Ideally, it is desired that $\Delta_E \to 0$ to reduce artificial diffusion, while the number of particles inside the ensemble domain should be infinitely large to avoid statistical error. A compromise between statistical accuracy and diffusive accuracy has to be find and an optimum value for Δ_E cannot be specified *a priori*. We performed some simulations on three-dimensional mixing layers using different sizes for Δ_E (see fig. 3.1) in order to test the sensitivity of the solution on this parameter. The results are shown in chapter 4.

The last step in the Monte Carlo simulation of the FMDF transport equation is

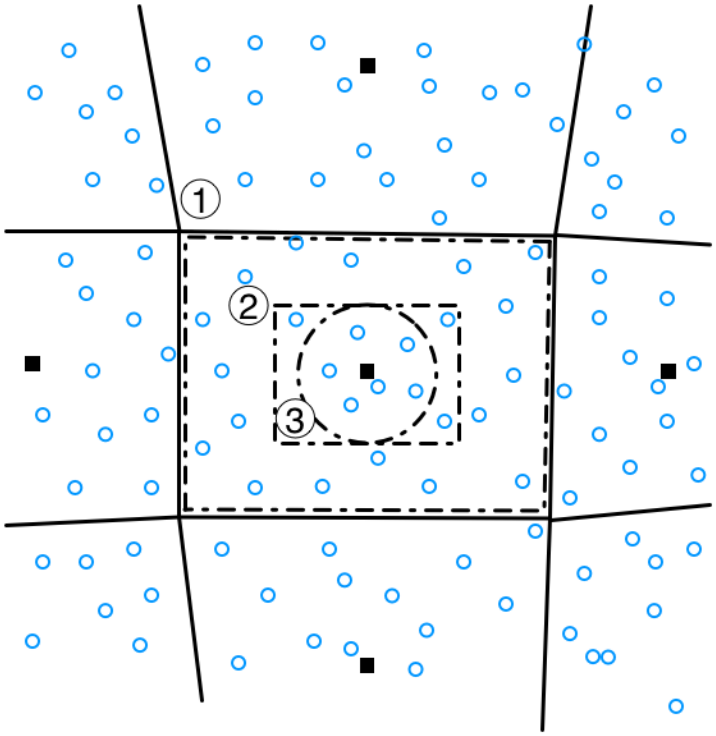

Figure 3.1: Schematic of three possible ensemble domain sizes (dashed-dotted lines). 1. Full FV element; 2. Half FV element; 3. Sphere of diameter corresponding to half element. Black squares denotes element centroids while the circles represent MC particles.

to calculate the change of composition of the particles due to mixing and chemical reactions. The evolution of the particles' composition is given by eq. (2.72)

$$\frac{d\phi_\alpha^{(p)}}{dt} = -\Omega_m(\phi_\alpha^{(p)} - \widetilde{\phi}_\alpha) + \hat{S}_\alpha, (\phi_\alpha^{(p)}) \tag{3.13}$$

in which the superscript p denotes the value of ϕ that pertains to the single particle and Ω_m is the mixing frequency given by eq. (2.65). This ordinary differential equation is integrated in time by decoupling the chemical source term from the molecular mixing term. The mixing model is advanced first by using a first-order explicit Euler method,

$$(\phi_\alpha^{(p)})^{n+1} = (\phi_\alpha^{(p)})^n - \Omega_m \left[(\phi_\alpha^{(p)})^n - \widetilde{\phi}_\alpha\right] \Delta t, \tag{3.14}$$

where Δt is the same time step used by the FV solver and $\widetilde{\phi}_\alpha$ is the Favre-averaged

mean obtained using eq. (3.12). Alternatively, when only the mixing term is present, eq. (2.72) admits the analytical solution,

$$\phi_\alpha^{(p)} = (\phi_\alpha^{(p)})_0 \exp\left(-\Omega_m t\right). \tag{3.15}$$

We employed both integration methods and did not find any significant differences between the solutions.

After the fractional mixing step is completed, the particle compositions are advanced because of the effect of chemical reactions. This step can be formally written as

$$(\phi_\alpha^{(p)})^{n+1} = (\phi_\alpha^{(p)})^n + \int_t^{t+\Delta t} \omega_s \left((\phi_\alpha^{(p)}(\tau)\right) d\tau. \tag{3.16}$$

As already noticed in sec. 2.1.2, the chemical source term ω_s is a highly non-linear function of the species mass fractions and temperature and it is usually numerically very stiff. It can therefore place a severe constraint on the time step that can be used to integrate eq. (3.16) explicitly, especially for fast reactions. In fact, one of the advantages of performing the chemical reaction step last is to allow fast chemical reactions to return to their "local equilibrium" states (Fox (2003)).

3.2.1 Particle tracking on 3D unstructured meshes

The hybrid coupling between the Eulerian finite volume fluid solver and the Lagrangian Monte Carlo method requires every stochastic particle to be univocally associated with a grid element at any simulation time. For this purpose a robust and efficient algorithm which is able to track particles on arbitrary three-dimensional unstructured mesh is needed. In this work we employ the *convex polyhedron* method proposed by Subramaniam and Haworth (2000) with some small modifications. This method is well suited for a face-based data structure like the one used by the fluid solver. The computational domain is decomposed into arbitrary non-overlapping polyhedra, which coincides with the computational elements used by the fluid solver. In the following, each variable that is associated to a computational element will be denoted with a subscript i, whereas the subscript j will be used to denote variables linked to a face. Each element has $N_f^{(i)}$ faces and a set of connectivity information that links each element to its faces. Each face

carries the location of its centroid x_c^j, a normal unit vector $\widehat{n}^j$ pointing outside of the element and a connectivity pointer with the indeces of the two neighboring elements. With reference to fig. 3.2, particle n, which initially has position $x^{(n)}(t)$ and belongs to

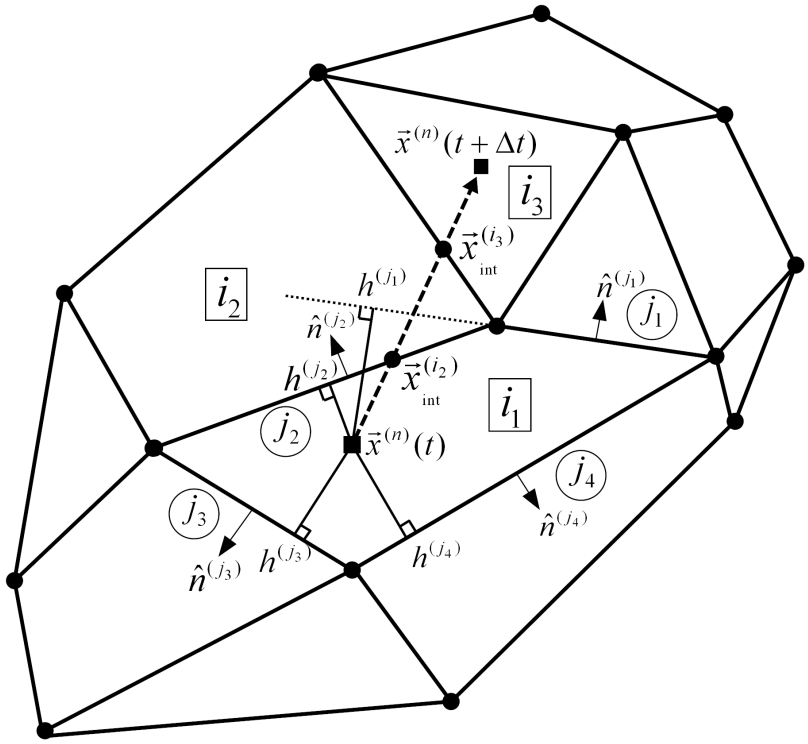

Figure 3.2: Two-dimensional example of particle tracking on unstructured meshes. Element i_1 has four faces denoted by j_1, j_2, j_3 and j_4.

element i_1 has to be moved to the new location $x^{(n)}(t+\Delta t)$, which is inside element i_3. The particle moves on a straight line and its velocity is $v^{(n)} = \Delta x/\Delta t$. The first step is to build, for all the four faces of element i_1, the particle-to-face-heights $h^{(j)}$. The time it will take for the particle to intersect the j^{th} face of i_1 is simply $t^{(j)} = h^{(j)}/(v^{(n)} \cdot \widehat{n}^j)$, where the denominator is the component of the particle velocity normal to the face. The minimum time to intersect one of the faces of i_1 is $t^{(i)}_{\min} = \min_{j=1}^{N_f(i_1)} \left[\max\left(0, t^{(j)}\right)\right]$. If $t^{(i_1)}_{\min} > \Delta t$ then the particle is still inside element i_1. If $t^{(i_1)}_{\min} < \Delta t$, the particle is moved to the intersection point of the face $x_{\text{int}} = x^{(n)}(t) + v^{(n)} t^{(i_1)}_{\min}$, its time step is decremented by $t^{(i_1)}_{\min}$ and appropriate actions can be taken depending on the type of

face it intersected. For example, if it is an internal face the particle element pointer is updated to the new element it now belongs to. If it is a boundary face, the appropriate boundary condition (symmetry, periodicity, inflow, outflow) can be easily assigned. In the example of fig. 3.2, the particle is first moved on $x_{\text{int}}^{(i_2)}$ and, as j_2 is an internal face, its element pointer is updated to i_2. The same procedure is repeated for all the faces of element i_2 and the particle is moved again on $x_{\text{int}}^{(i_3)}$ and its pointer updated to i_3. Now the remaining Δt is less than the minimum time to reach any of on i_3 faces and thus the particle will reach its final position $x^{(n)}(t + \Delta t)$.

3.2.2 Particle weights and clustering

Each Monte Carlo particle carries a weight $w^{(p)}$ that is representative of the amount of mass that it is carrying. It is of paramount importance to prescribe the correct weights both during the initialization phase and at the inflow condition, as discussed in the next section. Failure to do so will produce unphysical results. It is also worth noticing that, once they are initialized at the initial condition or at the inflow, individual particle weights are never changed during the simulation unless the particle clustering algorithm is employed.

The use of particle weights is also required when simulating variable-density flows (Jaberi et al. (1999)), because the estimation of the local density is a function of them,

$$\overline{\rho} \approx \frac{1}{\Delta V_E} \sum_{p \in \Delta_E} w^{(p)}, \tag{3.17}$$

and thus are all the other Favre-filtered variables because of eq. (3.12). In the previous expression, ΔV_E is the volume of ensemble domain. Equation (3.17) essentially provides a way of calculating the local mass density entirely from the particle field. This property would theoretically make superfluous the computation of the total density by the finite volume solver. Unfortunately, the density field that results from eq. (3.17) is affected by a large amount of statistical noise and would negatively affect the numerical stability of the simulations. Nevertheless, we can still compare the two density fields to qualitatively check the consistency of the FMDF formulation (see fig. 3.4). In chapter 4 we provide some examples of the inherent noisiness of eq. (3.17) and how it compares with the FV density. It is useful to note that eq. (3.17) only provides an estimate for $\overline{\rho}$ but that it

would be an exact expression in the limit of $\Delta_E \to 0$ and an infinite number of particles.

Finally, particle weights can be used to reduce the computational overhead and use the simulation particles more efficiently as noted by Fox (2003). Whenever the number of particles per cell exceeds upper or lower thresholds assigned by the user, particles can be "split" or "clustered" together and the newly created particles will have a combination of the weights of the old ones. In this work we implemented a clustering procedure to prevent particle accumulation in high density areas that could act as a bottleneck for the simulation and saturate the memory of that particular partition. The algorithm works as follows:

1. Detect whenever the number of particles (NPC) in one particular cell exceeds a certain user defined threshold ($\mathrm{NPC}_{\mathrm{thre}}$).

2. If $\mathrm{NPC} > \mathrm{NPC}_{\mathrm{thre}}$ the algorithm randomly selects two particles, p and p^*, from those that populate the cell and cluster them together as,

$$\begin{pmatrix} x_i \\ \phi \\ w \end{pmatrix}^{(p)} \quad \text{and} \quad \begin{pmatrix} x_i \\ \phi \\ w \end{pmatrix}^{(p^*)} \xrightarrow[cluster]{} \begin{pmatrix} x_i^{(m)} \\ \phi^{(m)} \\ w^{(p)} + w^{(p^*)} \end{pmatrix}^{(m)}, \tag{3.18}$$

   where $m = p$ with probability $w^{(p)}/(w^{(p)} + w^{(p^*)})$ and $m = p^*$ with probability $w^{(p^*)}/(w^{(p)} + w^{(p^*)})$.

3. Keep doing step 2 until the number of particles in that cell falls below the threshold, $\mathrm{NPC} \leq \mathrm{NPC}_{\mathrm{thre}}$.

Note that the position and composition of the new particle are *not* the weighted averages of the old particles as that would artificially increase the molecular mixing and bias the particle positions towards the cell center. Instead, the new particle inherits the position and composition of the old particle that is randomly selected but gets the sum of the old particles' weights so that the density inside the cell is conserved.

3.2.3 Initial and boundary conditions

At the beginning of each simulation, a user-defined initial number of stochastic particles per cell ($\mathrm{NPC}_{\mathrm{init}}$) is randomly distributed inside each element. The initial total number

of particles in the domain is thus $(\mathrm{N_p})_{\mathrm{init}} = \mathrm{NPC_{init}} \cdot \mathrm{N_{ele}}$, where $\mathrm{N_{ele}}$ is the total number of FV elements used in the simulation. Usually, for a constant density flow, to obtain converged statistics, $\mathrm{NPC_{init}}$ should be in the order of 40 or 50.
Each particle is given a weight that depends on the volume ($\mathcal{V}_i$) of the element in which it is created and on the local density,

$$w^{(p)} = \frac{\overline{\rho}\mathcal{V}_i}{\mathrm{NPC_{init}}}, \tag{3.19}$$

where $\overline{\rho}$ is the cell-center value of the mass density. Chemical concentrations and static enthalpy are also initialized using the cell-center values,

$$c_s^{(p)} = \widetilde{c}_s, \qquad h^{(p)} = \widetilde{C}_P\widetilde{T} + \widetilde{c}_s h_s^0. \tag{3.20}$$

The Monte Carlo solver is able to handle four types of boundary conditions which spans all the types of flows of interest. These are wall/symmetry, inflow, outflow, and periodic boundary.
We treat both solid walls or symmetric, velocity slip boundary conditions in the same manner. The particle is reflected back into the domain by inverting its velocity vector as sketched in fig. 3.3.

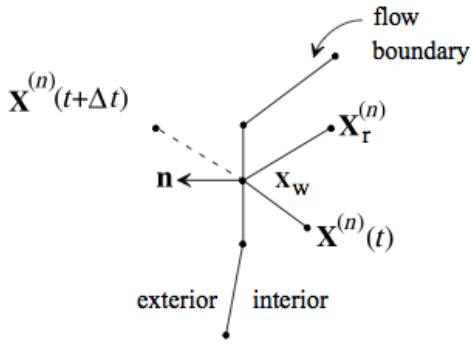

Figure 3.3: Sketch of a reflective boundary condition. Taken from Fox (2003).

In the case of an inflow boundary the mean velocity vector will point into the flow

domain. The total mass entering the domain during the time step Δt is

$$\Delta m_{in} = \rho_{in} S_{in} \widetilde{U}_{in} \Delta t, \tag{3.21}$$

where ρ_{in} and $\widetilde{U}_{in}$ are the density and mean velocity of the incoming flow and S_{in} is the inflow surface area. A fixed number of particles per inflow cell $\mathrm{NPC}_{\mathrm{inflow}}$ are added into the domain, each carrying a weight,

$$w^{(p)} = \frac{\Delta m_{in}}{\mathrm{NPC}_{\mathrm{inflow}}} \tag{3.22}$$

The new particles are placed at the inflow face centroid and their composition corresponds to the inflow composition. Because of the diffusion term in eq. (3.9), a particle may attempt to leave the domain even if it is an inflow. In this case the particle is reflected back inside the domain in the same way as in the wall/symmetry case.
At an outflow boundary the mean velocity vector will point out of the flow domain. All the particles that cross an outflow face are simply eliminated.
In the case of a periodic boundary condition, the particles are translated to the corresponding periodic face. In a simulation where only wall/symmetry and periodic boundary conditions are present, the total number of simulation particles is conserved.

3.2.4 Parallelization of the Monte Carlo code

The Monte Carlo solver shares the same domain partitioning that is used for the FV solver as described in sec. 3.1. Whenever a particle hits a face which lies on the boundary between two partitions, the particle is flagged for exchange, its position on the face is "frozen" and the remaining time it needs to complete its move is saved. At the end of the moving algorithm, sec. 3.2.1, all the particles that have been flagged are exchanged among processors and the particles finish their move in the new partition. The algorithm is able to handle the unlikely case of particles crossing multiple processors' boundaries during a single time step, thus increasing robustness.
It must be noted that the METIS algorithm generates the partitioning by minimizing some penalty functions like the latency of data transfers and load imbalances. Although this is very efficient for a standard finite volume calculation, it may not be ideal for the

Lagrangian MC solver as the particles tend to cluster in regions of high density and thus create some load imbalances. We show some of the effects of this issue in the results for the spatially developing mixing layer (chapter 6) where it is exacerbated by the relatively complex chemistry, as noted by Yilmaz (2009).
This problem is not unique to the FMDF methodology but it is common to most of the Lagrangian particle methods, such as Direct Simulation Monte Carlo (DSMC), as pointed out for example by Nompelis and Schwartzentruber (2013).

3.3 Coupling between the FV and the FMDF solver

The coupling between the two schemes is a crucial aspect of the hybrid methodology and a lot of care has to be used in order to obtain a consistent formulation. One important point to stress is that there is more than one possible approach to couple the two solvers. In the most basic coupling, the FMDF solver could provide the species mass fractions and the static enthalpy, and the FV solver would only need to solve the momentum and total density equations, eqs, (2.32b) and (2.31). Previous work done by Jaberi et al. (1999) found that solving for the energy only with FMDF results in a lot of statistical noise in the simulation, which has a detrimental effect on numerical stability. For this reason, it is preferable to solve an energy (or enthalpy) equation also with finite volume methods, as we do in this work. In addition, we use the finite volume solver also to solve the N_s partial density equations (eqs. (2.32a)), for which the chemical source term, if present, is provided by the FMDF code. As noted earlier this calculation is redundant because the FMDF solver is also providing the N_s species mass fractions and solving one single total mass equation with the FV solver would be sufficient. Nevertheless we choose this approach for two main reasons. Firstly, the original US3D code was designed to solve the N_s partial density equations and to obtain total density as $\rho = \sum_s \rho_s$ and we did not want to radically modify the architecture of the code. Secondly, solving the same equations with both the FV and FMDF methods provides an excellent consistency test to check the novel FMDF implementation against the well-established US3D results. As we discuss in chapters 4 and 5, the FMDF and FV solutions for the species mass fractions should be very close both for the case of non-reacting flows, for which $\omega_s = 0$, and for reacting flows, for which the source term

is calculated by the FMDF solver.

Figure 3.4 summarizes the main features of the present implementation of the hybrid finite volume/Monte Carlo (FV/MC) methodology. The finite volume code is used to

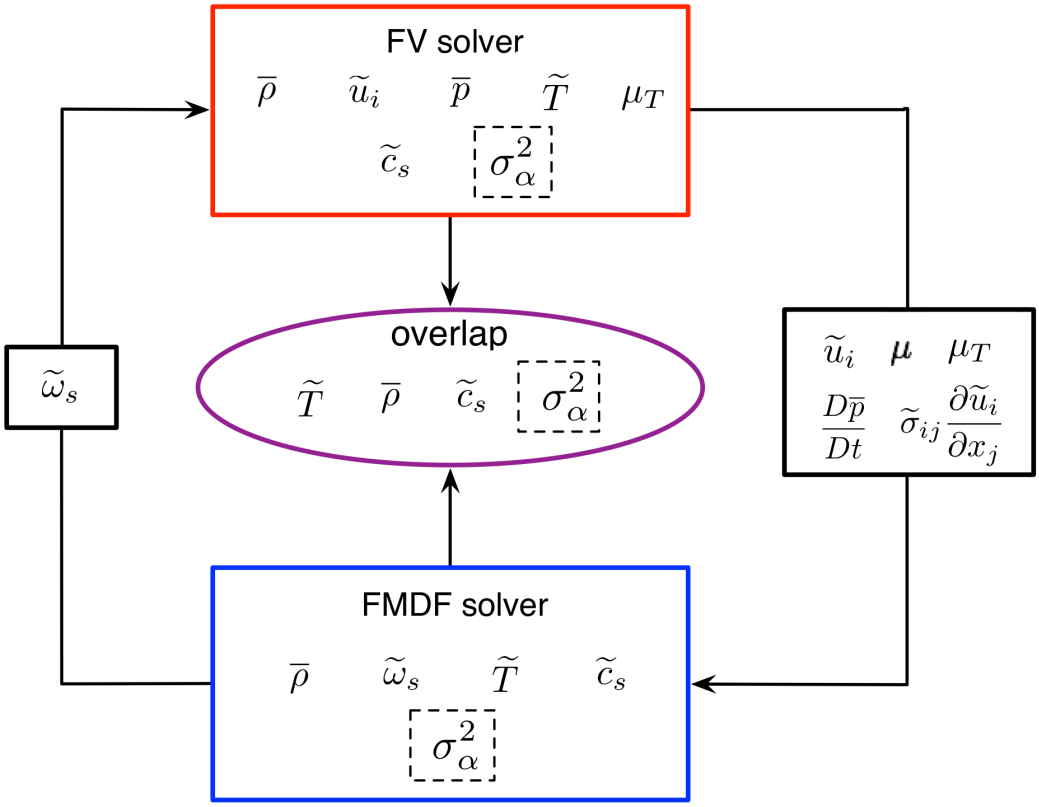

Figure 3.4: Diagram showing the basic coupling between the finite volume (FV) solver (LES-FV) and the FMDF one. Optionally the SGS variance (σ^2_α) can also be used for consistency check.

calculate the hydrodynamic variables (velocity, pressure, viscosity, eddy viscosity, total density), while the FMDF solver determines the scalar fields (species mass fraction and enthalpy) as well as the chemical source term. The FMDF solver receives from the FV solver the filtered velocity, the molecular and turbulent viscosity, the total derivative of the pressure and the viscous dissipation terms. It then feeds back to the FV solver the filtered chemical source term to be used in the partial density LES equations, eqs. (2.32a). The overlapping variables, which are calculated by both solvers, are the

filtered species mass fraction, the filtered temperature and the filtered total density[3]. Obviously the finite volume solver can only calculate the first statistical moment (filtered value) of any quantity. On the other hand the Monte Carlo solver, as it determines the whole probability density function of the SGS terms, can theoretically determine any arbitrary n^{th} moment. For certain test cases we also implemented the SGS variance equation in US3D, eq. (2.69), and we compared it with the variance obtained by the FMDF solver (dashed boxes in fig. 3.4). The results and a discussion on this test is given in chapter 4.

One advantage of the hybrid FV/FMDF formulation is that the coupling between the two procedures is minimal and this allowed us to develop the Monte Carlo routine as separate module from the FV code that can easily be switched on or off by the user. Operationally the simulation proceeds as depicted in the flow chart of fig. 3.5. The two steps (FV and FMDF) never overlap and proceed in a serial way. Only when the FV step is completely terminated the FMDF routine is called. At the beginning of the simulation, the FV variables are initialized based on the initial conditions and a fixed number of MC particles ($\mathrm{NPC_{init}}$) are created for every cell as described in the previous section. As the simulation proceeds, the FV solver is advanced first and the cell-centered values of all the hydrodynamic variables are updated to the next time step $(n+1)$. Next the Monte Carlo module is called and the particles are moved to their new locations based on the numerical solution of the stochastic differential equations of eqs. (3.9). The updated $(n+1)$ values of the velocity, pressure, molecular and turbulent viscosity fields, as needed by the coefficients of eqs. (3.9), are interpolated to the particle location through eq. (3.10). Whenever a particle hits a boundary face, the appropriate boundary condition is applied. All the particles that have hit a interprocessor boundary face are placed in arrays and exchanged among the processors, where they complete their move. The next step consists of updating the particle composition because of the effects of molecular and turbulent mixing and of the chemical source term. Finally, the updated filtered chemical source term $\widetilde{\omega}_s$ is calculated from the particle composition and it is passed back to the FV solver.

In all the problems we investigated we always used an explicit time integration scheme

[3]Remember that an estimation of the total density, although very noisy, can be obtained from the particle field through eq. (3.17).

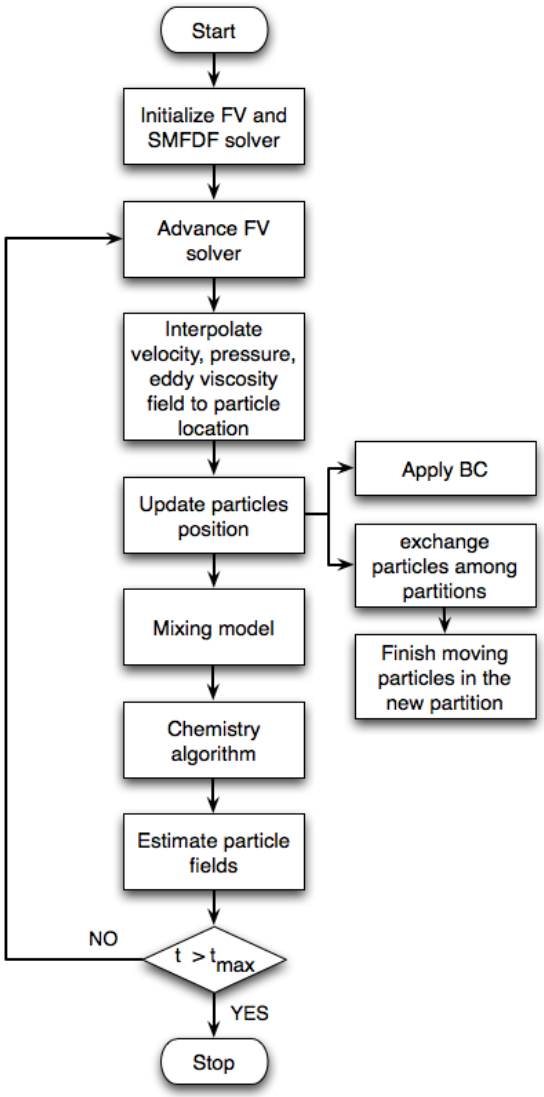

Figure 3.5: Flow chart for a hybrid FV/FMDF simulation.

for advancing the FV solution. All the FMDF routines are also integrated explicitly in time although the evaluation of source terms, eq. (3.16), could be done in an implicit manner to make it more robust in cases where stiff chemistry terms are involved.

Chapter 4

Validation

In this chapter we present the results of some two and three-dimensional temporally developing mixing layer simulations that we use to validate the FMDF solver. As discussed in the previous chapter, sec. 3.3, there is a set of variables that are independently calculated both by the finite volume (FV) and the FMDF solver and this redundancy can be exploited to check that the FMDF results are consistent with the FV ones. These redundant variables are the species mass fractions, the temperature, the total mass density and the SGS variance.

All the results we show in this chapter are for non-reacting flows, so that the additional complexities of treating stiff source terms are removed and we can focus on the performance of the advection and the mixing parts. Note that for non-reacting cases there is no feedback loop from the FMDF code to the FV one and the latter is completely unaffected by the FMDF step.
The main objectives of this chapter are,

1. To demonstrate the consistency of the FMDF/Monte Carlo methodology.
2. To investigate the sensitivity of the FMDF solution on some numerical parameters.
3. To test the performance of FMDF for variable-density and compressible flows.

In order to achieve these goals we simulated two and three-dimensional temporally developing mixing layers. These types of flow are very convenient to use for validation

because they are computationally cheap but still possess all the main features of fully developed turbulent flows.

In the next section we describe in more detail the set up of these flows and then present some consistency results using "nominal" numerical parameters. Next, we investigate the effect on the same solution of varying the most important numerical parameters in the FMDF solver, such as the initial number of particles per cell (NPC) and the size of the ensemble domain (Δ_E). The effect of the turbulence model, the grid size and the Reynolds number are also investigated.

Finally, in the last two sections, we assess the performance of the FMDF solver for variable-density flows by initializing the flowfield with a non uniform density distribution and by conducting two-dimensional simulations at a high subsonic Mach number, where compressible effects become relevant and shock waves are formed.

4.1 Two and three-dimensional temporal developing mixing layers

The temporally developing mixing layer consists of two co-flowing streams traveling in opposite directions with the same speed. This flows have been extensively studied by many researcher groups (see for instance, Jou and Riley (1989), Givi (1989) and Vreman (1995)).

The streamwise, cross-stream and, if present, spanwise directions are denoted by x and y and z, respectively. The velocity components in these directions are u, v and w. We simulated both two-dimensional and three-dimensional cases.

For the three-dimensional mixing layer, we follow the setup suggested by Vreman et al. (1994). The domain is a cubic box with $0 \leq x \leq L$, $-L/2 \leq y \leq L/2$, $0 \leq z \leq L$, where the length in the streamwise direction is large enough to allow for the roll-up of two large vortices and one subsequent pairing of these vortices. Periodic boundary conditions are assigned in the streamwise (x) and spanwise (z) directions, while along y a symmetric, no-slip condition is imposed. The initial velocity profile is initialized with a hyperbolic function with $\widetilde{u} = 1$ on the top stream and $\widetilde{u} = -1$ on the bottom one. The formation of turbulent structures is expedited by adding eigenfunctions-based perturbations to the flow, as suggested by Vreman et al. (1994). The flow variables

are normalized with respect to the half initial vorticity thickness, $L_r = [\delta_v(t = 0)/2$; $\delta_v = \Delta U/|\partial\widetilde{u}/\partial y|_{max}$, where ΔU is the velocity difference across the layer. The reference velocity and reference temperature are $U_r = \Delta U/2$ and $T_r = 1$, respectively. The Reynolds number based on the reference velocity and length scale is defined as

$$Re = \frac{U_r L_r}{\nu_r}. \tag{4.1}$$

For the three-dimensional simulations, the convective Mach number,

$$M_c = \frac{u_1 - u_2}{c_1 + c_2}, \tag{4.2}$$

is held fixed at $M_c = 0.2$. In eq. (4.2) the subscript 1 and 2 refers to the upper and lower stream, respectively, and c is the speed of sound.
We follow the evolution of a passive scalar A, which is also initialized with a hyperbolic tangent profile with $\widetilde{c}_A = 1$ on the upper one and $\widetilde{c}_A = 0$ on the bottom one.

For the two-dimensional simulations, we simulate the case proposed by Yee et al. (2000) and Sjögreen and Yee (2004) at a convective Mach number of $M_c = 0.8$. At this conditions shock waves (shocklets) are formed around the vortices and the challenge is to compute the vortex evolution accurately while avoiding oscillations around the shock. Figure 4.1 shows a schematic of the physical problem. The velocity is initialized with a hyperbolic tangent profile and the temperature is determined from an assumption of constant stagnation enthalpy. The Reynolds number defined by the velocity jump, vorticity thickness, and kinematic viscosity at the freestream temperature is set equal to 1000. Disturbances are added to the velocity components in the form of simple waves. For the normal component of velocity we have the perturbation

$$v' = \sum_{k=1}^{2} a_k \cos(2\pi k x/L_x + \phi_k) \exp(-y^2/b) \tag{4.3}$$

where $L_x = 30$ is the box length in the x-direction and $b = 10$ is the y-modulation. The u-velocity perturbations are found by assuming that the total perturbation is divergence free and $a_1 = 0.01$, $\phi_1 = -\pi/2$, $a_2 = 0.05$ and $\phi_1 = -\pi/2$. The domain is $[0, 30] \times [-50, 50]$ and a the grid is uniform in the x-direction, while a hyperbolic sine stretching is used in the y-direction.

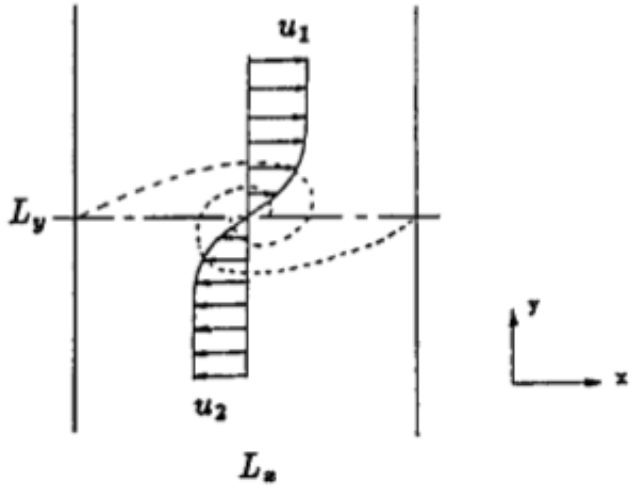

Figure 4.1: Schematic showing the vortex pairing in the two-dimensional mixing layer. This image is taken from Yee et al. (2000).

4.1.1 Numerical specifications

In all simulations equally-spaced hexahedral elements are employed ($\Delta x = \Delta y = \Delta z = \Delta$). For the three-dimensional mixing layer simulations we use cubic grids composed of $32 \times 32 \times 32$ and $64 \times 64 \times 64$ elements. The "nominal" Reynolds number, as defined by eq. (4.1), is 100. In sec. 4.3 we show the effect on the results of varying this quantity. The LES filter function is a top-hat with a characteristic filter length Δ_G,

$$G(\mathbf{x'} - \mathbf{x}) = \prod_{i=1}^{3} \hat{G}(x'_i - x_i) \tag{4.4}$$

$$\hat{G}(x'_i - x_i) = \begin{cases} \frac{1}{\Delta_G} & \text{if } |x'_i - x_i| \leq \frac{\Delta_G}{2} \\ 0 & \text{if } |x'_i - x_i| > \frac{\Delta_G}{2} \end{cases} \tag{4.5}$$

where the filter width is taken as the cubic root of the volume of the cell, $\Delta_G = \sqrt[3]{\mathcal{V}_i}$, and the secondary filter for the MKEV turbulent model (Δ') is taken so that $\Delta'/\Delta_L = 5$.

No attempt is made to investigate the sensitivity of the results on the choice of the filter function or filter width (Aldama (1990)).
The numerical input parameters for the MC solver are the initial number of particles per cell, which is set at $\mathrm{NPC}_{\mathrm{init}} = 60$ and the ensemble domain size, which is the full element ($\Delta_E = \Delta$). These are the nominal conditions. The mixing model constant is held fixed at $C_\Omega = 4$ because this value was shown by Jaberi et al. (1999) to give satisfactory results for the mixing layer. For these simulations we employ the MKEV turbulence model with a constant of $C_k = 0.020$. The turbulent Schmidt and the turbulent Prandtl numbers are held fixed at $\mathrm{Sc_T} = \mathrm{Pr_T} = 0.7$ so that $\mathrm{Le_T} = 1$.
The three-dimensional mixing layer is simulated until $t = 80$ with a timestep of $\Delta t = 0.04$, while the two-dimensional case is run until $t = 160$.

4.2 Consistency of the FMDF/MC method

We demonstrate the consistency of the FMDF/Monte Carlo procedure by comparing the first two moments (mean and SGS variance) calculated by taking an ensemble average of the particles (denoted FMDF-MC) with the same quantities obtained by solving the transport equations, eqs. (2.68) and (2.69), with the conventional finite volume solver.

We analyze the results both instantaneously and statistically. In the first case we show snap-shots and scatter plots of the relevant variables, while, in the latter, we consider Reynolds averaged statistics. Reynolds averaged variables, denoted by the $\langle\cdot\rangle$ bracket, are constructed by averaging over the statistically homogeneous directions (stream- and spanwise for these types of flows). All the results presented in this section are for the low Mach number three-dimensional mixing layer on a 32^3 equally spaced grid with $\mathrm{Re} = 50$, $\mathrm{NPC}_{\mathrm{init}} = 120$ and a cubic ensemble domain with $\Delta_E = \Delta$, unless noted. We didn't use any turbulence model for these simulations ($\mu_T = 0$).

In fig. 4.2 we present a comparison of the 3D scalar fields obtained from the FV and FMDF-MC simulations. We can see how the two results appear to be in very good agreement with each other. These plots, together with the iso-surface vorticity magnitude plot of fig. 4.3, show the high degree of mixing and three dimensional structures that are present in this flowfield, making it a good test case to assess the performance of the FMDF methodology.

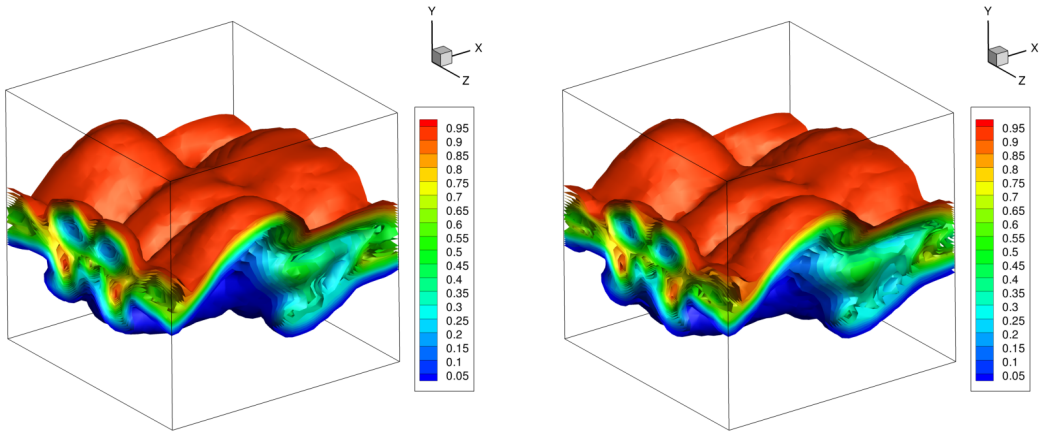

(a) (b)

Figure 4.2: Three-dimensional contour plots of the instantaneous mass fraction of the conserved scalar obtained by (a) FMDF solver and (b) finite volume solver.

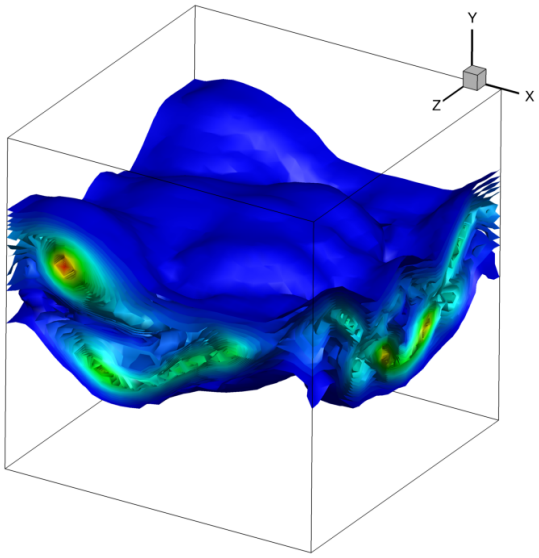

Figure 4.3: Iso-surfaces of vorticity magnitude.

The instantaneous contour plots of the filtered scalar mass fraction of fig. (4.4) provide a further visual demonstration of the consistency of the FMDF-MC procedure, as the solutions appear almost identical.

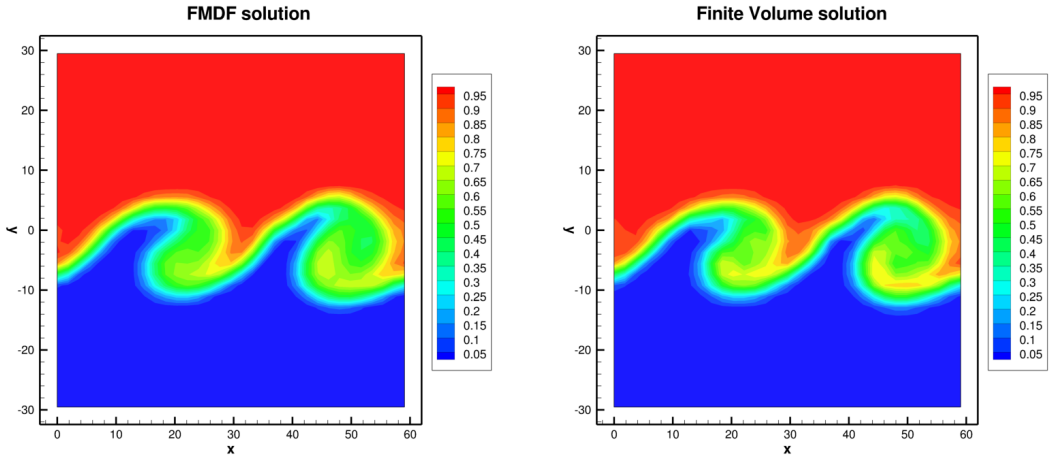

(a) (b)

Figure 4.4: Instantaneous filtered mass fraction of the conserved scalar at a slice at z=44 and t=60. (a) FMDF, (b) finite volume.

The scatter plots of fig. (4.5) demonstrate in a more quantitative manner the agreement between the two solutions for the filtered scalar $\widetilde{c}_A$. In this type of chart we plot on a xy graph the mass fractions that are obtained by both methods at each point. In fig. (4.5) we show the solution at two different times, $t = 60$ and $t = 80$. The correlation coefficient for both snapshots is greater than 0.998. The Reynolds averaged results for first moment of the filtered scalar of fig. (4.6) also confirm the excellent agreement seen in the instantaneous data.

Another quantity of interest is the resolved (or LES) variance, defined as

$$R(a,b) = (\widetilde{a} - \langle \widetilde{a} \rangle) \left(\widetilde{b} - \left\langle \widetilde{b} \right\rangle \right), \tag{4.6}$$

where $\langle \cdot \rangle$ denotes Reynolds averaging.

Figure 4.7 shows the Reynolds average results of this quantity at $t = 60$ and $t = 80$. In this case the agreement between the two methodologies is not as good as it is for the filtered mass fraction. The discrepancy is much more apparent for the second moment, the SGS variance, which is defined as $\sigma_A^2 = \widetilde{A^2} - \widetilde{A}^2$. Figure 4.8 shows that the SGS variance obtained by FMDF over predicts the FV solutions by over 300%, both at $t = 60$ and $t = 80$. The discrepancies we found in the LES and, especially, in the SGS

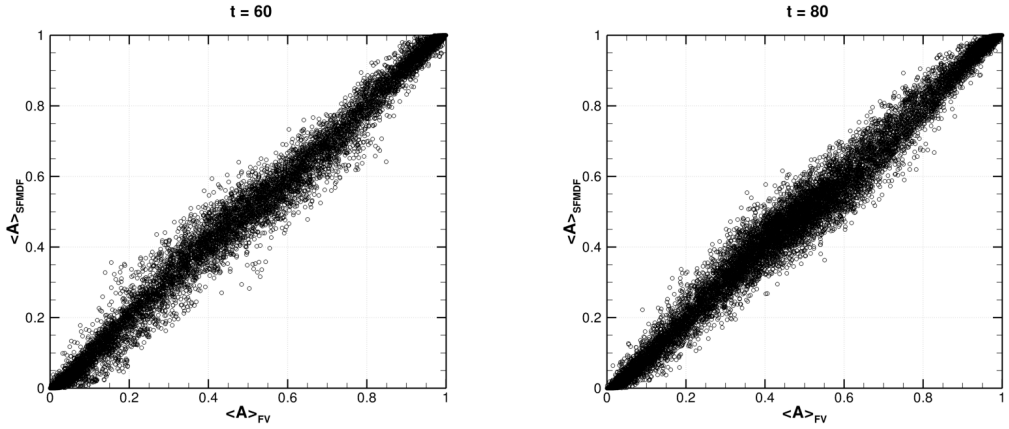

(a) (b)

Figure 4.5: Scatter plots of the filtered mass fraction of the conserved scalar calculated by FMDF and FV at (a) t=60 and (b) t=80.

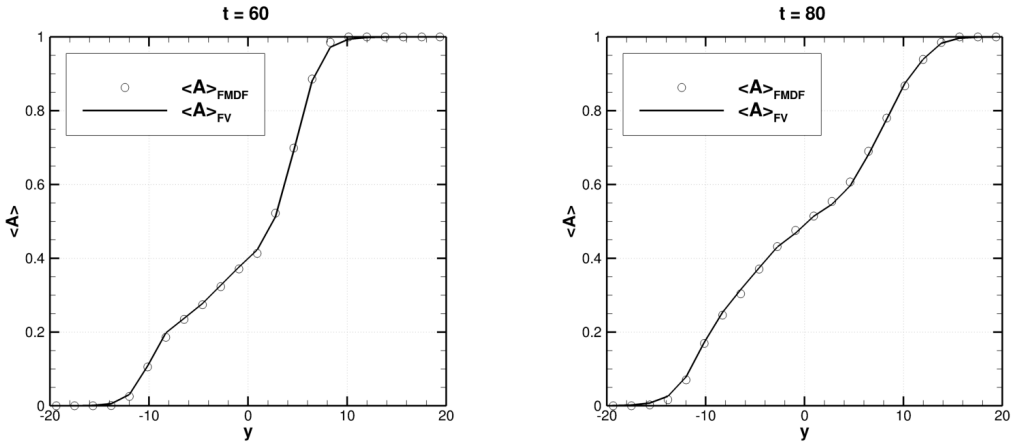

(a) (b)

Figure 4.6: Cross-stream variation of the Reynolds averaged scalar mass fraction at $t = 60$ and $t = 80$.

variance are not entirely surprising as higher moments are more sensitive to statistical and diffusion errors than lower ones. These findings motivate the numerical sensitivity study that we present in the next section.

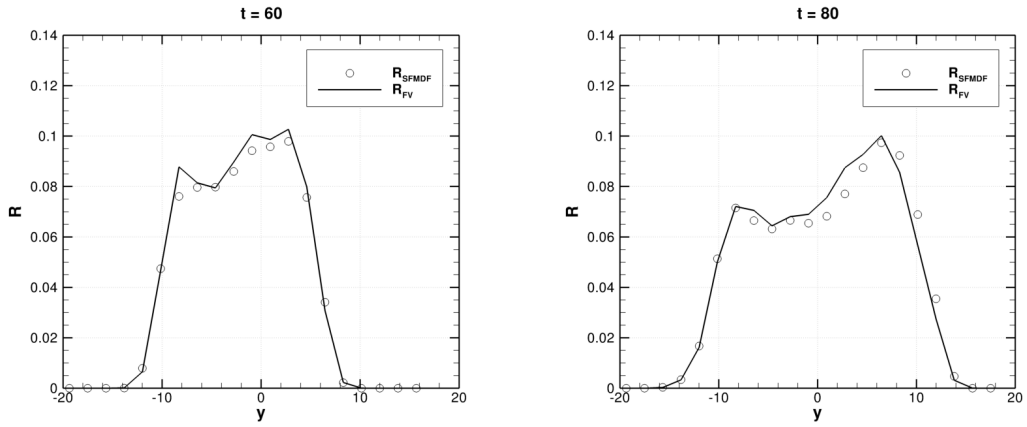

(a) (b)

Figure 4.7: Cross-stream variation of the Reynolds averaged resolved variance $\langle R \rangle$ at $t = 60$ and $t = 80$.

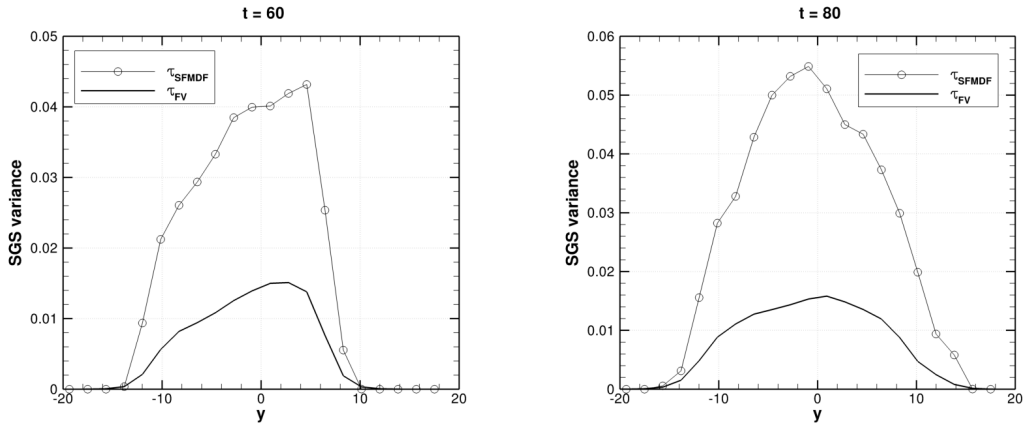

(a) (b)

Figure 4.8: Cross-stream variation of the Reynolds averaged SGS variance $\langle \tau \rangle$ at $t = 60$ and $t = 80$.

4.3 Sensitivity of the FMDF solution on numerical parameters

In this section we investigate the sensitivity of the FMDF results to different numerical parameters. We focus especially on the SGS variance because, as previously shown, it is the quantity that has the worst agreement with the FV solution. Again, all the results of this section are for the three-dimensional mixing layer and are obtained using the MKEV turbulence model. The parameters we examined are

1. Grid size.
2. Reynolds number.
3. Initial number of particles per cell (NPC).
4. Size of the ensemble domain (Δ_E).

The first step is to assess the effect of grid resolution. Figure 4.9 and 4.10 show Reynolds averaged results for the mean scalar mass fraction and SGS variance for the 32^3 and the 64^3 grids, respectively. While the scalar mean changes very little, grid resolution has a far greater impact on the higher moments. As the grid is refined and the sub grid scale content is reduced, both the FMDF and the FV results start to converge.
Another way to investigate the effect of the SGS influence on the solution is to hold the grid resolution fixed and vary the Reynolds number. As the Reynolds number is increased, as shown in fig. 4.11 and 4.12, the absolute value of the SGS variance also increases, as expected, but so does the difference between the FMDF-MC and the FV solutions. At low Reynolds numbers the two curves lie very close but, as we reach $Re = 50$ and $Re = 100$, the relative difference between the two solutions jumps to over 300% and 400%, respectively. One possible explanation may lie in the fact that, as the Reynolds is increased, so does the sub-grid scale content that is being filtered and that needs to be modeled. The last two sets of numerical parameters that can have an impact on the solution (initial number of particles per cell and ensemble domain size) are characteristic of the Monte Carlo solver only. The Reynolds averaged results of fig. 4.13 clearly demonstrate that the initial number of particles per cell does not have a major impact on the FMDF solution. We found that this always holds true provided

that NPC is above about 30.

Those results are in contrast with the size of the ensemble domain size, which does have some effects on the solution. As expected, a smaller Δ_E corresponds to a more accurate FMDF solution, as it is demonstrated by the resolved variance in fig. 4.14. A similar effect is seen on the SGS variance, for both the 32^3 grid, fig. 4.15(a), and the 64^3 one, fig. 4.15(b). It must be noted, however, that whenever the ensemble domain is shrunk, the number of initial particles per cell must be increased so that there are enough particles inside Δ_E to compute meaningful statistics. The computational requirement of the simulation is consequently increased.

The impact of the NPC and Δ_E on the FMDF solution we find here are in accordance to earlier results by various research groups such as Jaberi et al. (1999), Colucci et al. (1998) and Colucci (1998). Effectively fig. 4.14 and 4.15(b) demonstrates that the FMDF-MC formulation is also consistent with the FV method for the SGS variance, provided that certain constraints on the grid resolution and the ensemble domain size are satisfied.

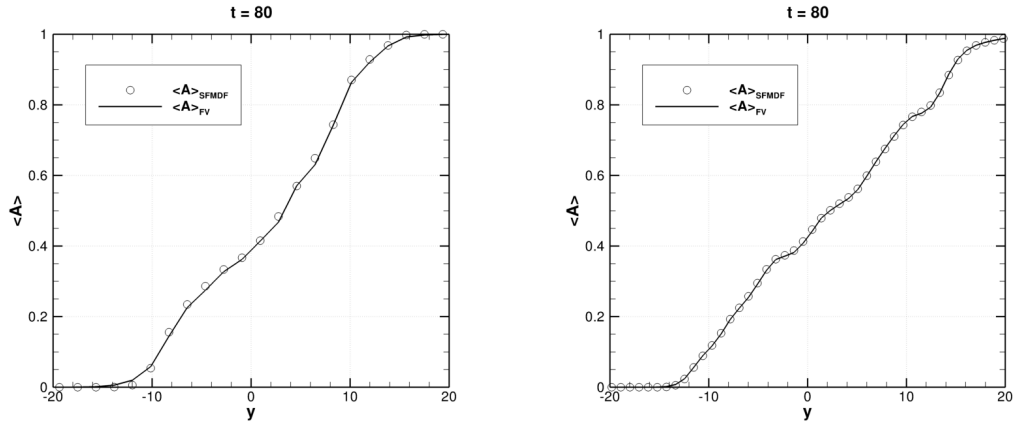

(a) (b)

Figure 4.9: Reynolds averaged scalar mass fraction. (a) 32^3 grid. (b) 64^3 grid.

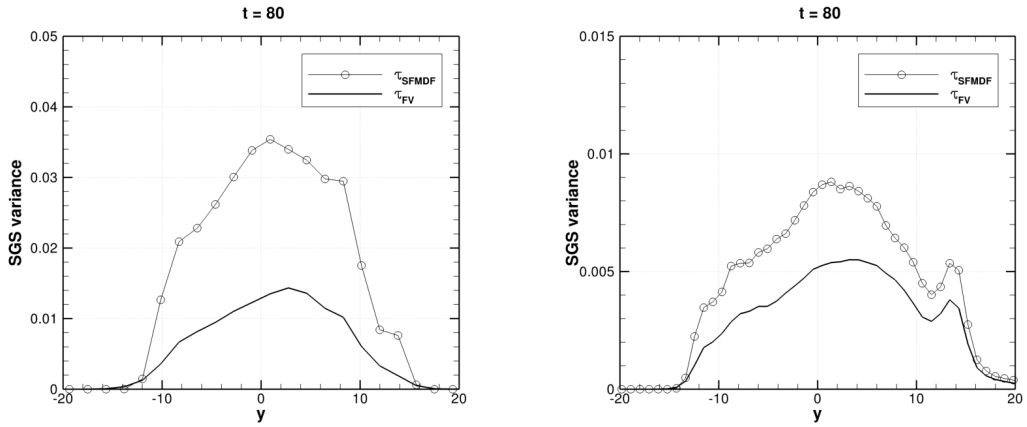

(a) (b)

Figure 4.10: Reynolds averaged SGS variance. (a) 32^3 grid. (b) 64^3 grid.

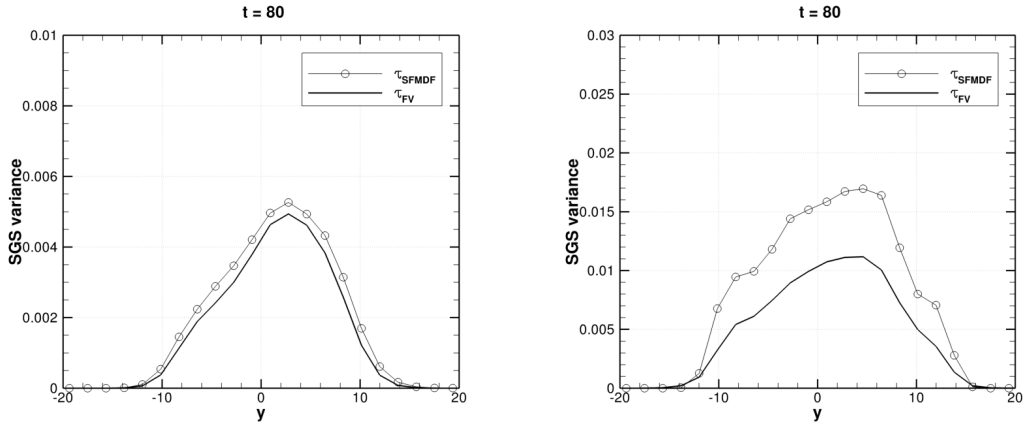

(a) (b)

Figure 4.11: Cross-stream variation of the Reynolds averaged SGS variance $\overline{\tau}$ at t=80. (a) $Re = 10$, (b) $Re = 25$

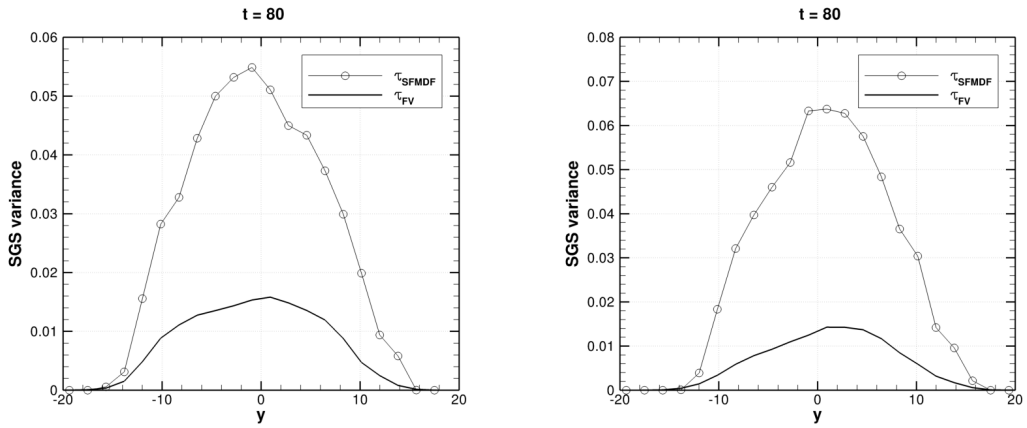

(a) (b)

Figure 4.12: Cross-stream variation of the Reynolds averaged SGS variance $\overline{\tau}$ at t=80. (a) $Re = 50$, (b) $Re = 100$

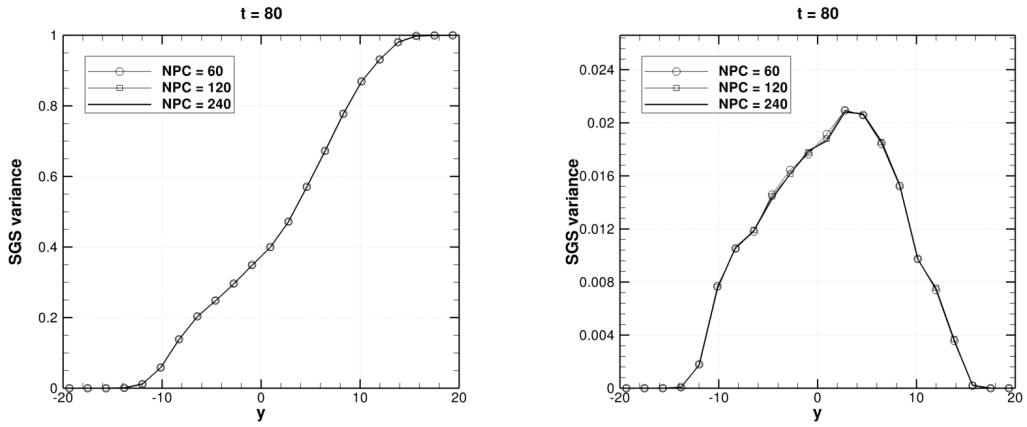

(a) (b)

Figure 4.13: Effect of the initial number of particles (NPC) at $t = 80$. (a) Reynolds averaged scalar mass fraction, (b) Reynolds averaged SGS variance.

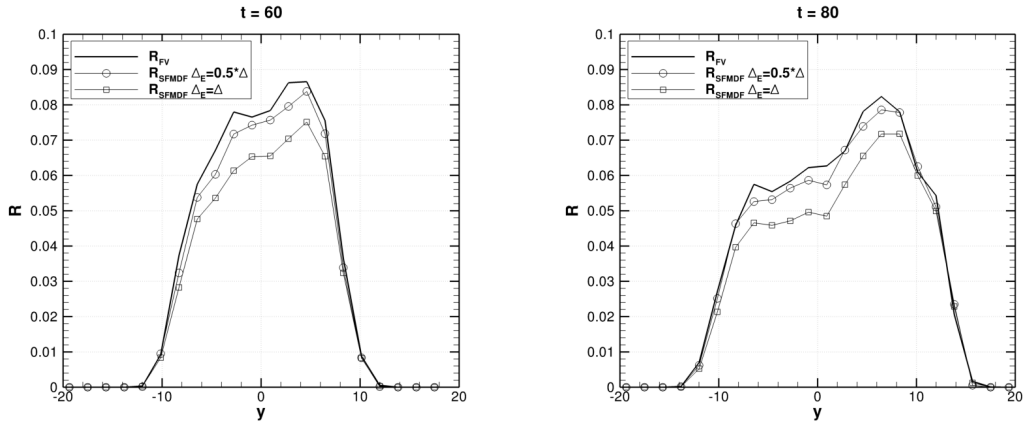

(a) (b)

Figure 4.14: Effect of the width of the ensemble domain on the the Reynolds averaged resolved variance. (a) $t = 60$, (b) $t = 80$.

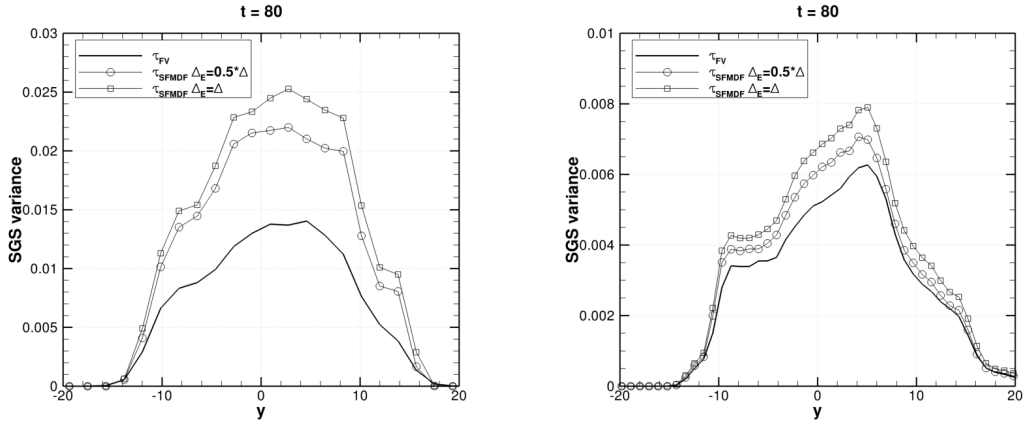

(a) (b)

Figure 4.15: Effect of the ensemble domain size on the the Reynolds averaged SGS variance at $t = 80$. (a) 32^3 grid, (b) 64^3 grid.

4.4 Validation of FMDF in variable-density flows

In this section we analyze the performance of the FMDF-MC method on variable-density flows. We achieve this (i) by studying low speed flows with initial non-uniform density, and (ii) by considering a high subsonic Mach number flow, where the effects of compressibility are important.
For (i) we employ the same three-dimensional mixing layer described in the previous sections. The major difference is that now the two streams are initialized with different densities, while the pressure is kept constant. In order to investigate (ii) we utilize the two-dimensional temporal mixing layer case which we described at the beginning of the chapter. The convective Mach number of the layer is $M_c = 0.8$, so that, at this speed, part of the flow becomes supersonic and shock waves are formed around the primary vortices. This type of flow field represents a good case to test the performance of the FMDF/Monte Carlo methodology in the presence of discontinuities.

4.4.1 Low-speed 3D mixing layer with non-uniform initial density

Flow fields characterized by non-uniform densities are very important from a practical standpoint. In fact, even in the case of low-speed, incompressible flows, the effects of exo- or endothermic chemical reactions can significantly change the local temperature - and therefore density - of the flow. We show some examples of these effects in chapter 6. In order to validate the FMDF solver for low-speed, variable density cases without using a chemical source term, we initialize the three-dimensional mixing layer with different densities between the upper and the lower streams. In particular, all of the simulations shown here are carried out with the density ratio between the upper stream and the lower one, $S = \rho_1/\rho_2$, kept fixed at $S = 2$. The initial pressure across the layer is kept constant, so that $T_{up}/T_{bot} = 1/S$, where T_{up} and T_{bot} are the normalized temperatures of the two layers. This set up is similar to what was employed by Sheikhi et al. (2007).

Figure 4.16 shows the scatter plots of the temperature for a simulation on a 32^3 grid with $Re = 50$ and using the MKEV turbulence model. There is good agreement between the temperature calculated by the finite volume solver and by the FMDF-MC one. This agreement is confirmed by the Reynolds averaged results which are depicted

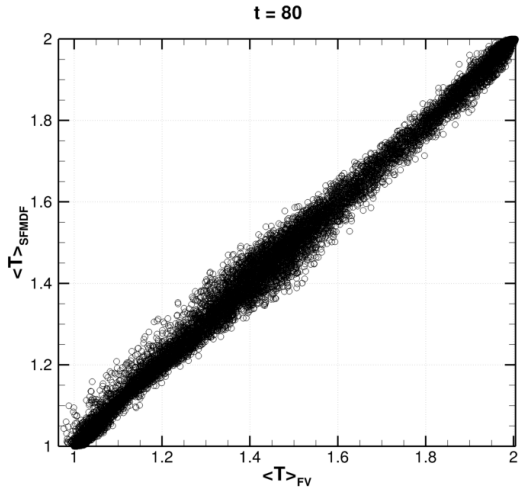

Figure 4.16: Scatter plots of the filtered temperature calculated by FMDF and FV at t=80

in fig. 4.17.

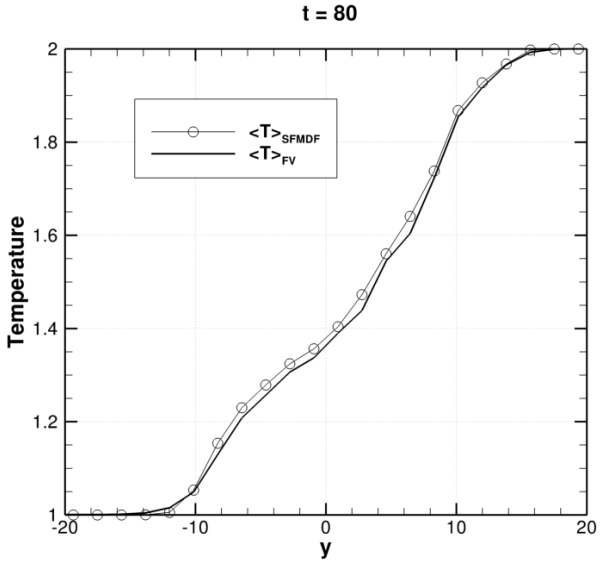

Figure 4.17: Cross-stream variation of the Reynolds averaged temperature at t=80.

There are two manners to calculate the local density in the FMDF-MC framework:

1. *Using particle weights.* The sum of the weights of the particles belonging in an ensemble domain is directly linked to the local density through eq. (3.17):

$$\overline{\rho} \approx \frac{\Delta m}{\Delta V_E} \sum_{p \in \Delta_E} w^{(p)}. \tag{4.7}$$

   This is referred to as the particle density and, as noted earlier, it is significantly affected by statistical noise.

2. *Using the enthalpy equation and the equation of state.*

$$\overline{\rho} \approx \left(\frac{\sum_{p \in \Delta_E} w^{(p)} (RT^{(p)}/\overline{p})}{\sum_{p \in \Delta_E} w^{(p)}} \right)^{-1} \tag{4.8}$$

   This is referred to as the FMDF density and, as the pressure is solely obtained by the FV solver, it is related to the FMDF temperature.

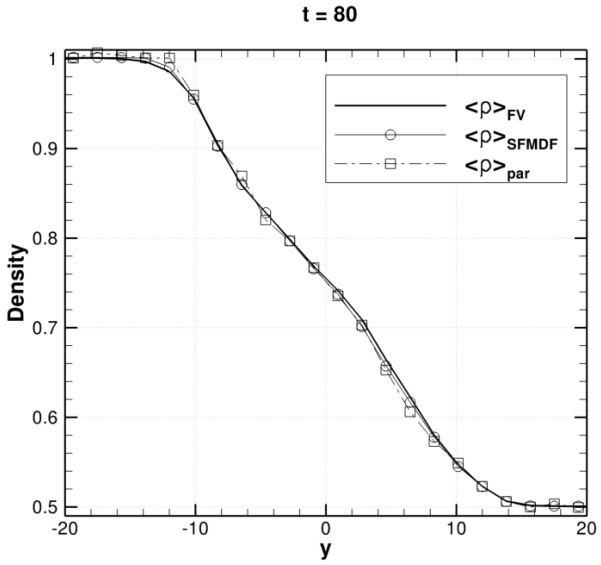

Figure 4.18: Cross-stream variation of the Reynolds averaged density obtained at t=80. Solid line: finite volume results. Circles: eq. (4.8). Squares: eq. (4.7).

Figure 4.18 shows the comparison of the Reynolds averaged results for the FV density,

the FMDF density and the particle density. The latter quantity shows some noise even in these averaged results, but the overall comparison is good.

4.4.2 2D compressible mixing layer

The local mass density can change not only because of the effect of heat releasing (or absorbing) chemical reactions but also due to the effects of compressibility. To investigate the performance of the FMDF methodology in this latter case, we use the two-dimensional, temporal developing mixing layer case which we described at the beginning of the chapter. The initial convective Mach number ($M_c = 0.8$) is large enough that typical compressibility effects are present in the field. These are clearly visible in the two instantaneous snapshots of the filtered temperature of fig. 4.19 and 4.20.

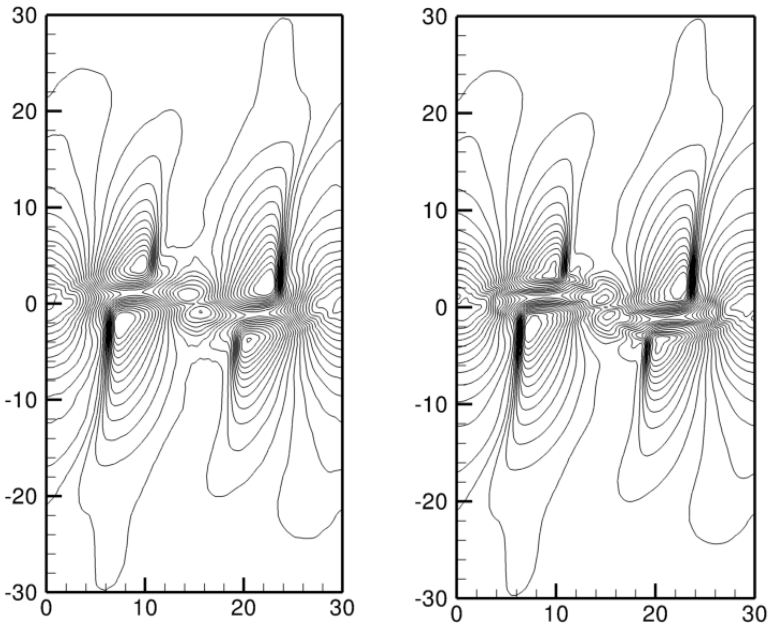

Figure 4.19: Contour plots of the normalized filtered temperature at $t = 80$ with 26 contour levels from 0.88 to 1.13. (a) FMDF, (b) FV.

These results demonstrate the consistency of FMDF also in the presence of discontinuities and are in good qualitative agreement with the reference solution obtained by Yee et al. (2000). A more quantitative comparison is obtained by looking at the scatter

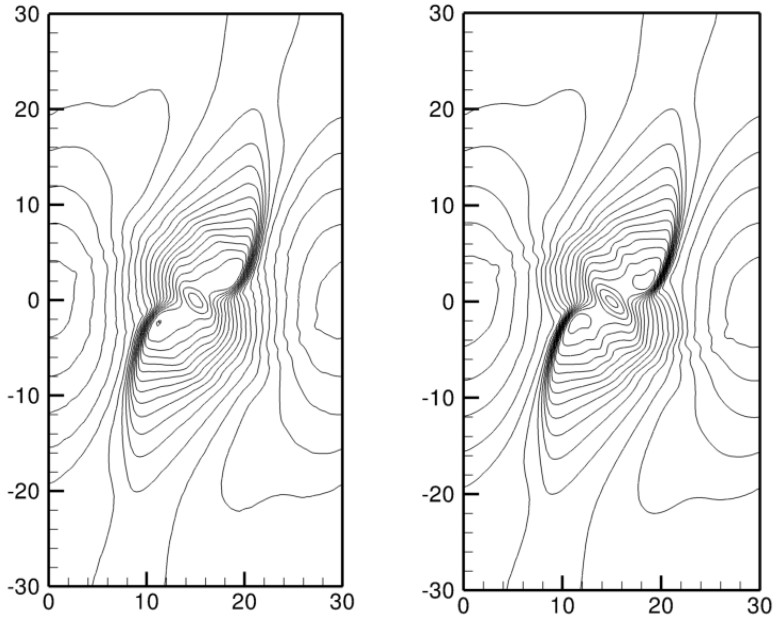

(a) (b)

Figure 4.20: Contour plots of the normalized filtered temperature at $t = 120$ with 20 contour levels from 0.72 to 1.1. (a) FMDF, (b) FV.

plots of fig. 4.21. For both times most of the points lie very close to the diagonal of the chart, indicating an excellent agreement between the two solutions.

The consistency of the method can also be checked by comparing the density contour plots of fig. 4.22. Although, as expected, the particle density field is characterized by a large amount of noise, the discontinuities in the density field are correctly captured and don't seem to create instabilities in the FMDF solution.

Finally, in fig. 4.23 and 4.24, we present two snapshots of the SGS variance, which is the most sensitive among the variables for which consistency can be checked. Also for this quantity the FMDF results, although slightly noisier, compare fairly well with the FV predictions.

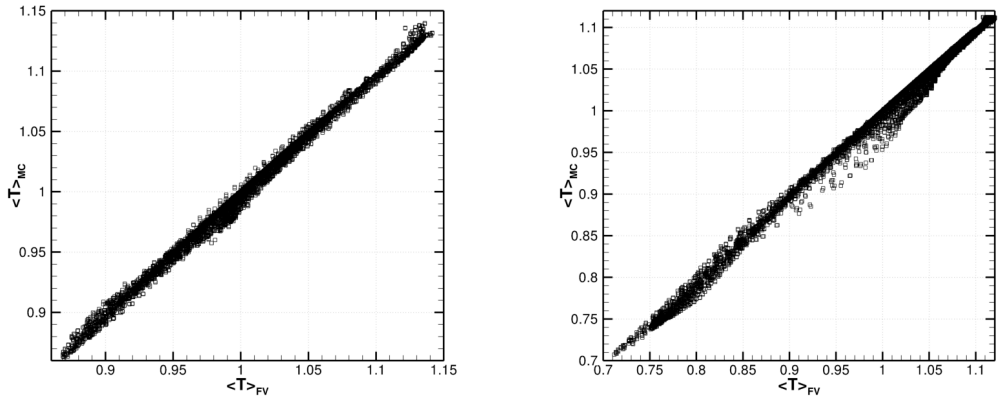

(a) (b)

Figure 4.21: Scatter plots of the FMDF and FV normalized filtered temperature. (a) $t = 80$, (b) $t = 120$.

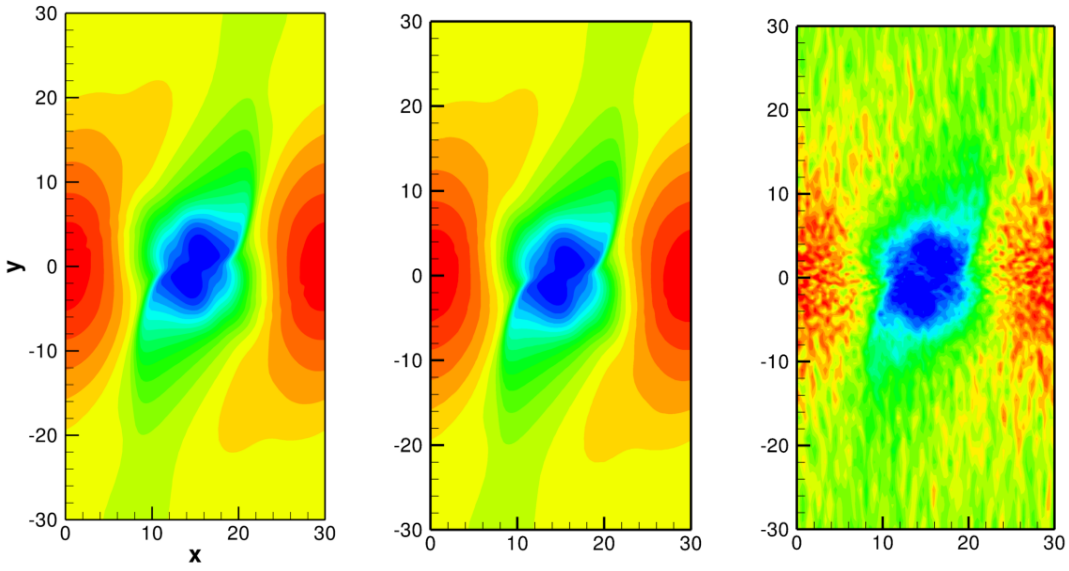

(a) (b) (c)

Figure 4.22: Contour of the filtered density at $t = 120$ with 19 levels from 0.35 to 1.25. (a) FV density, (b) FMDF density, eq. (4.8), (c) Particle density, eq. (4.7).

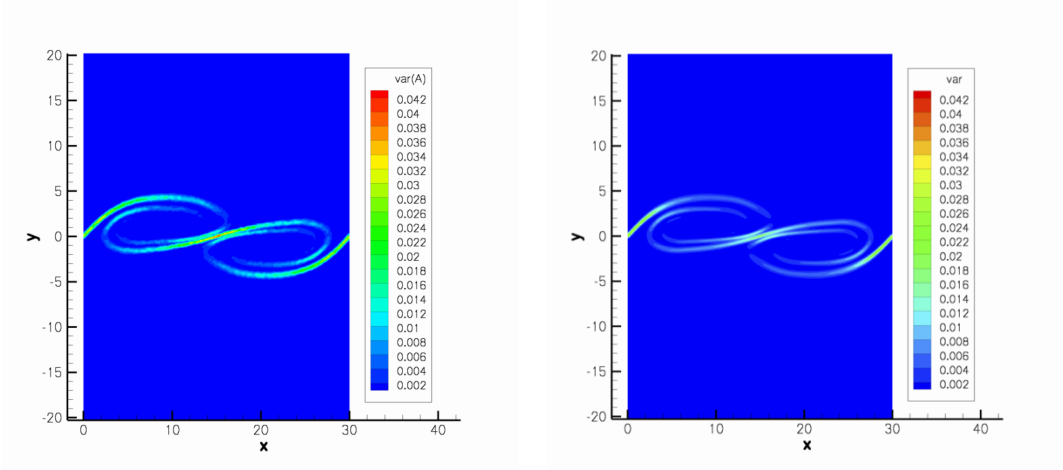

(a) (b)

Figure 4.23: Instantaneous contour plot of SGS variance at $t = 80$ for the high-speed mixing layer. (a) FMDF. (b) FV.

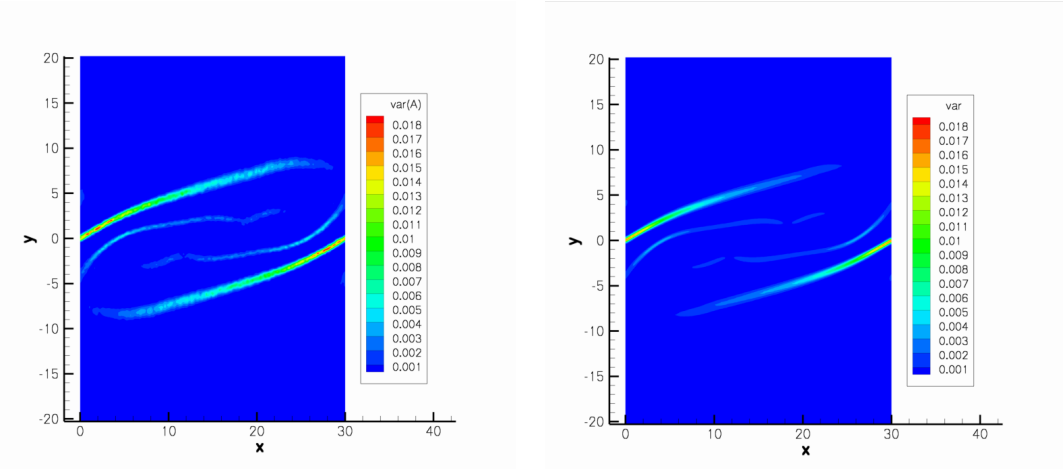

(a) (b)

Figure 4.24: Instantaneous contour plot of SGS variance at $t = 160$ for the high-speed mixing layer. (a) FMDF. (b) FV.

4.5 Computational requirements

In the development of the FMDF solver we placed more emphasis on robustness rather than on optimization. Nevertheless, our results on the CPU times that is required to carry out a simulation are encouraging. All tests were performed on the three-dimensional temporal mixing layer with two different grid sizes and three different initial numbers of particles per cell (NPC). The results are shown as the percentage increase in CPU time of the hybrid LES-MC simulations over the LES simulation alone.

Grid	NPC_{init}	Total number of particles	Increase in CPU time (%)
$32 \times 32 \times 32$	60	1.9 million	26.5
$32 \times 32 \times 32$	120	3.9 million	73.7
$32 \times 32 \times 32$	240	7.8 million	266
$64 \times 64 \times 64$	120	31.4 million	317.4
$64 \times 64 \times 64$	480	125.8 million	1083

Table 4.1: Percentage increase in CPU time of hybrid FMDF/FV simulations as compared to standard FV ones for different gird sizes and initial number of particles per cell (NPC_{init}).

As table 4.1 shows, when 60 particles per cell are used, the computational overhead of the Monte Carlo solver is less than 30 %. It must be noted that most FMDF simulations in the literature use around 40 particles per cell. As expected, CPU times drastically increase when NPC is over 120.

The simulations on the 32^3 grids were performed on 16 processors, while we utilized 64 processors for the 64^3 grid.

Chapter 5

Chemically reacting simulations

In this chapter we present the results of chemically reacting simulations with the goal of demonstrating the greater accuracy of the hybrid FMDF/FV methodology as compared to finite volume simulations in which the SGS turbulence/chemistry interactions are neglected[1].

We simulate the same two- and three-dimensional temporally developing mixing layers that we described in the previous chapter, with the addition of a simple chemical source term. The grid sizes, physical conditions and numerical parameters are the same as those employed in chapter 4 (sec. 4.1).

We first demonstrate that the FMDF solution is consistent with the FV one also in the presence of a chemical source term, provided that the latter is evaluated by the FMDF procedure and passed back to the FV solver. Next, we compare the results obtained by the hybrid FMDF/FV methodology and by the model-free LES against the solution of a direct numerical simulation (DNS) for the two-dimensional mixing layer. Both the instantaneous and Reynolds averaged results clearly show that the FMDF/FV predictions for the amount of product formed are much closer to the DNS as compared to the model-free LES for the same grid resolution. All the incompressible results presented in this chapter are taken from Ferrero et al. (2012).

[1] For the reminder of this work we will refer to a LES in which the turbulence/chemistry interactions are ignored as model-free LES. We will also interchangeably use the term LES-MC to denote the hybrid FMDF/FV methodology and the term LES-FV to refer to the model-free LES.

5.1 Chemical reaction mechanism

For the set of simulations presented in this chapter we use a simple one-step, irreversible reaction which is described by the chemical formula,

$$\mathrm{A} + \mathrm{B} \overset{\mathrm{k_f}}{\rightarrow} 2\mathrm{P}, \tag{5.1}$$

where A and B are the reactants while P is the product. The chemical source terms are given by

$$\omega_A = \omega_B = -\rho k_f c_A c_B, \tag{5.2}$$

where c_A, c_B are the mass fractions of the reactants and k_f is the pre-exponential factor. The reactant-product conversion rate is controlled by the Damköhler number, which is defined as $Da = k_f \rho_r / (U_r/L_r)$. For the mixing layers simulated here the reference quantities are $L_r = [\delta_v(t=0)]/2$, $U_r = \Delta U/2$ and $\rho_r = 1$ (see sec. 4.1). The non dimensional number that characterizes the degree of exothermicity of the reaction is the heat release parameter,

$$C_E = \frac{h_P^0}{C_P T_r}, \tag{5.3}$$

where h_P^0 and C_P are the heat of formation and the specific heat of the product, respectively, while $T_r = 1$. Note that this reaction scheme is a simplified version of the general Arrhenius form of eq. (2.21) with no dependence on temperature (i.e. $E_a = 0$ and $\eta = 0$).

5.2 Validation of the FMDF solver for chemically reacting simulations

Even in the presence of a chemical source term the FMDF solutions must be consistent with those obtained by the finite volume code provided that the source term is evaluated by taking ensemble averages of the FMDF particles and passed back to the finite volume solver (see fig. 3.4). For reacting cases, thus, assessing the consistency of the hybrid formulation with the FV also serves as a way to check that the chemical source term is calculated correctly.

In this section we show some results from the two- and three-dimensional mixing layers that demonstrates consistency. The three dimensional cases are low-speed, $M_c = 0.2$, with $C_E = 35$. We run two set of simulations characterized by very different reaction kinetics, Da = 0.01 and Da = 10.

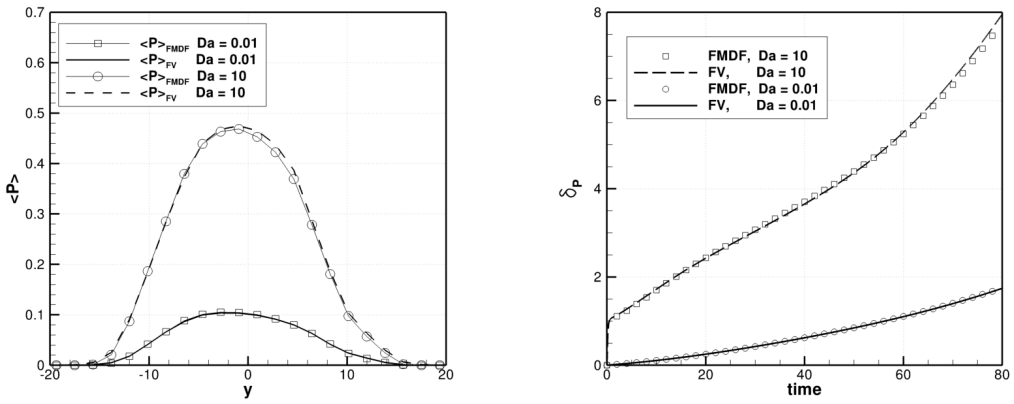

(a) (b)

Figure 5.1: Reynolds averaged product mass fraction (a) and total product formation (b) for $Da = 0.01$ and $Da = 10$. Low-speed 3D mixing layer.

In fig. 5.1(a) we plot the Reynolds averaged filtered product mass fraction for both cases. It is evident that the slower reaction mechanism (lower Da) does not have time to generate as much product as the high Da case. This is also evident from fig. 5.1(b), where we show the total product formation as a function of time. This latter quantity is a convenient manner of expressing the total amount of P that is present in the domain at a certain time and is mathematically defined as

$$\delta_P(t) = \int \langle \widetilde{c}_P \rangle (y,t) dy, \tag{5.4}$$

where the tilde stands for filtered value while the $\langle \cdot \rangle$ bracket denotes Reynolds averaging. A higher amount of product is converted from the reactants for the faster reaction scheme as compared to the slower one. In both cases the agreement between the FMDF and the FV solutions is excellent.

For the two-dimensional case we simulate a compressible case with $M_c = 0.8$, $C_E = 0.5$

and Da = 1 and in fig. 5.2 we show the results for the filtered temperature and density.

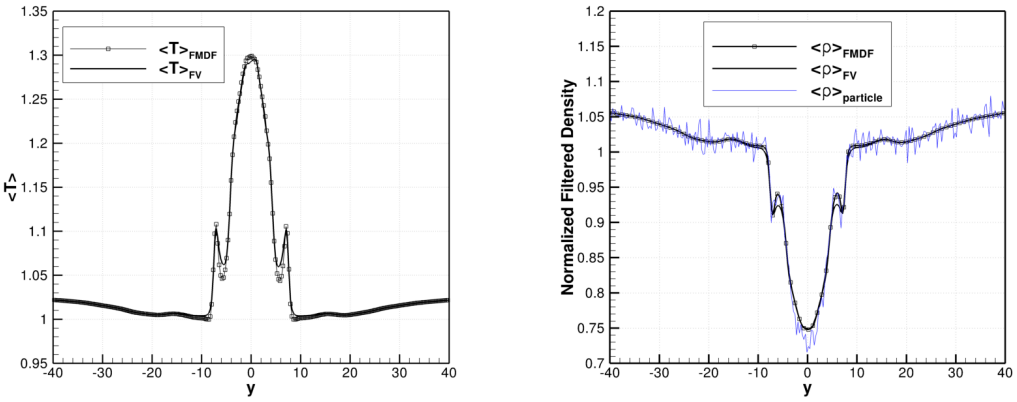

(a) (b)

Figure 5.2: Reynolds averaged plots for the normalized filtered temperature (a) and density (b) at $t = 160$. Compressible 2D mixing layer.

As already noted for the non-reacting cases, the particles density exhibits some statistical noise, as expected, but the two solutions are consistent.

5.3 Comparison with DNS results

While the previous test cases were used to validate the FMDF solver and to check its consistency, in this section we show that the FMDF methodology is able to obtain better predictions for chemically reacting flows as compared to model-free LES for the same grid. To this aim, we utilize the two-dimensional mixing layer described in sec. 4.1 and we compare the product mass fraction c_P obtained by the hybrid FMDF/FV methodology with DNS results. We show that the predictions of the hybrid scheme lie much closer to the DNS data than those obtained from a model-free LES.

We simulate both a low convective Mach number case ($M_c = 0.2$) and a compressible one ($M_c = 0.8$). In both cases we use a grid of 100×200 elements for the hybrid FMDF/FV and for the model-free LES simulations, while for the DNS we utilize 500×1000 points. All the grids are equally spaced. The Reynolds number based on the velocity difference, vorticity thickness and kinematic viscosity at the free stream velocity

is Re = 1000 (see sec. 4.1). We focus the attention on the filtered product mass fraction, $\widetilde{c}_P$ because the amount of product formation is entirely dictated by the chemical source term.

The increased accuracy of the FMDF methodology can be qualitatively appreciated by comparing the contour plots of the filtered product from the DNS, LES-MC and LES-FV of fig. 5.3 for the low-speed case ($M_c = 0.2$) and of fig. 5.4 for the compressible case ($M_c = 0.8$).

The LES-MC contour plots are relatively close to the DNS ones, although the LES were performed on a grid which is twenty-five times smaller than the one used for the DNS. On the other hand, when the SGS contribution of the chemical source terms are neglected, as in the case of LES-FV results, the product formation is over-predicted and tends to be more diffused. We can notice this effect in more quantitative terms from the Reynolds averaged profiles for $\widetilde{c}_P$ of fig. 5.3(d).

The increased accuracy of the FMDF formulation over model-free LES is not limited to the specific time we chose to present but it is evident throughout the whole simulation, as the time history of the total product formation of fig. 5.5 demonstrates. With the exception of the initial linear growth, after around $t = 30$ the flow becomes turbulent and the conventional LES consistently over-predicts the total product formation, while the FMDF profile lies much closer to to the value predicted by DNS. Again, this behavior is confirmed in both the low- and high-speed simulations.

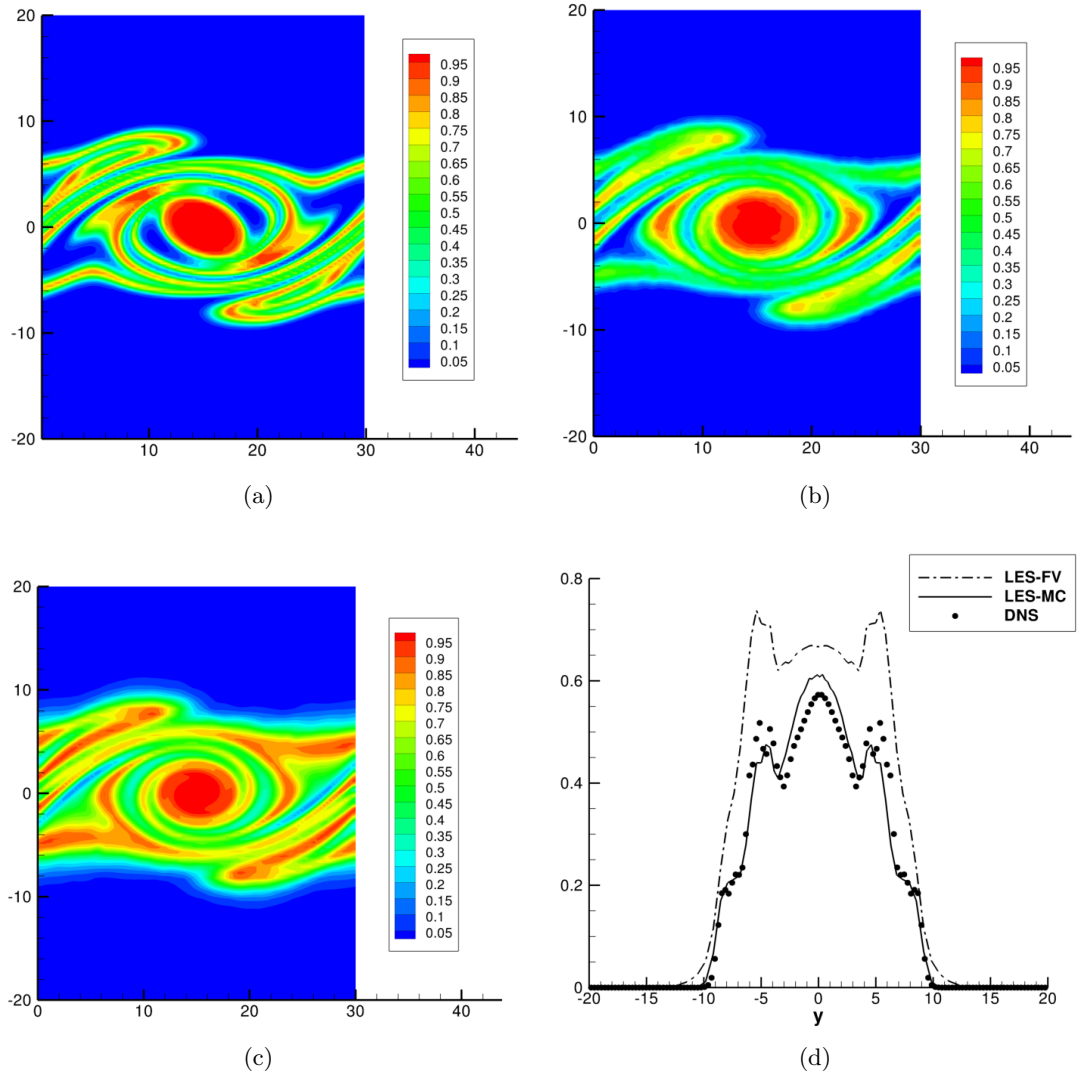

Figure 5.3: Product filtered mass fraction $\widetilde{c}_P$ at $t = 160$. (a) Filtered DNS, (b) LES-MC, (c) LES-FV and (d) Reynolds averaged along x. Low-speed case ($M_c = 0.2$).

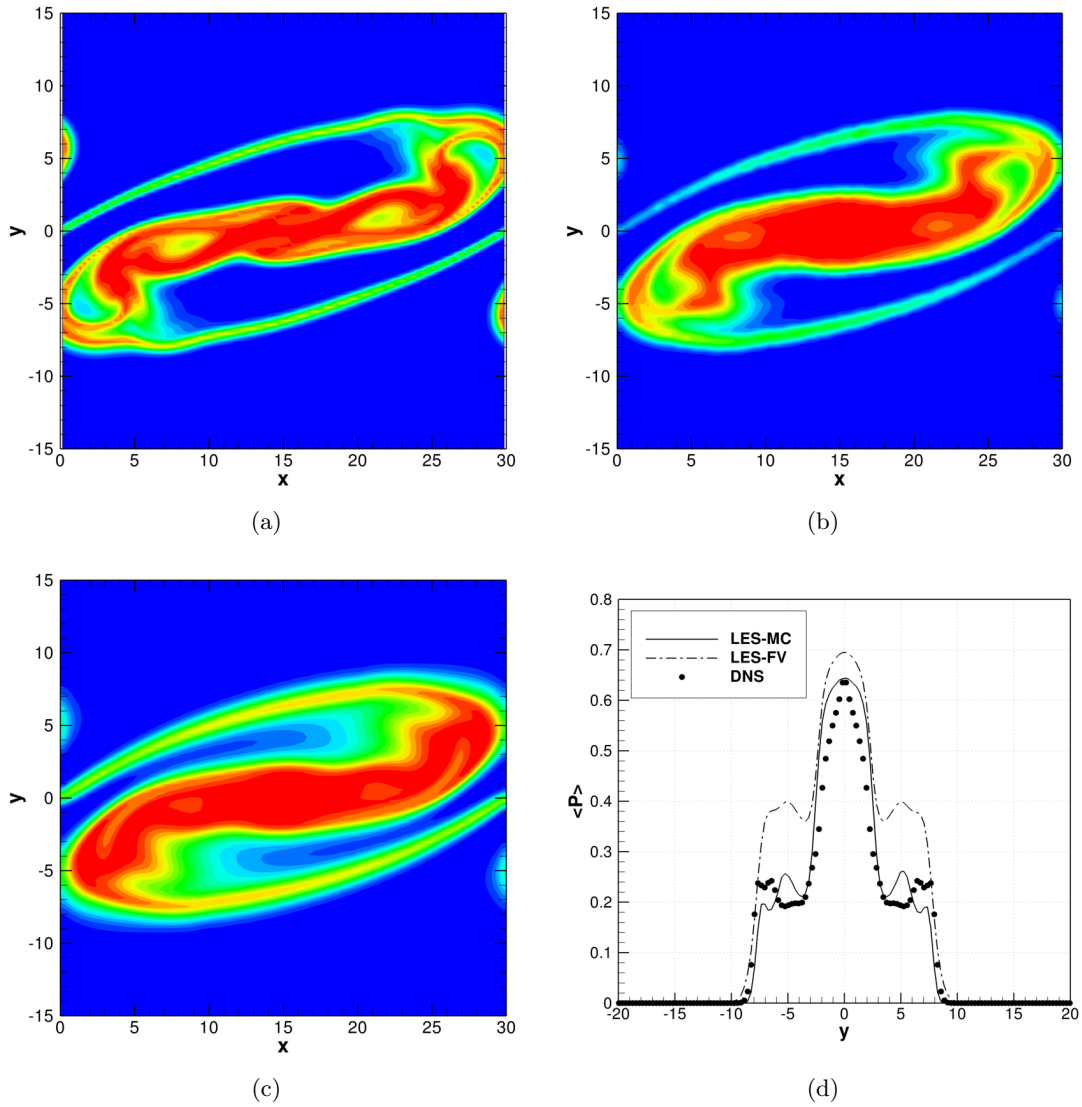

Figure 5.4: Product filtered mass fraction $\widetilde{c}_P$ at $t = 160$. (a) Filtered DNS, (b) LES-MC, (c) LES-FV and (d) Reynolds averaged along x. High-speed case ($M_c = 0.8$).

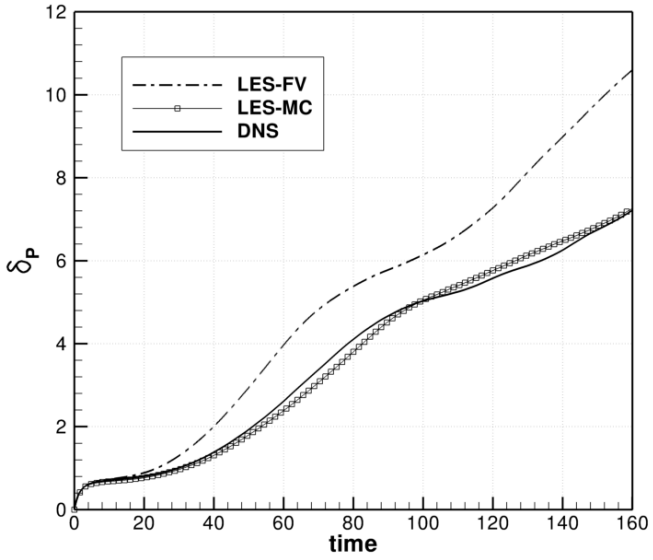

(a)

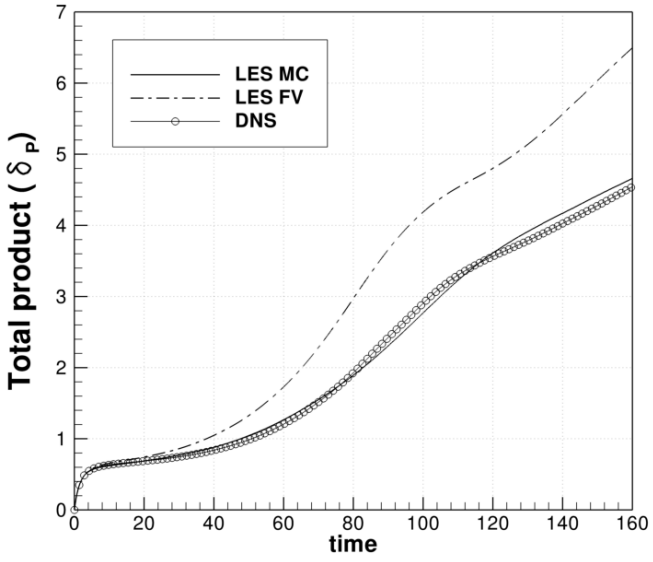

(b)

Figure 5.5: Total product formation versus time for the DNS data (solid line), LES-MC (symbols) and LES-FV (dashed-dotted line). (a) $M_c = 0.2$, (b) $M_c = 0.8$.

Chapter 6

Simulation of high-Reynolds, chemically reacting, spatially developing mixing layers

In this chapter we apply the hybrid FMDF/FV methodology, which we have been validated in previous chapters, to the simulation of high-Reynolds number, chemically reacting, spatially developing mixing layers. These flows are much more complicated, in terms of computational requirements, geometric complexity and reaction mechanism, than the temporally developing mixing layers that we presented earlier. In particular our aim is to reproduce the experimental results obtained by Slessor et al. (1998). The chemical mechanism is the reaction of hydrogen and fluorine to produce HF. This is an exothermic, kinetically-fast reaction (Da $\gg 1$) in which the heat release (and the consequent temperature rise) is a direct measure of the product formation. The upper stream has a velocity of $U_1 = 100$ m/s and is composed of a mixture of H_2 and inert gases, while the bottom stream has a lower velocity, $U_2 = 40$ m/s, and carries F_2 diluted in inert gases. Both streams have the same density. The mixing layer develops from a splitter plate and is characterized by a fairly large Reynolds number ($Re_{\delta_T} = 2 \cdot 10^5$). Although we do not explicitly model the boundary layers developing on the splitter plate, we impose laminar boundary-layer profiles at the inflow consistent with those reported in Slessor et al. (1998).

We performed both two- and three-dimensional simulations with different initial concentrations. The work we show in this chapter is an attempt to improve on the results we report in Ferrero et al. (2013) which we obtained using a model-free LES, where the chemistry/turbulence interactions were ignored.

6.1 Reaction mechanism

The chemical reaction considered is between molecular hydrogen and fluorine and can be formally written as

$$\mathrm{H_2 + F_2 \rightleftharpoons 2HF}, \qquad \Delta \mathrm{Q} = 544 \ \ \mathrm{kJ/mol}. \tag{6.1}$$

However, a more realistic reaction mechanism is composed of the hydrogen-fluorine chain reactions and nitric-oxide-fluorine dissociation:

$$\mathrm{H_2 + F} \overset{k_1}{\rightleftharpoons} \mathrm{HF + H}, \ \ \Delta Q = -133.9 \ \ \mathrm{kJ/mol}, \ \ k_1 = 2.6\times10^9\, T^{0.5} \exp\left(\frac{-307}{T}\right) \tag{6.2a}$$

$$\mathrm{F_2 + H} \overset{k_2}{\rightleftharpoons} \mathrm{HF + F}, \ \ \Delta Q = -411.3 \ \ \mathrm{kJ/mol}, \ \ k_2 = 3.0\times10^6\, T^{1.5} \exp\left(\frac{-845.5}{T}\right) \tag{6.2b}$$

$$\mathrm{NO + F_2} \overset{k_3}{\rightleftharpoons} \mathrm{NOF + F}, \ \ \Delta Q = -76.6 \ \ \mathrm{kJ/mol}, \ \ k_3 = 4.2\times10^8 \exp\left(\frac{-1150}{T}\right) \tag{6.2c}$$

Although the $\mathrm{H_2/F_2}$ reaction mechanism is very fast, it needs a catalyst to initiate the chain reactions. As pointed out by Mungal and Dimotakis (1984) it must be ensured that some F atoms are present in the system so that reactions (6.2a) and (6.2b) can proceed rapidly. For this reason a small amount of nitric oxide (NO) is introduced in the high-speed stream so that atomic fluorine is formed through reaction (6.2c). It was determined by Broadwell and Breidenthal (1982) that the overall chemical rate is linearly proportional to the concentration of NO (for small concentrations). Additional reactions that we consider are the formation of NOF and the dissociation of $\mathrm{F_2}$, $\mathrm{H_2}$ and

HF.

$$\mathrm{F + NO + M \overset{k_4}{\rightleftharpoons} NOF + M}, \quad \Delta Q = -238.5 \ \mathrm{kJ/mole}, \quad k_4 \approx 3.0\times10^{13} \tag{6.3a}$$

$$\mathrm{F + F + M \overset{k_5}{\rightleftharpoons} F_2 + M}, \quad k_5 \approx 3.2\times10^{11} \tag{6.3b}$$

$$\mathrm{H + F + M \overset{k_6}{\rightleftharpoons} HF + M}, \quad k_6 \approx 2.5\times10^{13} \tag{6.3c}$$

$$\mathrm{H + H + M \overset{k_5}{\rightleftharpoons} H_2 + M}, \quad k_7 \approx 3.0\times10^{12} \tag{6.3d}$$

The equilibrium constants k_i are given in $\mathrm{m^3\ kmol^{-1}s^{-1}}$ and have been estimated by Mungal and Frieler (1988) at 300 K. The overall chemical time, τ_{chem} that it takes for the reaction set (6.2) to complete is a very important quantity that is used to define the Damköhler number,

$$\mathrm{Da} = \frac{\tau_{\mathrm{mix}}}{\tau_{\mathrm{chem}}}, \tag{6.4}$$

where τ_{mix} is the fluid-mechanical molecular-mixing time. Flows with $\mathrm{Da} \gg 1$ are characterized by kinetically-fast chemical reactions and the amount of product formed is limited by the amount of mixing achieved. In this regime, product formation is directly related to the amount of heat released to the system and this property has been exploited in several experimental investigations. From a computational standpoint, however, kinetically-fast reactions pose a challenge if the source term is treated in an explicit manner, as is done in this work. We further discuss the stiffness of the reaction mechanism in sec. 6.3.1.

6.2 Experimental and computational setup

The computational simulations we carry out are intended to reproduce the experimental results that were obtained by Dimotakis and his research group at the Supersonic Shear Layer Facility ($\mathrm{S^3L}$) at the California Institute of Technology. A detailed description of this experimental apparatus can be found in Mungal and Dimotakis (1984) and Hermanson and Dimotakis (1989). In particular we focus on a set of experiments at high Reynolds number that were performed by Slessor et al. (1998) to investigate the effects of the inflow boundary conditions on the mixing layer.

We first briefly describe the experimental setup that was used by Dimotakis's group

and use this information to justify the choice of computational domain, grid topology and boundary conditions we made in the numerical reconstruction. Next, we introduce the set of four initial conditions that were used in the experiments and analyze their numerical stiffness with the help of a zero-dimensional, perfectly stirred reactor model.

6.2.1 Computational domain and boundary conditions

Figure 6.1 shows a sketch of the GALCIT Supersonic Shear Layer (S^3L) facility that was used to generate the mixing layers. This is a two-stream, blow-down wind tunnel, nominally operating at atmospheric (static) temperature. Gas for the two free streams is supplied by independent flow systems. Coarse-mesh-screen, honeycomb, and a series of fine-mesh-screen sections are used for turbulence management. The two streams are separated in their respective plena by a splitter plate, which is flat on the top (high-speed) surface and curved on the bottom (low-speed) surface. A detailed view of the splitter plate, taken from Slessor et al. (1998), is shown in fig. 6.2.

In this work, we simulate only the test section of the apparatus, which is highlighted by the red box in figure 6.1. The splitter plate in the experiments has a fairly sharp trailing edge (about 0.050") with an included angle of ~ 4 degrees. The instrument rake, where all the experimental measurements were taken, is located at $x = 36.5$ cm downstream of the splitter plate trailing edge. The instrumentation used was able to determine time averaged pressure and temperature profiles. Using incompressible relations it is possible to determine the time averaged velocity profile from the pressure measurements.

The computational domain has dimensions $[0, 0.80] \times [-0.10, 0.05] \times [0, 0.084]$ meters in the streamwise (x), transverse (y) and spanwise (z) directions and the origin is placed on the upper side of the splitter plate's trailing edge. The grid is heavily stretched in the transverse direction, so that at least 15 to 20 grid elements are used to capture the boundary layer profiles. With this spacing, the finite thickness of the splitter plate tip (fig. 6.2) is very coarsely taken into account by separating the upper and the lower streams with two grid points. The transverse stretching then relaxes downstream to become essentially isotropic at the measurement station ($x = 36.5$ cm). The grid relaxation approximately follows the spread of the mixing layer as determined by preliminary simulations, so that it is much finer in the shear layer region, while it

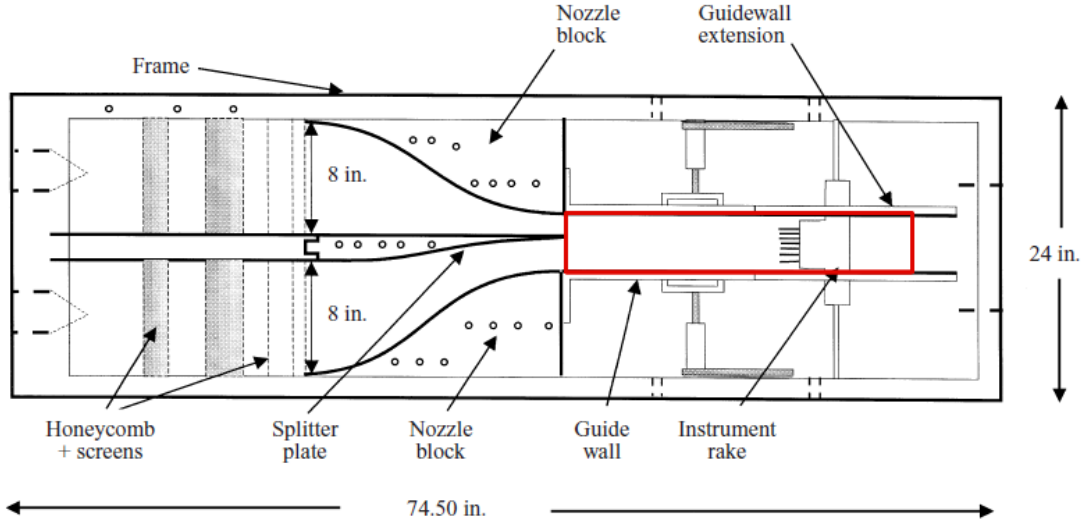

Figure 6.1: Experimental setup used by Slessor et al. (1998). The red rectangle denotes the computational domain used in this work.

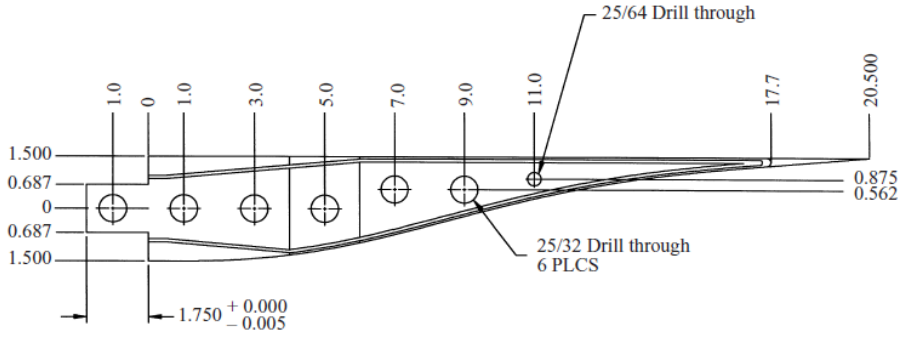

Figure 6.2: Detailed view of the splitter plate used in the experiments. Taken from Slessor et al. (1998).

rapidly coarsens away from the layer. We use 120 equally spaced points in the spanwise direction. The total number of points is about 16 million. We did not perform any grid refinement studies. In the two-dimensional cases we use the same grid with only one element in the z direction.

We employ periodic boundary conditions in the spanwise direction, whereas on the top and bottom walls we prescribe inviscid-slip conditions so that no attempt is made to resolve the boundary layers developing on these walls. At the inflow boundary, we impose

laminar boundary-layer profiles that match the values of the displacement thickness reported in Slessor et al. (1998), along with a characteristics-based inflow boundary conditions (Poinsot and Lele (1992)). At the subsonic outflow boundary, we use the characteristic boundary conditions of Rudy and Strikwerda (1981). It is well known (Poinsot and Lele (1992)) that these boundary conditions, especially when used for unsteady flows, are not perfect and can produce reflections from the boundaries that pollute the solution. In order to reduce this effect, we added a "sponge layer" which uses a combination of grid coarsening and added numerical dissipation to damp acoustic disturbances between streamwise position $x = 0.5$ m and the outflow boundary.

An additional issue that arises in chemically reacting mixing layers is that the heat released in the flow by the chemical reactions creates a mean pressure gradient that can accelerate/decelerate the flow. To correct for this effect, we followed the strategy employed by Hermanson and Dimotakis (1989) and adjusted the lower wall angle (β) of the domain to make $dp/dx \simeq 0$ (see fig. 6.3). This angle is not known *a priori*; in pre-

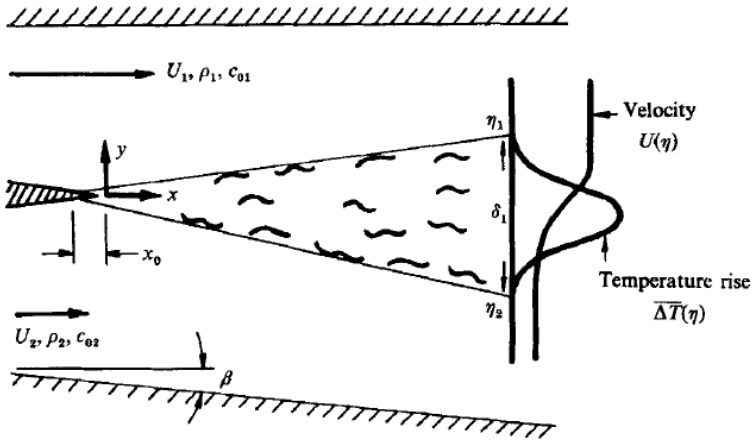

Figure 6.3: Schematic representation of the mixing layer and the definition of the lower guide-wall angle β.

vious analyses performed by Hermanson and Dimotakis (1989) and Dimotakis (1991), it was found to depend on the entrainment rate from each stream, which, in turn, is a function on the mixing layer flow parameters and heat release. In particular, the angle assumes a slightly negative value for zero and for very low heat release, while it becomes positive for high heat release cases. After experimenting with different angles

using two-dimensional simulations, we found that the value that minimized the pressure gradient for this case is $\beta = 0.01$ radians and is the angle used in defining the numerical domain.

6.2.2 Initial conditions

The four cases investigated by Slessor et al. (1998) are summarized in table 6.1. All

Case 1	Fluorine-rich ($\phi = 8$, $\Delta T_{\mathrm{ad}} \simeq 171$ K): Upper stream: 8.00% Ar, 15.07% He, 0.93% H_2, 0.14% NO, 75.86% N_2 Lower stream: 16.00% He, 8.00% F_2, 76.00 % N_2
Case 2	Hydorgen-rich ($\phi = 1/8$, $\Delta T_{\mathrm{ad}} \simeq 267$ K): Upper stream: 8.00% Ar, 4.00% He, 12.00% H_2, 0.75% NO, 75.25% N_2 Lower stream: 6.45% Ar, 16.00% He, 1.55% F_2, 76.00 % N_2
Case 3	Hydorgen-rich, reduced concentration ($\phi = 1/8$, $\Delta T_{\mathrm{ad}} \simeq 171$ K): Upper stream: 8.00% Ar, 8.00% He, 8.00% H_2, 0.50% NO, 75.50% N_2 Lower stream: 6.97% Ar, 16.00% He, 1.03% F_2, 76.00 % N_2
Case 4	Non-reacting: Upper stream: 8.00% Ar, 16.00% He, 76.00% N_2 Lower stream: 8.00% Ar, 16.00% He, 76.00% N_2

Table 6.1: Freestream compositions and adiabatic flame temperatures.

cases have a velocity ratio $r = U_2/U_1 = 0.4$ with upper and lower stream velocities $U_1 = 100$ m/s and $U_2 = 40$ m/s, respectively, while the density ratio is $s = \rho_2/\rho_1 = 1$. The initial static temperature is 292 K and the initial static pressure is 1 atm. The only difference between the cases is in the initial reactant concentrations. The three sets of reacting cases were performed to recreate "flip experiments" (Mungal and Dimotakis (1984)), where the stoichiometric-mixture ratios between the reactants are inverted. Case 3 is used to demonstrate that the experiments lie in the fast-kinetic regime by initializing the flow with a reduced concentration of reactants and verifying that the mixing layer profile remains unchanged. The reduced concentration effectively decreases the Damköhler number by increasing τ_{chem} while holding τ_{mix} constant (eq. (6.4)).

6.2.3 Numerical specifications

For all cases simulated we modeled the dynamic viscosity, μ, using Sutherland law, while the Prandtl and Schmidt numbers are assumed constant and equal to $\mathrm{Pr} = \mathrm{Sc} = 1$.
We use the Spalart-Allmaras turbulence method with the modifications described in sec. 2.2.1 with $\mathrm{Pr_T} = \mathrm{Sc_T} = 0.7$. The equations are integrated in time using an explicit, third-order accurate Runge-Kutta scheme with a CFL number kept fixed at $\mathrm{CFL} = 0.75$. Because of the very small grid spacing close to the splitter plate, this resulted in a very small time step that made the 3D simulations very expensive to run. Other than the grid spacing, the very fast chemical reactions also pose a severe restriction of the maximum time step that is allowed for explicit simulations. We discuss this issue in the validation of chemical scheme section (sec. 6.3.1).

We initialized the domain using $\mathrm{NPC_{init}} = 40$ particles per cell. We introduce one particle per cell in the inflow every two iterations in the upper (high-speed) stream and one particle every four iterations in the lower (low-speed) stream. As we show in the results section, due to the very small Δt, this is more than sufficient to guarantee enough particles in the freestream. We also employ a clustering algorithm to prevent the number of particles per cell from growing too much in certain areas of the domain and slow down the simulation. This threshold is kept fixed at $\mathrm{NPC_{thre}} = 150$ particles per cell. In order to further save computational resources, we do not use FMDF particles in the sponge layer and destroy them as soon as they pass $x = 0.5$ m.
The mixing model constant is kept fixed at $C_\Omega = 6$ and the filter width, also used by the mixing model, is $\Delta = 0.0007$ m which corresponds to the smallest grid spacing in the computational domain.

6.3 Results

We carry out two 2D simulations, corresponding to cases 1 and 3 of table 6.1. Due to the time step limitations, we were able only to perform one three-dimensional simulation for the fluorine-rich case 1. We also analyze the stiffness and the time step constraints of the chemical reaction scheme using a zero-dimensional, well-stirred reactor.

6.3.1 Validation of the chemistry model

The well-stirred reactor is a zero-dimensional (only chemical source terms are active) solution of the chemical species and energy equations (at constant pressure), starting from some well-defined set of initial conditions. It employs the same chemistry routines that are used in the fluid dynamics code and is used both to validate the reaction mechanism and to study the kinetics of the reactions as a function of the initial concentrations. Figure 6.4 shows the evolution of temperature and product mass fraction (HF) for an

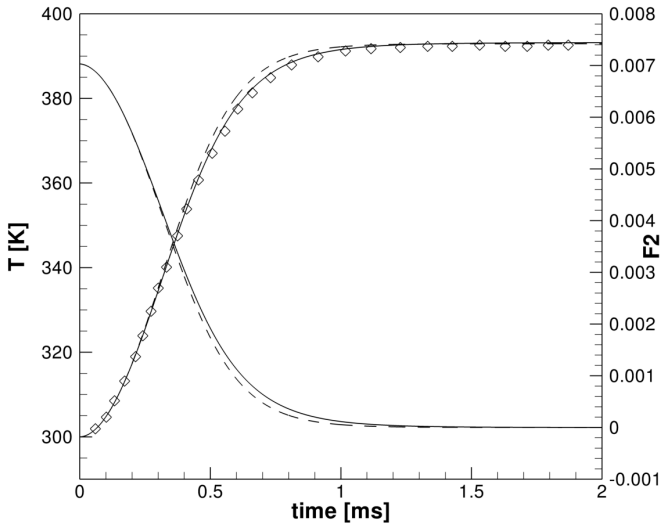

Figure 6.4: Temperature and F_2 mass fraction evolution for 4% H_2 and 0.5% F_2 and 0.015% NO in an N_2 diluent. Solid lines are for the full reaction set, eqs. (6.2a-6.3d). Dashed lines are for the reduced set, eqs. (6.2a-6.2c). Diamond symbols were obtained by Mungal and Frieler (1988) using the CHEMKIN software. $\Delta T_{\mathrm{ad}} = 93K$ for this case.

initial concentration of 4% H_2 and 0.5% F_2 and 0.015% NO in an N_2 diluent, which corresponds to a mixing layer with 8% H_2 and 0.030% NO on the high-speed side and 0.5% F_2 in on the low-speed side. The curves exactly reproduce the results obtained by Mungal and Frieler (1988) using the CHEMKIN software.

By looking at the similarity of the curves obtained using the full reaction set, eqs. (6.2a-6.3d), as compared to the reduced set, eqs. (6.2a-6.2c), it is evident that the first three dominate the behavior of the system at the temperature of interest. Nevertheless,

in all the simulations performed in this work, we used the complete reaction set, eqs. (6.2a-6.3d). The maximum heat released in the system, which determines the adiabatic flame temperature rise ΔT_{ad}, is a function only of the initial concentrations of F_2 and H_2. We also ran simulations using concentrations resulting from mixing different volumes of

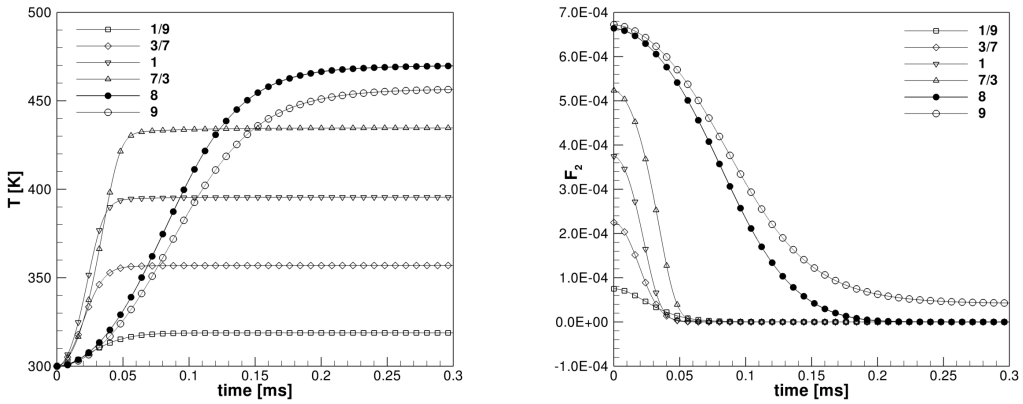

Figure 6.5: Temperature (left) and F_2 mass fraction (right) time evolution for different ratios of upper and lower stream fluid corresponding to case 1. The stoichiometric ratio ($\phi = 8$) is shown with solid symbols and reaches $\Delta T_{\mathrm{ad}} \simeq 171K$, as reported in Slessor et al. (1998).

top and bottom stream fluid corresponding to case 1 ($\phi = 8$, fluorine rich), which are shown in fig. 6.5. The purpose of these plots is to get a better idea of the heat release and the kinetics when different volumes of the upper and lower stream get mixed as would happen due to mixing and entrainment. Furthermore, as we are using an explicit time integration scheme, these simulations help us to determine a stable time step. It was found that, although case 2 and 3 are, on the whole, kinetically slower compared to case 1, the time step required for stability is more stringent due to the higher concentration of H_2. The numerically stiffest reaction, due to the high value of the equilibrium constant, is the exchange reaction (6.2a). In order to obtain a numerically stable solution with the initial concentration that characterize cases 2 and 3, we had to lower the time step to $\sim 1/3$ of the one used for case 1 and that made the three-dimensional simulations too expensive to run for the available computer resources.

6.3.2 Two-dimensional results

In this section we present the two-dimensional results for case 1 and 3. As table 6.1 shows both cases have the same adiabatic temperature rise, $\Delta T_{\text{ad}} \simeq 171$ K but are "flipped", in the sense that case 1 is fluorine-rich and case 3 is hydrogen-rich.

As discussed previously, an important aspect of these simulations is to adjust the angle of the lower guidewall to ensure a nearly zero mean pressure gradient which could otherwise alter the velocity field. That the value of $\beta = 0.01$ rad used in this work is adequate is demonstrated in fig. 6.6, where the mean pressure and velocity profiles are plotted close to the bottom guidewall. The pressure profile for the straight-walled case, $\beta = 0$ rad, is also shown for comparison. It is evident that in this case, there is an almost constant positive pressure gradient that causes the flow to slow down significantly and highlights the importance of obtaining $\partial p/\partial x \approx 0$.

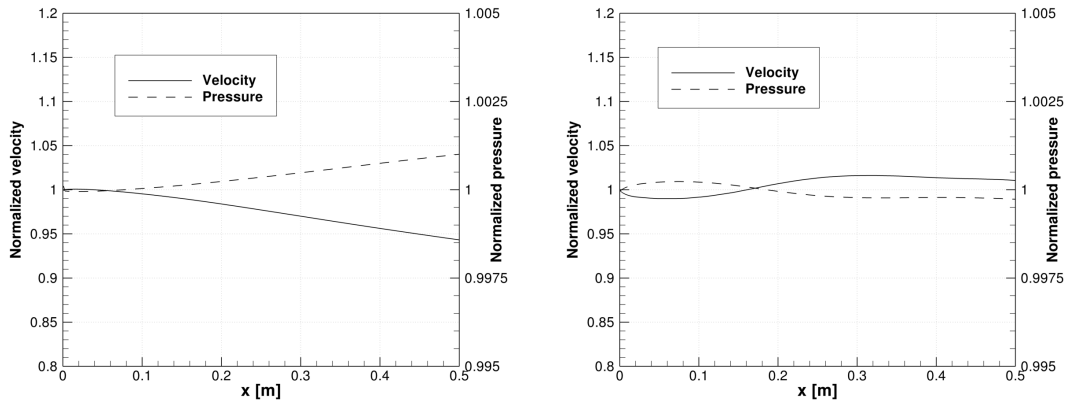

Figure 6.6: Mean velocity and pressure profiles on the lower guidewall for a straight domain, $\beta = 0$ rad (left) and for a divergent one, $\beta = 0.01$ rad (right). Both quantities are normalized with their freestream values.

Figure 6.7 shows the instantaneous mass fractions of the reactant, F_2 and H_2, and of the product HF for case 1 after about 2 flow times. The mixing layer becomes unstable and naturally transitions to a turbulent state, without the need of any artificial forcing. The contour plot of H_2 clearly shows that there are no intermediate concentrations of hydrogen: $\widetilde{c}_{H_2}$ is either zero or at its free stream value. This is a confirmation that H_2 is the lean reactant for this case and also that the reaction kinetics is very fast, as the

hydrogen gets converted into HF almost instantaneously as soon as it gets mixed with fluorine.

In fig. 6.8 we show a comparison between the filtered FMDF mass density, eq. (4.8), the particle density, eq. (4.7) and the number of particles per cell (NPC). As for the temporal mixing layers, also in this case there is an excellent agreement between the two density fields, although the particle field is affected by the typical noise to be expected in stochastic simulations. The number of particles per cell contour plot highlights a number of important aspects of the FMDF simulation. First, we demonstrate that the number of particles per cell is everywhere above 15. Colucci et al. (1998) and Givi (2006) note that the optimal NPC should be around 40. This condition is essentially verified in most of the domain, with the exception of the final part, past the measurement station at $x = 36.5$ cm, where, in certain areas, NPC drops to about 20. Secondly, the picture highlights the importance of having a clustering algorithm to reduce NPC in selected areas. Without this capability there would be an unnecessary accumulation of particles, especially where the grid is more stretched towards the end of the domain, that would considerably slow down the simulation without any improvements to the accuracy. Lastly, it can be noticed how there are some streaks of high NPC, followed by areas of relatively low NPC. We think this effect is caused by the vertical velocities that are induced by the mixing layer and that cause the particles alternatively to be lifted towards the layer and away from it.

In fig. 6.9 we compare the mass fraction of hydrogen for case 1 and case 3 at the same time. The purpose of this picture is to highlight the different degree of mixing of hydrogen when it the lean reactant (case 1) or when it is the rich one (case 3).

The differences between the two cases are evident from fig. 6.10, where we plot the instantaneous temperature rise obtained by the model-free LES and the FMDF for case 1 together with the FMDF results for case 3. The temperature rise is normalized with the adiabatic flame temperature, which is the same for both cases ($\Delta T_{\mathrm{ad}} = 171$ K). The first important observation is that, similarly to what we already pointed out in the previous chapter, the model-free LES results show a much higher temperature as compared to the FMDF ones. This higher temperature profile implies that there is a higher product formation (HF) than what is predicted by FMDF. Furthermore, the FMDF results never exceed the adiabatic flame temperature, unlike the model-free LES

which displays some some regions where $(\Delta T/\Delta T_{\mathrm{ad}}) > 1$. It is also worth noticing that, although both case 1 and 3 have the same ΔT_{ad}, the temperatures reached for case 3 are markedly lower than those reached by case 1. This is an effect of the different entrainment ratio between the high-velocity (top) stream and the low-velocity (bottom) stream, and it depends on which stream carry the lean reactant (Dimotakis (1991)).

Finally, in fig. 6.11, we plot the time averaged temperature profiles for the two cases and the corresponding experimental data obtained by Slessor et al. (1998). The computational results for the fluorine-rich case 1 capture the shape of the experimental measurements quite well but they consistently under-predict the temperature rise. The maximum difference in temperature is located close to the peak of the curve and is about 12 K, which corresponds to 7% of ΔT_{ad}. Conversely, the maximum mean temperature rise predicted by the simulations for case 3 is in good agreement with the value reported in the experiments, but the shape of the profile is tilted towards the high-speed (top) side. In addition, the computational curve seems to be more flat on top and to under-predict the product formation on the low-speed (bottom) side. It is not entirely clear what might be causing the discrepancies but the two-dimensionality of the LES plays an important role, as shown in the next section. It is also worth noticing that the FV/FMDF results are in much closer agreement with the experiments than the model-free LES results that are reported in Ferrero et al. (2013).

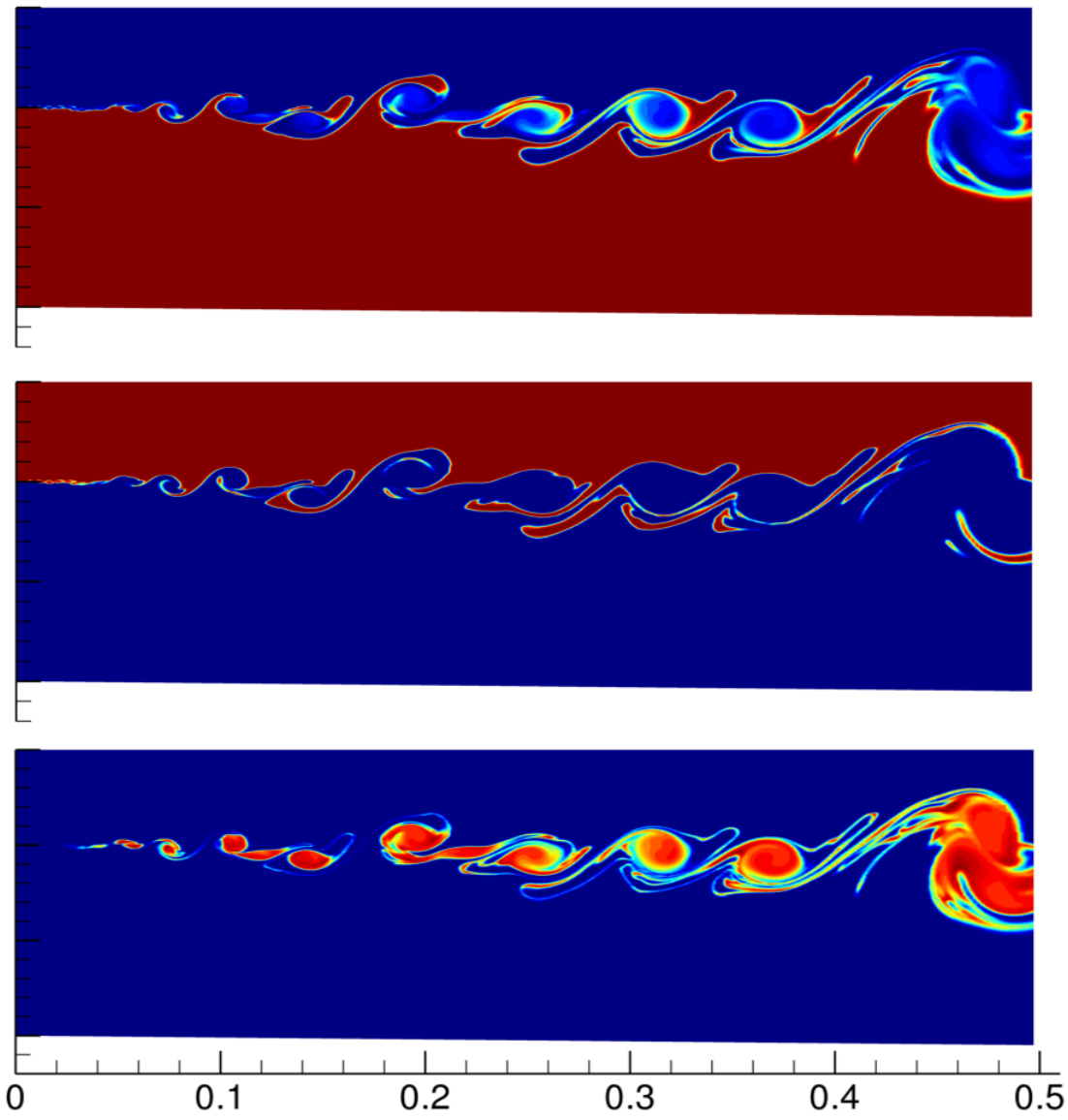

Figure 6.7: Instantaneous snapshots of the filtered mass fraction of F_2 (top), H_2 (center) and HF (bottom). The F_2 contour plot has 24 levels from 5 % to 12 %, H_2 has 14 levels from 0.005 % to 0.07 % and the product (HF) has 26 levels from 0.05 % to 1.3 %. Case 1 (fluorine-rich) at $t = 0.025$ s ($\sim$ 2 flow times).

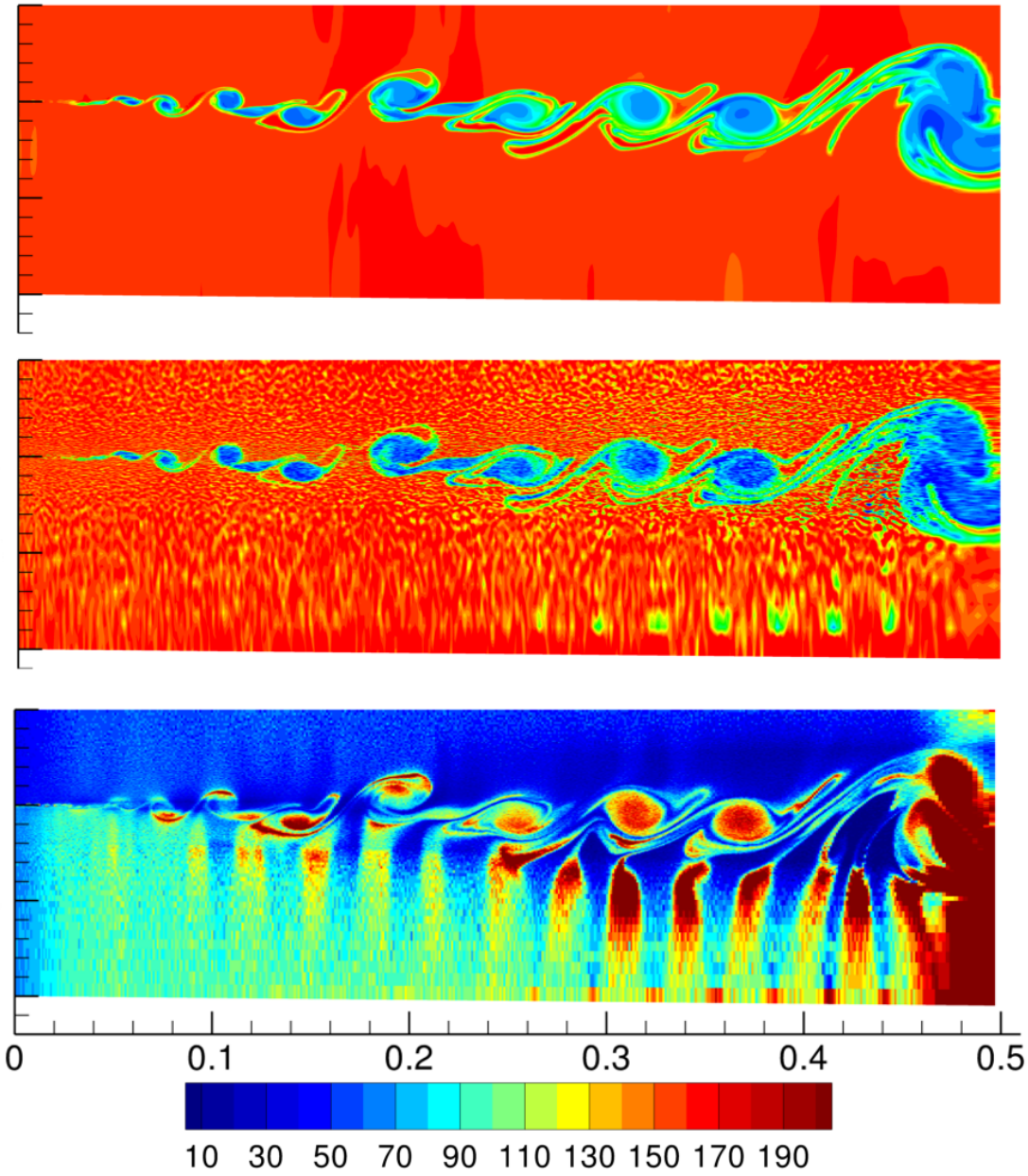

Figure 6.8: Instantaneous snapshots of the filtered FMDF density (top), the particle density (center) and the number of particles per cell (NPC) (bottom). Both density plots have 20 levels from 0.64 to 1.02 kg/m^3, while NPC has 20 levels from 10 to 200. Note that no particle clustering algorithm was used for this case. Case 1 (fluorine-rich) at $t = 0.025$ s ($\sim$ 2 flow times).

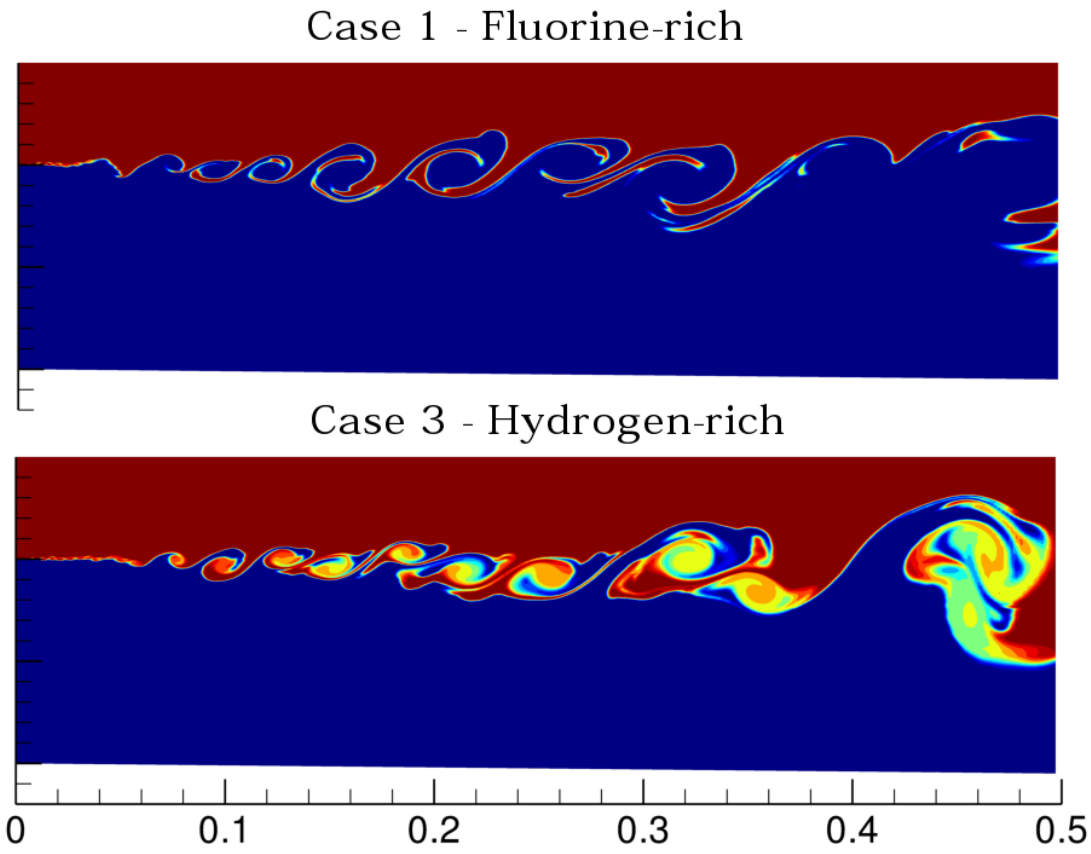

Figure 6.9: Instantaneous snapshots of the filtered mass fraction of H_2 for case 1 (top) and case 3 (bottom) at $t = 0.0125$ s (~ 1 flow time). Hydrogen is the lean reactant in case 1 ($\phi = 8$) but it is the rich one in case 3 ($\phi = 1/8$). The contour plot for case 1 has 14 levels from 0.005 % to 0.07 %, while the one for case 3 has 12 levels from 0.05 % to 0.6 %.

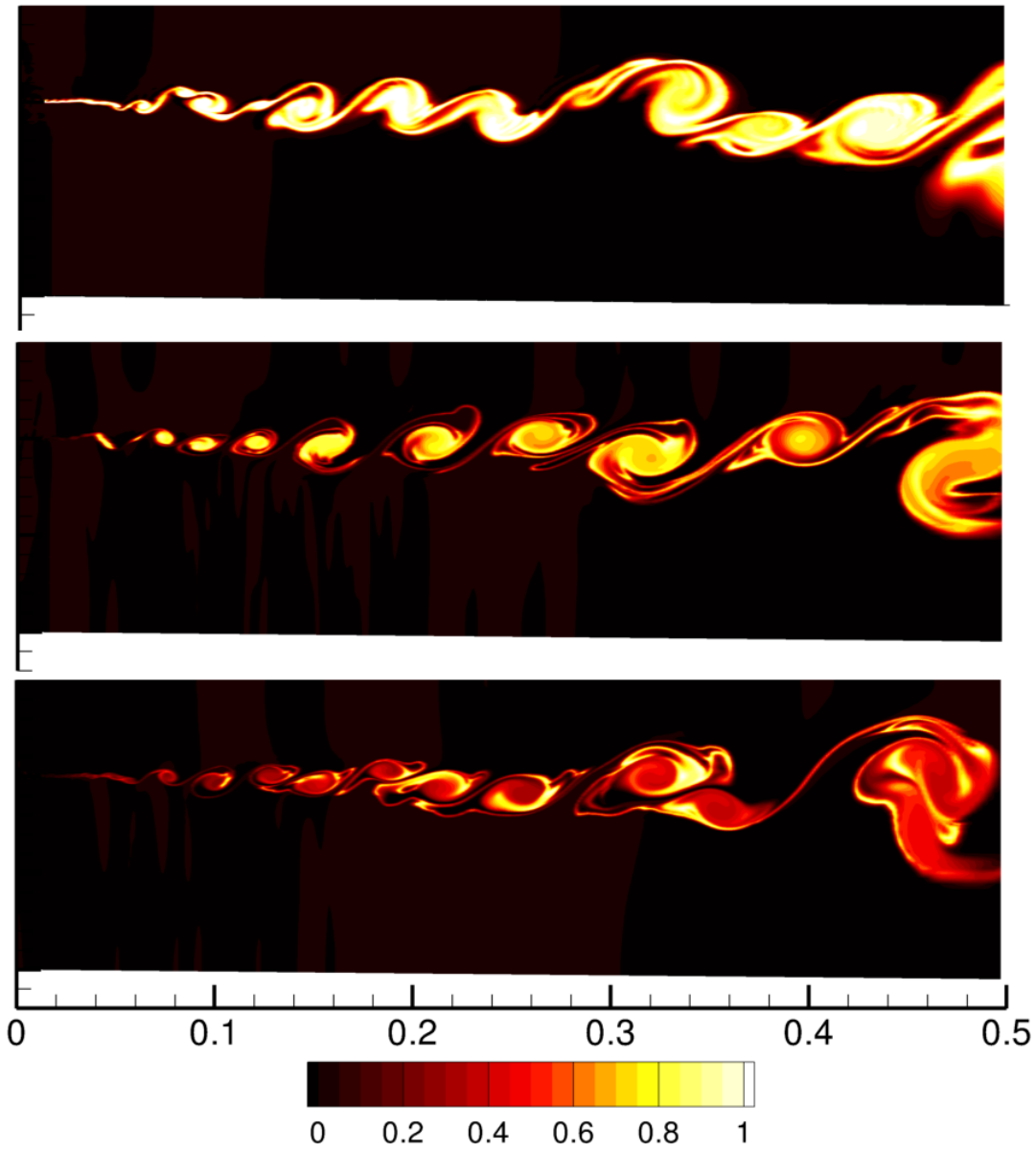

Figure 6.10: Instantaneous snapshots of the normalized temperature rise ($\Delta T/\Delta T_{\mathrm{ad}}$) for case 1: conventional LES (top) and FMDF results (center). The bottom plot shows the FMDF results for case 3. All plots are obtained at $t = 0.0125$ s (~ 1 flow time) and have 21 levels from 0 to 1.

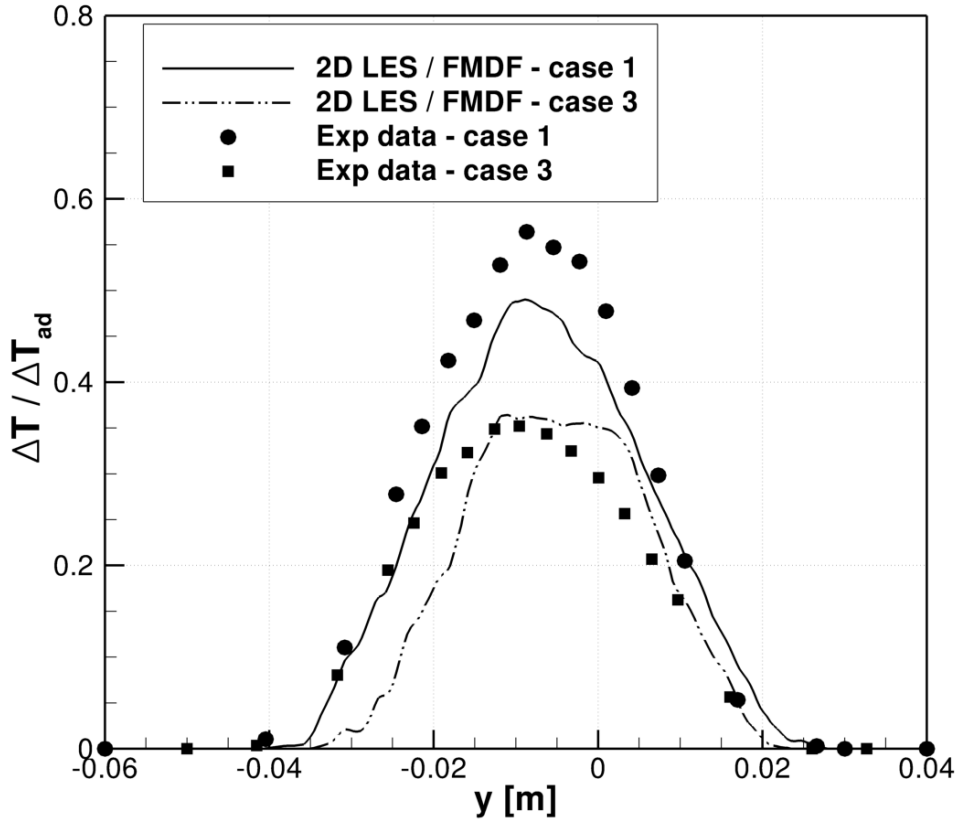

Figure 6.11: Time-averaged temperature rise at the measurement station ($x = 36.5$ cm). Solid lines denote the results of the 2D computations, while the dots represent experimental measurements. The temperatures are normalized using the adiabatic flame temperature rise ΔT_{ad}.

6.3.3 Three-dimensional results

In this section we present the 3D results obtained for case 1 (fluorine-rich). We were only able to perform a 3D simulation for this case because of the limitations imposed by the stiff chemistry terms on the maximum time step that we discussed in sec. 6.3.1. We use 120 points in the spanwise (z) direction, for a total of about 16 million elements for the grid. Even using the particle clustering algorithm and capping the maximum number of particles allowed in a cell at 150, the total number of particles that are simultaneously present inside the domain exceeds 900 million. We use the same numerical parameters as in the 2D simulations (sec. 6.2.3). The time averaged data that we show in this section has been further averaged along the statistically homogenous direction (z) in order to increase the number of samples.

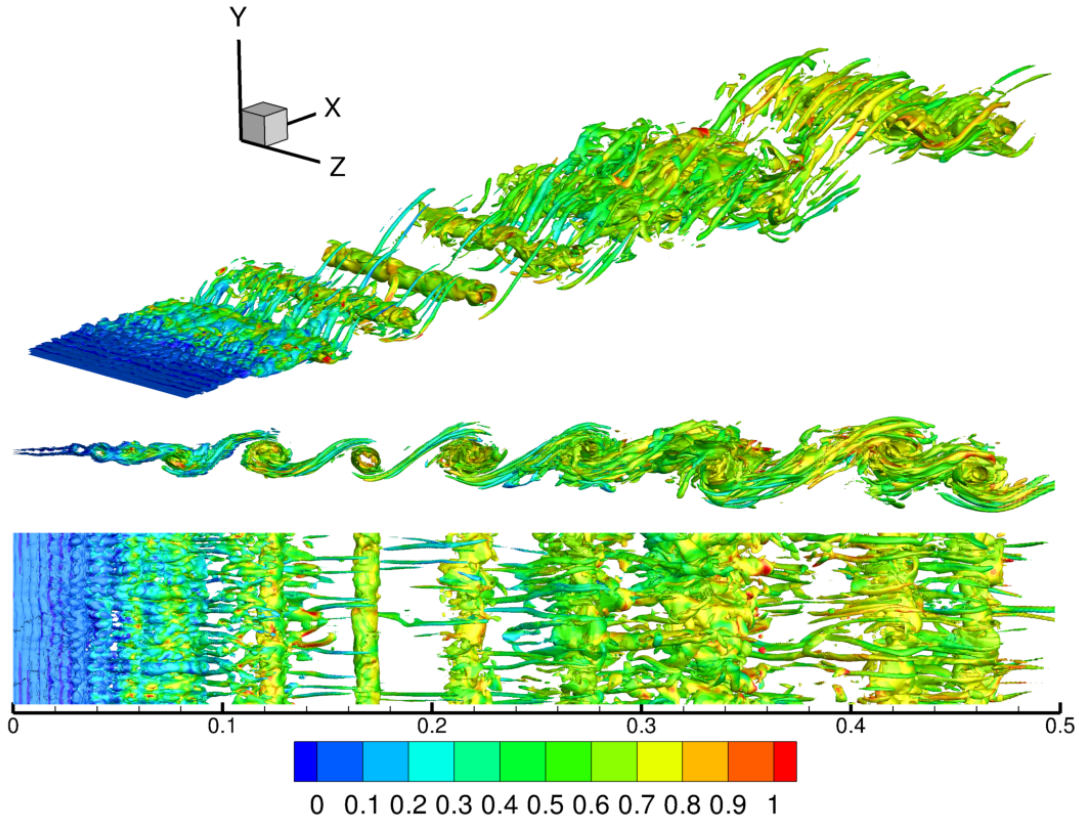

Figure 6.12: Iso-surfaces of vorticity magnitude colored with the local value of the normalized temperature rise. Case 1 at $t = 0.0125$ s ($\sim$ 1 flow time).

The three-dimensional flow field is depicted in fig. 6.12, where we plot the iso-surfaces of vorticity magnitude colored with the local value of the normalized temperature rise. The process through which the flow becomes unstable, forms the characteristic roller structures and becomes turbulent after $x \sim 30$ cm can be clearly seen. The flow starts "cold" but becomes hotter downstream as the reactants come into contact due to the turbulent mixing. The mean profile for the streamwise velocity is shown in fig. 6.13. It shows an excellent agreement with the experimental data obtained by Slessor et al. (1998). Both the spread and the shape of the mixing layer are well captured by the simulation.

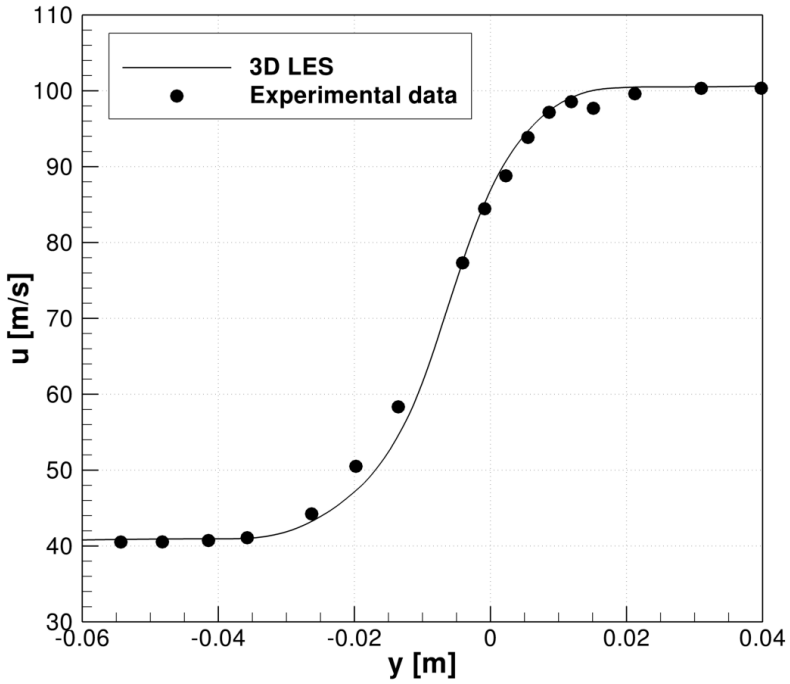

Figure 6.13: Mean velocity profile at x = 36.5 cm downstream of the splitter plate tip. The solid line is the present simulation. The dots represent the experimental results obtained by Slessor et al. (1998).

Figure 6.14 is a 3D representation of the mass fractions of the reactant and the product. Because H_2 is the lean reactant for this case, it is essentially absent in the mixed state, as already noticed for the two-dimensional case. The solution is clean and smooth and

does not appear to be affected by numerical noise.

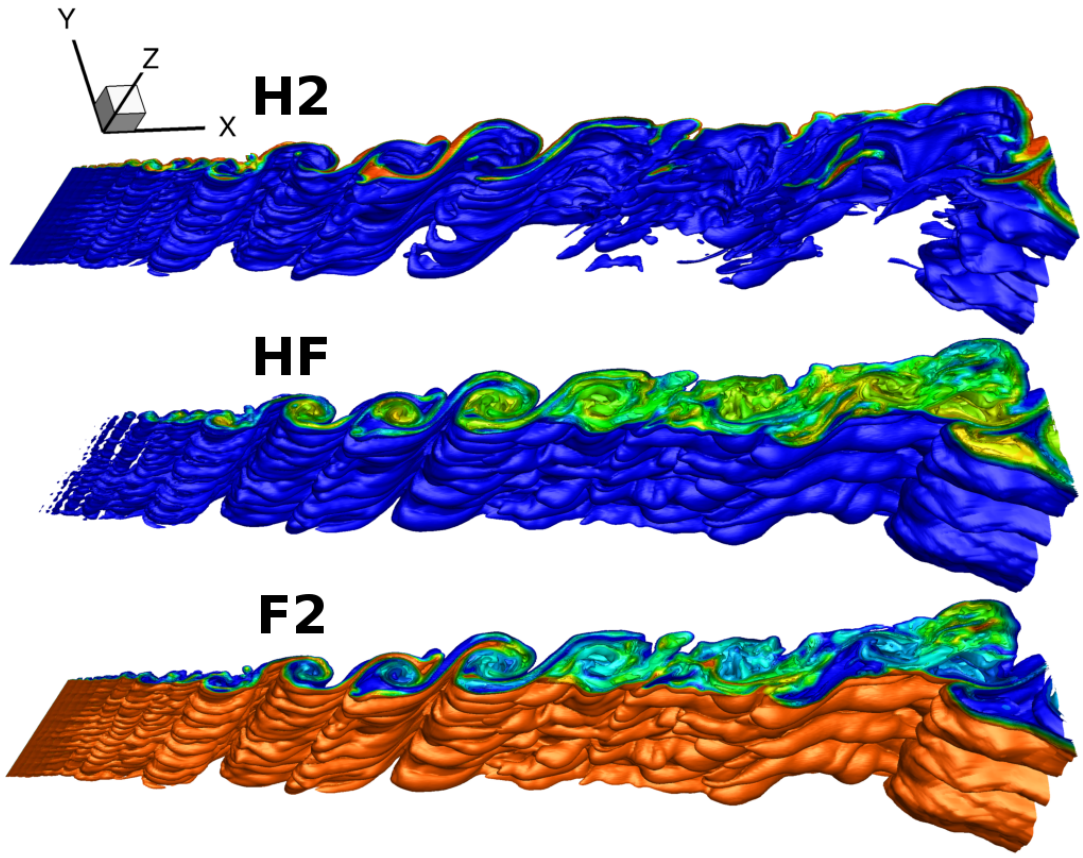

Figure 6.14: Iso-surfaces of reactant and product mass fractions at $t = 0.0125$ s ($\sim$ 1 flow time).

The results for the z-averaged mean temperature rise are shown in fig. 6.15. These statistics were collected for about one flow time. The three-dimensional simulation slightly over-predicts the rise in temperature on the high-speed (top) stream but the peak average temperature is well captured and the overall agreement with the experimental data is much better than model-free LES.

6.3.4 Concluding remarks

This flow field is challenging to simulate for a number of reasons. First, it is characterized by a fairly large Reynolds number which implies that a large number of points must

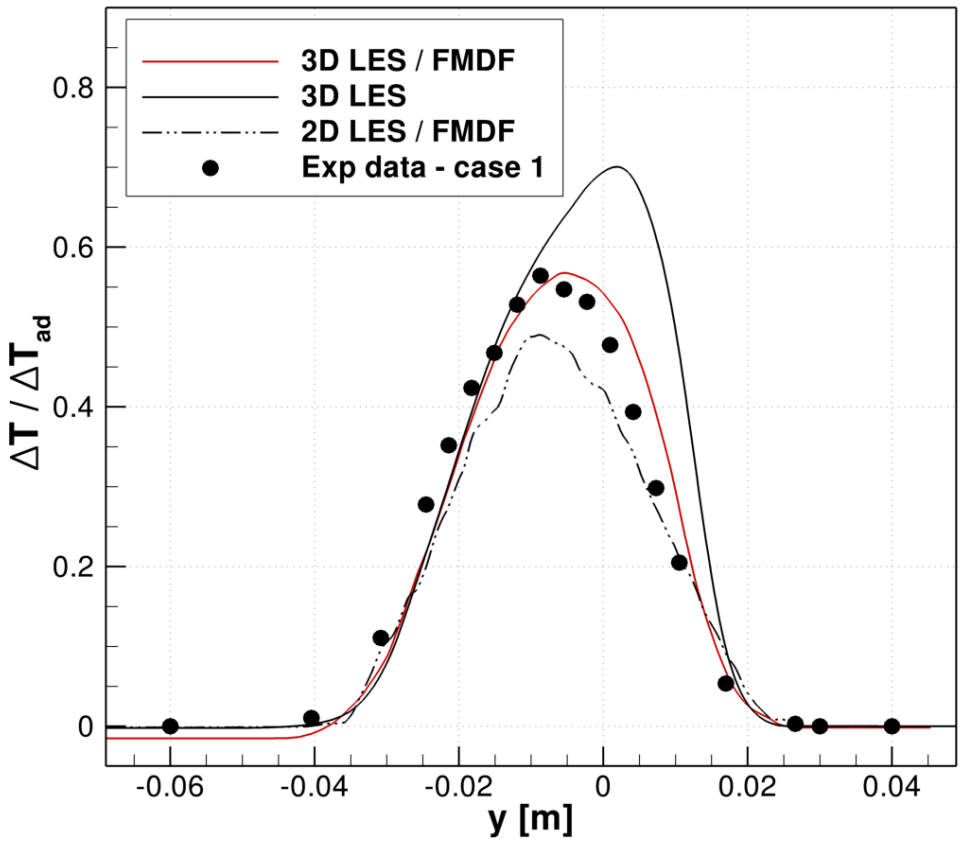

Figure 6.15: Mean temperature rise at the measurement station ($x = 36.5$ cm). The red line denotes the z-averaged 3D LES/FMDF results while the dots represent the experimental measurements. The profiles for the 2D LES/FMDF and for the model-free LES (solid line) are also shown for comparison.

be used to adequately resolve the LES. Second, there is wide range of length scales that implies a lot of grid stretching: we need to resolve the tiny splitter plate trailing edge as well as the inflow boundary layers and still be able to obtain uniform spacing after the mixing layer has developed. Third, the flow is composed of 10 species, which are characterized by sharp interfaces when the streams come into contact. Lastly, the reaction mechanism is characterized by very fast reactions that limit the maximum stable time step for explicit calculations. Given all these difficulties, we are able to reproduce

very accurately (within 5% difference) the experimental measurements for the mean streamwise velocity and, more importantly, we obtain a good agreement for the mean temperature rise. The fact that we don't have an exact match with the experiments could be explained by the assumption we made to neglect differential diffusion, which may be important in a case where hydrogen is present. A second possible source of discrepancies between the numerical and the experimental results is the fact that, in the simulations, we did not resolve the boundary layers that form on the higher and lower guide walls. Although these boundary layers are very thin, the displacement they exert on the flow could partially explain the slight shift between the experimental and numerical curves of fig. 6.15.

In addition the results show that the 3D simulations are in much better agreement to the experimental data as compared to the 2D ones. These findings highlight the importance of the three-dimensional character of these flows, arguing against the accuracy of 2D simulations.

Once again, it is clear that including the effects of the turbulent/chemistry interaction does significantly improve the accuracy of the simulations.

Chapter 7

Summary and conclusions

In this work we present the results of large-eddy simulations of turbulent, chemically reacting flows. The accurate simulation of these flows involves additional challenges as compared to non-reacting cases: the large number of species involved, the wide spectrum of time and length scales that are present and the coupling of large turbulent fluctuations with non-linear chemical kinetics. This last issue is particularly important in the context of large-eddy simulations (LES) and Reynolds-averaged Navier Stokes simulations (RANS) but, due to the lack of general models, it is sometimes ignored. One of the main objectives of this work is to take this coupling into account and investigate its effects on the results. We achieve this goal by implementing the filtered mass density function (FMDF) methodology in an existing high-resolution, unstructured fluid dynamics solver. This methodology belongs to the class of transported PDF methods, which aims at providing a statistical description of the sub-grid scale chemical composition and temperature/enthalpy of the flow. The FMDF methodology achieves this improved description by solving a transport equation for the distribution function of the sub-grid scale (SGS) fluctuations of mass concentration and enthalpy. The numerical solution of the FMDF transport equation is obtained with a stochastic Monte Carlo method which utilizes an ensemble of "stochastic" particles. These particles, which are not representative of the real fluid particles but are a numerical tool to obtain the filtered mass density function, are convected in a Lagrangian fashion throughout the domain. The effects of mixing are included by using a mixing model.

Since its introduction in LES in the late '90s, the FMDF methodology showed a great

potential to provide a general way to include the effects of the turbulence/chemistry interactions and, thus, to significantly improve the accuracy of the computations of turbulent reactive flows. Despite its successes, however, very few research has been done in extending FMDF methods to compressible, high-Mach number flows and its use has been mostly limited to simple geometries. In this work we take a step towards overcoming those limitations by extending the FMDF formulation to compressible flows and by implementing it in an unstructured framework which expands the range of problems that can be simulated. Furthermore, we use the same parallel infrastructure as the finite volume (FV) fluid dynamic solver and this feature enables us to run problems of considerable size, which have rarely been attempted previously in the context of the hybrid FMDF/FV methodology.

The first part of this thesis deals with the mathematical formulation of the hybrid finite volume/Monte Carlo scheme and provides a detailed description of the algorithmic implementation. In the second part, we first validate the hybrid solver by comparing some of the redundant variables - those which are calculated both by the finite volume and by the FMDF solver - in non-reacting flows. We demonstrate the consistency of our implementation by showing that the two sets of redundant variables are in good agreement with each other, as expected for chemically inert flows. One important finding is that, although the agreement is excellent at the level of the first moment (filtered quantities), the results for the second moment variables, such as the sub-grid scale variance, are more sensitive to numerical errors. We investigate several numerical parameters and we find that the SGS variance results are mostly affected by the grid resolution and by the size of the ensemble domain where the relevant statistics are collected from the particles' properties. For a given Reynolds number, by decreasing the ensemble domain width and by increasing the total number of grid points, we are able to recover good agreement between the FV and the FMDF solutions. We also validate the FMDF solver on compressible, high-Mach number flows and confirm that the method is not affected by the presence of discontinuities in the flow field.

Next, we apply the FMDF methodology to chemically reacting temporally developing mixing layers, in both compressible and incompressible regimes. We are able to demonstrate the increased accuracy of the FMDF simulations with respect to the

model-free LES by comparing the product formation against DNS results. The comparison clearly shows how neglecting the turbulence/chemistry interaction results in an over-prediction of the product formation for fast chemical kinetics. In contrast, when we use the FMDF methodology to model these effects, we find a much better agreement with the DNS data for the same grid resolution. These findings hold true for both incompressible and compressible cases.

In the final part of this work we perform two- and three-dimensional LES of high-Reynolds number, spatially developing, chemically reacting mixing layers with the intent of reproducing the experimental results obtained by Slessor et al. (1998) at the California Institute of Technology. This is a much more realistic and complex configuration as compared to the previous cases and it truly exploits the capabilities of the present implementation of the FMDF model in terms of grid complexity, resolution and total number of particles employed. The chemical reaction mechanism is the combustion of dilute concentration of hydrogen and fluorine into inert gases. We carry out two two-dimensional cases, corresponding to different, "flipped", initial concentrations of reactants. The results show the effects of the different entrainment ratio between the two streams, which manifests itself in the temperature profile when the initial location (upper stream or lower stream) of the lean reactant is reversed. The FMDF results appear to be much less diffused and resolve better the turbulent structures as compared to those obtained from conventional LES. Furthermore the time averaged temperature profile of the FMDF lies much closer to the experimental one, while the model-free LES results consistently over predict the temperature rise. The agreement with the experimental data is better for the hydrogen-rich case than for the fluorine-rich one, for which the temperature profile is slightly under predicted. We also conduct a fully three-dimensional simulation of the fluorine-rich case. This run pushes the limits of the FMDF solver as it is performed using over a thousand cores and it employs close to one billion stochastic particles. Although very expensive computationally, the results of the 3D case are very encouraging as we are able to obtain an excellent agreement with the time-averaged measurements of the velocity profile of the mixing layer. Furthermore the time averaged temperature rise profile shows a much better agreement with the experiments as compared to the 2D case and explains some of the discrepancies we found in the two-dimensional results. On the contrary, the model-free LES consistently

overpredicts the temperature rise, both in the 2D and 3D simulations.

In conclusion we have shown that effects of the turbulent fluctuations on the highly non-linear chemical source terms can have a large impact on large-eddy simulations of chemically reacting flows and that, therefore, they should always be included in the formulation. Although we do not prove it, it is reasonable to assume that the same holds true for RANS calculations. Many different models have been developed in the last thirty years to try to account for these effects, all of which can essentially be divided into two main categories: flamelet-like and PDF-like. We choose to utilize a method that belongs to the former category because, unlike the flamelet-like models, it neither restricts the chemical species to lie in low-dimensional manifold, nor it makes any assumptions on the shape of the resulting PDF (Pope (2012)).

In spite of these advantages, transported PDF methods for LES have not yet become as popular because they are not trivial to implement in existing fluid-dynamics solvers and because their use has been limited to relatively simple configurations. In this work we show that there is indeed a great potential for the use of these methodologies in practical problems. We establish that they are able to produce far superior results as compared to model-free LES and that, if properly implemented, the computational overhead cost is reasonable. We further demonstrate that the same results also apply for compressible flows, for which the research on turbulent combustion is not as developed as for the incompressible regime. In addition, the unstructured framework in which we developed the algorithmic procedure allows for the use of fairly complicated geometries and we believe this work is a step forward for the application of FMDF methods in realistic configurations such as SCRAMJET engines or other high-speed combustors. In order for this to happen, some more research efforts are needed to improve the algorithms that control the number of particles (cloning and clustering) and possibly to dynamically repartition the domain among the computational cores, so that computational bottlenecks are avoided. It is also important to consider that, for very complex reaction mechanisms, most of the computational time is spent in evaluating the source terms and that, therefore, this step requires very efficient algorithms.

References

A.A. Aldama. *Filtering techniques for turbulent flow simulation*, volume 56. Springer-Verlag Berlin, New York, 1990.

N. Ansari, G.M. Goldin, M.R.H. Sheikhi, and P. Givi. Filtered density function simulator on unstructured meshes. *Journal of Computational Physics*, 230(19):7132–7150, 2011.

A. Banaeizadeh, Z. Li, and F.A. Jaberi. Compressible scalar filtered mass density function model for high-speed turbulent flows. *AIAA journal*, 49(10):2130–2143, 2011.

J. Bardina, J.H. Ferziger, and W.C. Reynolds. Improved turbulence models based on large eddy simulation of homogeneous, incompressible turbulent flows. *Stanford Univ. Report*, 1, 1983.

M.D. Bartkowicz. *Numerical simulations of hypersonic boundary layer transition*. PhD thesis, University of Minnesota, 2012. URL `http://purl.umn.edu/121589`.

A.M. Bonanos, J.M. Bergthorson, and P.E. Dimotakis. Molecular mixing and flowfield measurements in a recirculating shear flow. part ii: supersonic flow. *Flow, turbulence and combustion*, 83(2):251–268, 2009.

J.E. Broadwell and R.E. Breidenthal. A simple model of mixing and chemical reaction in a turbulent shear layer. *Journal of Fluid Mechanics*, 125:397–410, 1982.

S. Catris and B. Aupoix. Density corrections for turbulence models. *Aerospace Science and Technology*, 4(1):1–11, 2000.

J.H. Chen, A. Choudhary, B. De Supinski, M. DeVries, E.R. Hawkes, S. Klasky, W.K. Liao, K.L. Ma, J. Mellor-Crummey, N. Podhorszki, et al. Terascale direct numerical simulations of turbulent combustion using s3d. *Computational Science & Discovery*, 2(1):015001, 2009.

H. Choi and P. Moin. Grid-point requirements for large eddy simulation: Chapmans estimates revisited. *Physics of Fluids*, 24:011702, 2012.

P.J. Colucci. *Large eddy simulation of turbulent reactive flows: Stochastic representation of the subgrid-scale scalar fluctuations*. PhD thesis, State University of New York at Buffalo, 1998.

P.J. Colucci, F.A. Jaberi, P. Givi, and S.B. Pope. Filtered density function for large eddy simulation of turbulent reacting flows. *Physics of Fluids*, 10:499, 1998.

P.E. Dimotakis. Turbulent free shear layer mixing and combustion. *Progress in Astronautics and Aeronautics*, 137:265–340, 1991.

F. Ducros, F. Laporte, T. Souleres, V. Guinot, P. Moinat, and B. Caruelle. High-order fluxes for conservative skew-symmetric-like schemes in structured meshes: application to compressible flows. *Journal of Computational Physics*, 161(1):114–139, 2000.

T. Echekki and E. Mastorakos. Turbulent combustion: Concepts, governing equations and modeling strategies. In *Turbulent Combustion Modeling*, pages 19–39. Springer, 2011.

P. Ferrero, G.V. Candler, and C. Otis. Filtered mass density function for variable-density turbulent reactive flows on unstructured meshes. *AIAA Paper*, 2964, 2012.

P. Ferrero, A. Kartha, P.K. Subbareddy, G.V. Candler, and P.E. Dimotakis. Les of a high-reynolds number, chemically reacting mixing layer. *AIAA Paper*, 3185, 2013.

R.O. Fox. *Computational models for turbulent reacting flows*. Cambridge University Press, 2003.

C.W. Gardiner. *Handbook of stochastic methods*, volume 13. Springer, 2009.

K. George and K. Vipin. Metis - unstructured graph partitioning and sparse matrix ordering system, version 2.0. Technical report, 1995.

Skorokhod A.V. Gickhman, I.I. *The Theory of Stochastic Processes II*. Springer, 1974.

P. Givi. Model-free simulations of turbulent reactive flows. *Progress in Energy and Combustion Science*, 15(1):1–107, 1989.

P. Givi. Filtered density function for subgrid scale modeling of turbulent combustion. *AIAA journal*, 44(1):16–23, 2006.

J.C. Hermanson and P.E. Dimotakis. Effects of heat release in a turbulent, reacting shear layer. *Journal of Fluid Mechanics*, 199:333–375, 1989.

F.A. Jaberi, P.J. Colucci, S. James, P. Givi, and S.B. Pope. Filtered mass density function for large-eddy simulation of turbulent reacting flows. *Journal of Fluid Mechanics*, 401:85–121, 1999.

W. Jou and J.J. Riley. Progress in direct numerical simulations of turbulent reacting flows. *AIAA journal*, 27(11):1543–1556, 1989.

P.E. Kloeden and E. Platen. Higher-order implicit strong numerical schemes for stochastic differential equations. *Journal of statistical physics*, 66(1-2):283–314, 1992.

D. Knight, G. Zhou, N. Okongo, and V. Shukla. Compressible large eddy simulation using unstructured grids. *AIAA Paper*, 535, 1998.

R.W. MacCormack and G.V. Candler. The solution of the navier-stokes equations using gauss-seidel line relaxation. *Computers & fluids*, 17(1):135–150, 1989.

M.P. Martin, U. Piomelli, and G.V. Candler. Subgrid-scale models for compressible large-eddy simulations. *Theoretical and Computational Fluid Dynamics*, 35:361–376, 2000.

D.J. Mavriplis. Revisiting the least-squares procedure for gradient reconstruction on unstructured meshes. *AIAA paper*, 3986, 2003.

D.W. Meyer and P. Jenny. Micromixing models for turbulent flows. *Journal of Computational Physics*, 228(4):1275–1293, 2009.

M.G. Mungal and P.E. Dimotakis. Mixing and combustion with low heat release in a turbulent shear layer. *J. Fluid Mech*, 148:349–382, 1984.

M.G. Mungal and C.E. Frieler. The effects of damköhler number in a turbulent shear layer. *Combustion and flame*, 71(1):23–34, 1988.

I. Nompelis. *Computational study of hypersonic double-cone experiments for code validation.* PhD thesis, University of Minnesota, 2004.

I. Nompelis and T. Schwartzentruber. A parallel implementation strategy for multi-level cartesian grid based dsmc codes. *AIAA Paper*, 1204, 2013.

I. Nompelis, T.W. Drayna, and G.V. Candler. Development of a hybrid unstructured implicit solver for the simulation of reacting flows over complex geometries. *AIAA Paper*, 2227, 2004.

I. Nompelis, T.W. Drayna, and G.V. Candler. A parallel unstructured implicit solver for hypersonic reacting flow simulation. *AIAA paper*, 4867, 2005.

T. Poinsot and D. Veynante. *Theoretical and numerical combustion.* RT Edwards Incorporated, 2005.

T.J. &amp Poinsot and S.K. Lele. Boundary conditions for direct simulations of compressible viscous flows. *Journal of computational physics*, 101(1):104–129, 1992.

S.B. Pope. Transport equation for the joint probability density function of velocity and scalars in turbulent flow. *Physics of Fluids*, 24:588–596, 1981.

S.B. Pope. Pdf methods for turbulent reactive flows. *Progress in Energy and Combustion Science*, 11(2):119–192, 1985.

S.B. Pope. Computations of turbulent combustion: progress and challenges. In *Symposium (International) on Combustion*, volume 23, pages 591–612. Elsevier, 1991.

S.B. Pope. *Turbulent flows.* Cambridge university press, 2000.

S.B. Pope. Small scales, many species and the manifold challenges of turbulent combustion. *Proceedings of the Combustion Institute*, 2012.

H. Risken. *The Fokker-Planck Equation*. Springer, 1989.

D.H. Rudy and J.C. Strikwerda. Boundary conditions for subsonic compressible navier-stokes calculations. *Computers & Fluids*, 9(3):327–338, 1981.

M.R.H. Sheikhi, P. Givi, and S.B. Pope. Velocity-scalar filtered mass density function for large eddy simulation of turbulent reacting flows. *Physics of fluids*, 19:095106, 2007.

M.R.H. Sheikhi, P. Givi, and S.B. Pope. Frequency-velocity-scalar filtered mass density function for large eddy simulation of turbulent flows. *Physics of Fluids*, 21:075102, 2009.

C. Shu and S. Osher. Efficient implementation of essentially non-oscillatory shock-capturing schemes. *Journal of Computational Physics*, 77(2):439–471, 1988.

B. Sjögreen and H.C. Yee. Multiresolution wavelet based adaptive numerical dissipation control for high order methods. *Journal of Scientific Computing*, 20(2):211–255, 2004.

M.D. Slessor, C.L. Bond, and P.E. Dimotakis. Turbulent shear-layer mixing at high reynolds numbers: effects of inflow conditions. *Journal of Fluid Mechanics*, 376: 115–138, 1998.

P. Spalart, W. Jou, M. Strelets, and S. Allmaras. Comments of feasibility of les for wings, and on a hybrid RANS/LES approach. *Advances in DNS/LES, 1st AFOSR International Conference on DNS/LES*, 1997.

P.R. Spalart and S.R. Allmaras. A one equation turbulence model for aerodinamic flows. *AIAA journal*, 94, 1992.

P.K. Subbareddy and G.V. Candler. A fully discrete, kinetic energy consistent finite-volume scheme for compressible flows. *Journal of Computational Physics*, 228(5): 1347–1364, 2009.

S. Subramaniam and D.C. Haworth. A probability density function method for turbulent mixing and combustion on three-dimensional unstructured deforming meshes. *International Journal of Engine Research*, 1(2):171–190, 2000.

B. Vreman. *Direct and Large-Eddy Simulation of the Compressible Turbulent Mixing Layer*. PhD thesis, University of Twente, 1995.

B. Vreman, B. Geurts, and H. Kuerten. Realizability conditions for the turbulent stress tensor in large-eddy simulation. *Journal of Fluid Mechanics*, 278(1):351, 1994.

B. Vreman, B. Geurts, and H. Kuerten. Subgrid-modelling in les of compressible flow. *Applied scientific research*, 54(3):191–203, 1995.

H.C. Yee. A class of high-resolution explicit and implicit shock-capturing methods. *NASA TM-101088*, 1989.

H.C. Yee, M. Vinokur, and M.J. Djomehri. Entropy splitting and numerical dissipation. *Journal of Computational Physics*, 162(1):33–81, 2000.

S.L. Yilmaz. *RANS/PDF and LES/FDF for Prediction of Turbulent Premixed Flames*. PhD thesis, University of Pittsburgh, 2009.